SIXTH FRAMEWORK PROGRAMME

Project no. 018412

IRASMOS

Integral Risk Management of Extremely Rapid Mass Movements

Specific Targeted Research Project

Priority VI: Sustainable Development, Global Change and Ecosystems

D1.2 – Report on the use of causes and triggers for up-/downscaling and interregional comparison

Due date of deliverable: 31/05/2008

Actual submission date: 15/07/2008

Start date of project: 01/09/2005 Duration: 33 months

WSL Swiss Federal Institute for Snow and Avalanche Research

Revision [2]

Project co-funded by the European Commission within the Sixth Framework Programme (2002-2006)		
Dissemination Level		
PU	Public	
PP	Restricted to other programme participants (including the Commission Services)	
RE	Restricted to a group specified by the consortium (including the Commission Services)	
CO	Confidential, only for members of the consortium (including the Commission Services)	

SIXTH FRAMEWORK PROGRAMME
PRIORITY VI
Sustainable Development, Global Change and Ecosystems

SPECIFIC TARGETED RESEARCH PROJECT

INTEGRAL RISK MANAGEMENT OF EXTREMELY RAPID MASS MOVEMENTS

WORK PACKAGE 1:
FROM CAUSES TO FORECASTING

DELIVERABLE D1.2

State-of-the-art models: their transferability and model application

Edited by:
RICCARDO RIGON (CUDAM, WP1 LEADER)

Contributions by:

CUDAM
POLIMI
CEMAGREF
OLIVER KORUP - WSL

DATE: AUGUST 23, 2007 – **1.3-VERSION**

TABLE OF CONTENTS

	scale mass movements (such as large landslides for instance), which are absent from the Manival ***catchment.***
Figure 24	(from Veyrat-Charvillon, 2005): Relation between variations in sediment accumulation for the 9 homogeneous zones defined in the Manival channel (in m3/year: histogram) and annual precipitations recorded in the nearby station of St-Pierre de Chartreuse. The dotted line represents the annual cumulated precipitations, and the full line represents the averages over the periods for which sediment data are available.
Figure 13	Variation of the failure probability with volumetric soil moisture evolution. Grey areas are rocky outcrop characterised by a very steep topography where the slope angle is larger than the internal friction angle and areas with scarce sediment availability.
Figure 14	Sauris geologic map.
Figure 15	Sediment analysis according to the photo-geology interpretation.
Figure 16	Variation of stable and unstable areas with depth. Soil depth is represented through 5 layers of 0.1 m, 0.30 m, 0.5 m, 0.6, m and 1 m respectively.
Figure 17	Variation of the stable areas with respect to time and depth. Stable areas refer to a triggering probability ranging from 0 to 20%. t1 refers to a day within the interstorm period and t2 refers to a day after the precipitation peak
Figure 18	Variation of the areas, whose failure probability ranges from 40 to 60 %, with respect to time and depth. t1 refers to a day within the interstorm period and t2 refers to a day after the precipitation peak.
Figure 19	Variation of the areas, whose failure probability ranges from 60 to 80 %, with respect to time and depth. t1 refers to a day within the interstorm period and t2 refers to a day after the precipitation peak
Figure 25	Example of the results obtained on four aspect of the Mont-Blanc massif on 17th September 2001 at 12 UTC in analysis mode. The surface humidity is drawn on the left as the yellow line (top left scale in %), with the arrows indicating the wind speed (bottom left scale in m/s). In the center the temperature is in full blue line (bottom scale in °C) and cloudiness in dotted line (top scale in [0,1]). The precipitation is to the right of the central axis (top right scale, grey squares means rain). All the radiation values are plotted on the right (direct="✧ "sun; scattered=mixed "✸" dotted/black sun; atmospheric=mixed "○" dotted/white circle) with their scales on top and bottom of this side in W/m2)
Figure 26	Example of the 1 day range operational forecast mode of SAFRAN concerning the 24hr precipitation at 1800m a.s.l over 24 alpine massif on flat aspect for the 11th January 1999. The left picture shows the verification analysis (performed in real time), the middle picture exhibits the final operational 24hr precipitation forecast (issued the 10th January) as seen by the forecaster. This forecast is based on the result of the meteorological model ARPEGE (right side top) and a nearest neighbours research (here the 14th March 1996, right side bottom).
Figure 27	Comparisons between observed and numerically simulated snowpack structures during the 1996-97 winter at the ski resort of "La Plagne" (Vanoise massif) on the snow pit location of "Montchavin" (2100m, NE). The different panels illustrate the weekly observed snow pits and the corresponding computed profile. The vertical axis (in cm) represents the snow depth and the blue and green curves respectively temperature and density profiles (with two different scales on the horizontal axis in °C and %V). On the right side of each profile , the stratigraphic profile is illustrated by the color code

	presented in next figure while vertical hachures show crusts.
Figure 28	Color code used for the snow crystals representation. This figure shows the connection with the international classification (Colbeck et al., 1990). Briefly, the fresh snow is represented by green colors, faceted crystals by a blue coloration and rounded crystals by red. As explained in Brun et al. (1992), fresh snow is described in terms of dendricity and sphericity and the more transformed crystals are defined by their size and sphericity.
Figure 29	Observed snowpack profile during the avalanche case of "Roc du Fer" on February 16th, 1996 showing the profiles of temperature (°C) and ram hardness (kgf) at different depths "H". According to Colbeck et al. (1990) the columns F1 and F2 indicate the two main grain shapes. The density "Dens" of each layer is in kg/m3, and the grain size is described by its diameter "Diam" in tenth of mm. The column "Wet" at 1 indicates a dry profile whereas the different manual hardness "Hard" is expressed on a 5 level scale. A manual estimation of the shear strength (in kg/dm2) is given in the column "Shear".
Figure 30	Simulated SCM snowpack profile at a computing location corresponding to the site of the avalanche case of "Roc du Fer" on February 16th, 1996 (Vanoise massif, East, 2100m, 40 deg. Slope) and showing the same two profiles as in the previous figure. Nevertheless the two main grain shapes are presented in a column named "grain", the diameter of the grain size (column "diam") is in mm and the density "dens" in 103 kg/m3. The "S" stability index is printed in the last column.
Figure 31	Symbolic representation (elevation and aspects) of MEPRA natural avalanche risks and types on the "Gdes-Rousses" massif for one slope (40 deg) in a typical winter situation (1995/01/23 at 12 UTC) as seen on the user screen.
Figure 32	Symbolic representation (elevation and aspects) of MEPRA natural avalanche risks and types on the "Belledonne" massif for one slope (40 deg) in a typical spring situation (1994/03/09 at 12 UTC) as seen on the user screen.
Figure 33	Time evolution (over winter 98-99 on x axis) of the snow stratigraphical profile in a reference station with total sow depth on y axis. Grain types area referenced with the left-hand colour code.
Figure 34	Time evolution of SNOWPACK snow drift index.
Figure 35	Representation of the nearest neighbors in NXD2000. On the left part the ten nearest neighbors with some of their previous days are shown, on the right top their variables and on the right bottom the aspect altitude diagram of the observed avalanches
Figure 36	Result of NXD-REG for 19 February 2000
Figure 37	Graphical presentation of the nearest neighbour method
Figure 38	Map showing the location of nearest neighbour application sites
Figure 39	Screen shot from the software implementing the nearest neighbour method
Figure 40	Evolution of the variance in ASTRAL with the number of available
Figure 41	Astral results screen in Geliniv environment.
Figure 42	ASTRAL Raw variables for analysis day and the first analogous day
Figure 43	Avalanche hazard according to wind and three days precipitation
Figure 44	Cumulative probability distribution of three day precipitation at Raffelsteinfonn causing avalanche occurrence
Figure 45	Distribution of curves for five avalanche paths
Figure 46	Terrain profiles for the five investigated avalanche paths in Grasdalen, Stryn

Figure 47	Weather observations from Grasdalen, Strynefjell 1. and 2. of March 1997

Chapter 1

MODELLING OF DEBRIS FLOW AND SHALLOW LANDSLIDES

1.1 Review on current approaches to triggering

Introduction

Shallow landslides are important mass-movement processes that may transform into **debris flows**. Hence, a detailed treatise on modeling the occurrence and dynamics of debris flows requires a focus on shallow landslide occurrence in the first place. Triggering of shallow landslides phenomena depend in a complex manner upon initial and boundary conditions and are affected by the heterogeneity of the hydraulic and geotechnical properties of the soil, topography, geological properties, soil moisture, and surface-subsurface interactions. Until now, landslide forecasting has been tackled according to three main approaches: (1) geomorphologic, (2) hydrological, and (3) geotechnical (see Casadei [2003] and references therein).

The geomorphologic analysis emphasizes spatial correlations between the location of landslides and topography, geology, soil properties and land use characteristics. This analysis is largely inferential and statistical. Applications for landslide hazard assessment typically consist of empirical correlations between landslide occurrence and rainfall that define a threshold condition above which shallow landslides can be expected. In order to identify triggering conditions within a storm or within a storm season, two thresholds are typically defined [e.g. Godt et al., 2005]: (1) an antecedent rainfall threshold, requiring an accumulation of a certain amount of rainfall during the season, and (2) a storm intensity-duration threshold, requiring a critical combination of rainfall intensity and duration be exceeded during the course of the storm.

For a long time hydrological modelling has dealt with the identification of triggering conditions related to intensity-duration thresholds within a storm or a storm season [Caine 1980, Campbell 1975, Wieczorek 1987, Larsen 1993]. This procedure relies on plotting storm intensity versus cumulative rainfall for observed events. A simple, regional-specific curve identifying precipitation intensities which cause debris flow initiation is then constructed.

The geotechnical approach views landslide phenomena as dependent on space, time and stresses within the soil. Their analysis can be conducted at varying levels of detail. Physically-based models that analyse the *spatial* pattern of regional landslide susceptibility such as SHALlow STABility analysis (SHALSTAB) [Montgomery & Dietrich 1994], and Stability INdex MAPping (SINMAP) [Pack et al., 1998] couple a simple steady-state hydrology with an infinite-slope analysis for the computation of the safety factor or stability index, defined as the ratio of the stabilizing to the destabilizing forces. Neither approach is appropriate to assess the time-dependent nature of landslide occurrence. Understanding of this time dependence is critical for assessing the likelihood of slope failure in response to actual rainfall conditions and is required for meaningful prediction or forecasting.

Mass wasting is the major landform shaping process in mountainous and steep terrain. Many landslides result from infrequent meteorological or seismic events that induce unstable conditions on otherwise stable slopes or accelerate movements on unstable slopes. Thus, the delicate equilibrium between the resistance of the soil to failure and the gravitational forces tending to move the soil downslope can be easily upset by external factors, such as rainstorms, snowmelt, and vegetation management. The major triggering mechanism for slope failures is the build-up of soil pore water pressure. This can occur at the contact between the soil mantle and the bedrock [Pierson, 1977; Sidle and Swanston, 1982; Megahan, 1983] or at the discontinuity surface determined by the wetting front during heavy rainfall events. The control factors of landslide susceptibility in a given area may be subdivided into two categories: quasi-static and dynamic. The quasi-static variables deal with geology, geotechnical properties, slope gradient, aspect and long term drainage patterns. The dynamic variables deal with hydrological processes and human activities, which trigger mass movement in an area of given susceptibility.

Landslides hazard assessment is based on a variety of approaches and models. Most rely on either multivariate correlation between mapped (or observed) landslides and landscape attributes [e.g., Carrara et al., 1991, 1995; Carrara, 1983; Chung et al., 1995], or general associations of landslides hazard from rankings based on slope lithology, land form or geological structure [e.g. Campbell, 1975; Hollingsworth and Kovacs, 1981; Lanyon and Hall, 1983; De Graff and Canuti, 1988; Seely and West, 1990; Montgomery et al., 1991; Neiman and Howes, 1991; Derbishire et al., 1995]. Antecedent precipitation amounts [e.g. Campbell, 1975; Wieczoreck, 1987; Canuti et al., 1985] and daily rainfall rate [e.g. Crozier, 1999; Glade et al., 2000] were further introduced as triggering factors of shallow landsliding. The statistical approach can provide an insight of multi-faceted processes involved in shallow landsliding

	occurrence, and useful assessments of susceptibility to shallow landslide hazard in large areas. But the results are very sensitive to the dataset used in the analysis, and it is not straightforward to derive the hazard (i.e. probability of occurrence) from susceptibility. Other studies [e.g. Caine, 1980; Cancelli and Nova, 1985; Cannon and Ellen, 1985; Keefer et al., 1987; Wieczoreck, 1987; Wieczoreck et al., 2000] analysed the intensity and duration of rainfalls triggering landslides. They built the critical rainfall threshold curves, defined as envelope curves of all rainfall triggering landslides events for a certain geographic area.
Physical modelling	Due to the lack of a process-based analysis, this method is unable to assess the stability of a particular slope with respect to certain storm characteristics and it does not predict the return period of the landslide-triggering precipitation [D'Odorico et al., 2005]. Hence, another approach deals with spatially distributed and physically based models coupling slope stability equation with a hillslope hydrological model. This can provide an insight of triggering processes of shallow landslides at the basin scale, also accounting for the spatial variability of the involved parameters. Some of these models consider the build-up of soil pore water pressure deriving uniquely from the increase of a saturated layer above a predefined critical slip surface approaching subsurface flow in different way, i.e. steady state or dynamic [e.g. Okimura and Ichikawa, 1985; Montgomery and Dietrich, 1994; Dietrich et al., 1995; Pack et al., 1998, Wu and Sidle, 1995; Casadei et al.; 2003, Iida 2004]. Montgomery and Dietrich, [1994]; Dietrich et al., [1992,1993,1995,2001]; Pack et al., [1998] treat the subsurface flow as steady state analyzing the topographic control on the pore pressure. Using the pore pressure in the slope stability equation permits to estimate slope stability and produce maps of relative potential of shallow landslides [Montgomery et al., 2000; Dietrich et al., 2001]. Montgomery and Dietrich [1994] developed a simple model for the topographic influence on shallow landslides initiation by coupling digital terrain data with near-surface through flow and slope stability models. The hydrological model is based on the flow tube approach [see e.g. O'Loughlin, 1986; Dawes and Short, 1994; Moore, 1988; Moore and Grayson, 1991]. It predicts the degree of soil saturation in response to steady state rainfall for topographic elements defined by the intersection of contours and flow boundaries. The slope stability component uses this relative soil saturation to analyse the stability of each topographic element for the case of cohesionless soils and of spatially constant thickness and saturated conductivity. Further developments of this model include SHALSTAB, a freeware software application to evaluate slope instability associated with the potential occurrence of shallow landsliding [Dietrich and Montgomery, 1998]. Several applications show this approach to be capable of capturing the spatial variability of shallow landslides hazard, because of the essential role of topographic control in shallow landsliding. This approach permits uncalibrated predictions and has proven reasonably successful, though there is a tendency for over prediction to occur, depending on the quality of topographic data [Dietrich et al., 2001]. The approach by Montgomery and Dietrich [1994] does not account for transient movement of soil water. It only accounts for density and friction angle of the soil in

	analysing slope stability, neglecting other soil characteristics and the moisture content in the soil layer above the groundwater table. This simplification can affect model capability of predicting shallow landslide potential because the steady-flow condition can be unrealistic in the course of rainstorm.
	The Rosso et al. [2006] approach starts from Montgomery and Dietrich [1994] indicating that simple models coupling soil mechanics with hydrology can provide an insight of shallow landslide initiation useful for mapping the potential hazard of landslide occurrence. Accordingly, the topographic description of hillslope elements is based on the flow tube approach. The hillslope stability model accounts for the key characteristics of the soil mantle, i.e. angle of shearing resistance, void ratio and specific gravity of solids. Hillslope hydrology is modelled by coupling the conservation of mass of soil water with the Darcy's law used to describe seepage flow . This yields a simple model capable of accounting for the combined effect of storm duration and intensity in the triggering mechanism of shallow landslides. Finally, coupling of the model for the hydrologic control on shallow landsliding with the simple scaling model for the frequency of storm precipitation [Burlando and Rosso, 1996] can help understanding the climate control on landscape evolution associated with the occurrence of shallow landslides.
Unsteady physical models	Unsteady flow was approached by Okimura and Ichikawa [1985] modelling shallow subsurface flow with finite difference model, Wu and Sidle [1995] introducing a contour based distributed physically based model that couples the infinite slope approach to slope stability with a groundwater kinematic wave model, also accounting for changing vegetation root strength in time. Casadei et al. [2003] linked a dynamic spatially distributed shallow subsurface runoff model accounting for evapotranspiration and unsaturated zone storage to an infinite slope model. Iida [2004] presented a hydro-geomorphological model considering both the stochastic character of rainfall intensity and duration and the deterministic aspects controlling slope stability. The unsteady subsurface flow producing saturated soil depth was investigated using a simplified conceptual model. These models provide an insight of the triggering mechanisms of shallow landslides, but they include a complex parameterization of hillslope properties and drainage patterns, so requiring detailed field data analysis.
	The build-up of pore water pressure as generated by the advance of the wetting front was investigated by Pradel and Raad [1993] using the Green–Ampt infiltration model to analyse the critical wetting front position triggering failure. Rulli et al. [1999] developed a distributed model coupling the Green and Ampt infiltration model, kinematic subsurface flow and infinite slope stability model in order to investigate shallow landslides in areas where Hortonian runoff generation is predominant. Iverson [2000] provided an insight of physical mechanism underlying landslide triggering by rain infiltration by solving the Richard's equation. The model links slope failure and landslide movement to groundwater pressure heads that change in response to rainfall. These models provide an insight of the triggering mechanisms of shallow landslides, but they do not emphasize the link between rainfall duration and intensity and shallow landslide triggering.

	Reid [1994] considered both rainfall intensity and rainfall duration in the stability analysis. D'Odorico et al. [2005] enhanced the Reid's approach by coupling the short term infiltration model by Iverson [2000] and the long term steady state topography driven subsurface flow [Montgomery and Dietrich, 1994] and analysed the return period of landslide triggering precipitation using hyetograph at different shapes. They assumed that the pore pressure transient observable in the course of a rainfall is due to the unsteady vertical flow through the soil profile, while slope-parallel subsurface flow is assumed to at a longer time scale and to determine the pre storm wetness conditions.
Surface runoff modelling	The main limit of these models is that they have been primarily developed for floods prediction and so in any case they were not automatically tuned for landslide triggering. The primary problem to be solved in fact is the determination of the spatial distribution of runoff. In order to find the net precipitation effects, there are commonly two main approaches: Horton type [1945] based on the infiltration excess, Dunne type [1978] based on the saturation excess. Hypothetically we can assume that a slope, during an intense rainfall event, is subject to both the types of runoff, yet it can be noticed that, being the hydraulic conductivity much higher then rainfall intensity, the runoff is practically always of the Dunne type. Given these assumptions, the use of a GIUH method presents obvious advantages, like the possibility to determine, for every point in the basin, the peak of the discharge and its time of occurrence, together with the duration and return period of the precipitation involved [Rigon et al, 2004]. Therefore, it is possible to determine the critical conditions and times of the triggering [Rigon et al, 2004]. This is not a distributed approach in the usual meaning of the word, as the R-R model is always bound to the prediction of the discharge in a point. Yet, its semi-analytical formulation of the discharge enables a quick application of the model on all the points of the basin, and thus their relative stability assessment. The uncertainty about the location of the rills in the unchanneled slopes and the insufficient characterization of the friction (and consequently of the velocity), is partially overcome by the observation that landslides on average occur on the concave parts of the basins, where we have the natural convergence of the flows. For this reason it is necessary that the curvatures of the topography be accurately described, though the current resolution of DEM (digital elevation model) does not seem to be sufficient.
TOPMODEL	TOPMODEL [Beven and Kirkby, 1979; Beven et al., 1995] has been developed with the aim of providing a simple but physically reasonable, distributed description of the processes involved in rainfall-runoff production requiring a minimum of parameters. The main features of TOPMODEL are the integration of Richards equation on a finite portion of the slope, and the modelling of the hydraulic conductivity as a decreasing function of soil depth. It considers a steady condition, i.e. calculates in every element the balance between the sub-superficial flow in input and the output, without any water storage. According to this scheme, the formation of the superficial water table occurs through the combining effects of the lateral flow from upstream and infiltration. These simple assumptions allow to calculate the different saturation degree of each area, on the basis of the topographic characteristics: the steepest area tend to drain more rapidly,

	according to the piezometric gradient, whereas the most convergent area tend to accumulate water in excess, determining the rising of the water table as a function of the corresponding drainage area. These effect are combined in a single parameter called topographic (wetness) index, defined as $\ln\frac{a}{tg\beta}$, where, a is the upslope draining area per unit contour length, and $\tan\beta$ is the slope gradient. Regions of the landscape that drain large upstream areas or that are very flat give rise to high values of the index; thus areas with the highest values are most likely to become saturated during a rain or snowmelt event and thus are most likely to be areas that contribute surface runoff to the stream. The approach used in TOPMODEL, assuming a steady hydrology, is targeted at representing the runoff under humid conditions and slow/constant precipitations and thus is not really capable at representing rapid and intense events.
IUH - GIUH models	The unit hydrograph of the basin is the surface runoff hydrograph caused by a unit excess rainfall distributed uniformly over the area. It represents also the distribution of the residence times of the water volumes inside the basin [Gupta and Waymire, 1980], [Rodriguez-Iturbe and Valdes, 1979]. This latter interpretation has permitted the construction of the IUH on the basis of the morphology/topology of the basins and of the hydrograph networks [Rodriguez-Iturbe, 1996], [Rodriguez-Iturbe and Rinaldo, 1997], [D'Odorico and Rigon, 2003], giving origin to the geomorphologic instantaneous unit hydrograph (GIUH).
	1.2 Methods of analysis
	According to Sidle and Ochiai [2006], methods of assessing landslide hazards can be roughly divided into four categories: 1. Terrain stability mapping [e.g. Ives and Messerli 1981, Kienholz et al 1984, Howes and Kenk 1988] 2. Simple rainfall-landslide relationship [e.g. Caine 1980, Keefer et al. 1987, Larsen and Simon 1993] 3. Multi factor, empirical landslide hazard assessments [e.g. Aniya 1985, Gupta and Joshi 1990, Pachauri and Pant 1992] 4. Distributed, physically based models [e.g. Montgomery and Dietrhich 1994, Miller 1995, Wu and Sidle 1995] Some of these methods are more amenable to assessing relative landslide hazard at regional scales, others can be used as predictive tools for more specific sites, and yet others can be used to develop real-time warning system. With each increment of specificity, the intensity of required data increases.
Terrain hazard mapping	Terrain hazard mapping represents a somewhat general and qualitative level of landslide hazard assessment; topographic, geomorphic and geologic information are used, as well as data on pre-existing landslide to generate maps with broad categories of landslide hazards [e.g. Dobrovolny 1971, Kienholz et al 1984, Howes and Kenk 1988, van Den Eeckhaut et al. 2005]. Typically, such hazard mapping is developed or at least implemented by management agencies or regional governing bodies to evaluate

	the effect of various land uses on the occurrence of landslides. Thus, the main focus may be not be to predict landslide occurrence, but rather to reduce the risk of landslide hazard related to a particular land use. If the assessment includes quantitative factors related to vulnerability of the element at risk, then it can be considered a landslide risk assessment [e.g Alexander 1992, Fell 1994, Parise 2001]. Other types of hazard maps may identify specific landscape or geologic features (e.g. geomorphic hollows, areas of wind throw, sensitive clays, and vulnerable bedrock sequences) that are susceptible to slope failure. For some regional examples of this method (Western Oregon, British Columbia, Raukumara Peninsula) of terrain stability mapping see Sidle and Hirotaka [2006]. Recent advances in remote sensing techniques (see paragraph 1.6) and the development and application of contour based digital elevation models (DEMs) can improve terrain hazard mapping, especially when processed within geographic information system (GIS) [Sakellariou and Ferentinou 2001, Lee et al. 2002, Dhakal et al. 2002, Mizukoshi and Aniya 2002]. In particular, satellite imagery and light detection and ranging are useful for assessing landslide locations as well as developing detailed DEMs and hillshade [e.g. Lee et al. 2002, Wills and McCrink 2002, van Den Eeckhaut et al. 2005]. High resolution DEMs produced from airborne laser altimetry can be used to assess surface characteristics of active and dormant landslides as well as delineating detailed topographic information useful in predicting areas of future landslides [Dietrich et al. 2001, Haugerund et al. 2003, McKean and Roering 2004] However, identification of landslide locations is subject to interpretation, and considerable differences are apparent when comparing results from hillshade map interpretation with those based on field surveys [Wills and McCrink 2002, van Den Eeckhaut et al. 2005].
Simple rainfall-landslide relationship	Landslide hazard assessment based on simple relationship with rainfall characteristics has been applied at both the global [Caine 1980] and regional [Cannon and Ellen 1985, Canuti et al. 1985, Larsen and Simon 1993] scales. When coupled with real-time rainfall data, such analyses can provide the basis for early warning system for shallow landslide [Keefer et al 1987, Iiritano et al 1998].
Multi factor empirical landslide hazard assessment	In empirical landslide analysis, the factors contributing to landslide initiation are typically established based on characteristic of existing landslides. The end product is focused on producing maps, or at least useable decision tools. Most approaches assume that landslides are more likely to occur under conditions similar to those of previous failure [Brabb 1984, Varnes 1984]. Multi-factor methodologies typically estimate landslide hazard using the relationships between past landslide patterns with various site characteristics. In such cases, the weighting of site attributes affecting slope stability is important. Factors typically considered include topography, geology, vegetation cover or land use, hydrology and soil properties. Trigger mechanisms are usually not included because such hazard assessment focuses on condition predisposing hillslope to failure.

	Statistical approaches to landslide analysis involve developing relationships among factors affecting landslides based on a priori statistical analyses; these relationships are then applied to sites with similar characteristics [Soeters and van Westen 1996]. In bivariate statistical analysis, each factor is evaluated separately in conjunction with landslide density (or volume). This bivariate approach has been widely used to identify factors that are significantly related to landslide occurrence and, if significant, relative weightings are assigned [e.g. Gupta and Joshi 1990, Mehrotra et al. 1996, Ayalew and Yamagishi 2005]. Multivariate approaches to empirical landslide hazard analysis consider the interrelationship amongst factors in terms of selection and weighting. After sampling all relevant factors at appropriate scales, the presence or absence of landslides is determined. Multiple regression or discriminate analysis is then typically used to analyse the resulting matrix [Mulder and van Asch 1988, Carrara et al. 1988, Rollerson et al. 1997, Dhakal et al. 2000]. For some example applications of this method see Sidle and Hirotaka [2006]. To significantly improve multi-factor landslide hazard assessment, three major issues need to be overcome: 1. Methods that can be applied to broader geographical area or in areas that experience multiple failure types need to be developed 2. A clear focus needs to be placed on the underlying processes that relate to slope failure 3. Temporal as well as spatial attributes of landslide susceptibility need to be incorporated in the analysis.

Distributed physically based model	As a theoretical advance from empirical landslide models based solely on rainfall characteristic, numerous infiltration-based landslide models have been developed for individual sites in both two and three dimensions [e.g. Anderson et al. 1988, Sammori and Tsuboyama 1990, Haneberg 1991]. Such models offer the advantage of a physics-based approach to assessing the dynamic changes in positive and negative (suction) pressure heads in the soil mantle during the infiltration process and thus are valuable to predict the timing of slope failure relative to rainfall inputs at individual sites with simple slope configurations. However these models present many problems in application to real situation connected with complex topography of each site. Physically based landslide models [e.g. Skempton and Delory 1957, Okimura 1982, Sidle 1992] assess stability in terms of F_S (stability factor): for $F_S>>1$ the slope is stable. If single parameter input values are used to calculate FS, this method is most suitable for smaller areas because in larger areas the variations in terrain and soil parameters inherent in the analysis are typically too large [Lumb 1975, Burton et al. 1998, Haneberg 2004]. Distributed physically based landslide models hawe two uniquo requirements: 1. spatially and, in some cases, temporally distributing model parameters are necessary 2. the model output must be spatially and temporally explicit because of the need to know the locations and timing of landslides. For some examples of this type of model see, for instance, Sidle and Hirotaka [2006].
	1.3 Example of models
	There are many numerical models dealing with stability analysis and landslide triggering. Some of them are codes still oriented to research, others are already available on the commercial market. In this session we will review some of the current codes available.

SHALSTAB	SHALSTAB is a digital terrain model for mapping shallow landslide potential. It is based on a simplification of the infinite slope analysis coupled to the hydrologic model TOPMODEL. The model assumes that the resistance to movement along the sides and ends of the landslide is not significant and that the cohesion is zero. Furthermore, the model does not consider the effects of root strength on slope stability on the assumption that the model is capturing the condition of low root strength that would occur after cutting, disease, or a fire. To model the hydrologic controls, the steady state shallow subsurface flow is calculated based on the work of O'Loughlin [1986]. The coupled hydrologic-slope stability equation is solved by the program. The model has three topographic terms that are defined by the numerical surface used in the digital terrain model: drainage area, outflow boundary length and hillslope angle. There are potentially four parameters that need to be assigned to apply this model: the soil bulk density, the angle of internal friction, the soil transmissivity, and the effective precipitation. The proneness to instability is defined by the value assumed by the ratio q/T, being q the discharge in input to the water table and T the transmissivity. The critical q/T value is given by a regional back-analysis on the local long period landslide inventory. The program can be used as a parameter-free model, in which the only decision is how to rank the mapped pattern of relative stability into such categories as "high", "medium" and "low", for the practical purpose of prescribing some land management practice. This utility is accomplished by eliminating many processes or factors that do matter to slope instability but require too much local parameterization to be useful in a practical context for application over large areas [http://www.ggsd.com/ggsd/index.cfm].
SINMAP	SINMAP model is one of digital models that describe terrain stability implemented in a GIS environment. Its application is limited to shallow transitional debris slides. The theoretical basis of the model is the relation between infinite slope stability and a steady-state hydrological model, represented by a parameter of topographical moisture index. The model requires three groups of input data: 1. terrain topography in a DEM grid format; 2. soil mechanical and hydraulic properties in a grid or polygon vector format; 3. landslide source areas inventory in a point vector format. Topographic data in DEM format are pre-processed by a built-in pit-filling module. Then the required topographic parameters, such as slope and specific catchment area, are calculated. The model requires the following soil properties data: • range of cohesion values; • soil density value; • range of internal friction angle values; • range of R/T ratio. For calibration purposes the landslides inventory map is needed, obtained from aerial or satellite orthophoto. The modelling results are presented in a form of maps, where the stability probability is expressed as stability index (SI):

$SI = prob(SF > 1)$ where SF is the safety factor.

If $SF > 1$ then $SI = SF$.

The topographic wetness index is divided into five classes and the graph of landslide occurrence in fields of slope and specific catchment's area.

By adopting suitable ranges for variables it is possible to calibrate and group the majority of observed landslides into the smallest SI classes (***Table 1***).

Table 1. The definition of slope stability index SI classes.

SI value	**Predicted state**	**Possible influence of factors not included in the model**
SI>1.5	Stable slope zone	Significant destabilizing factors are required for instability
1.5>SI>1.25	Moderately stable zone	Moderate destabilizing factors are required for instability
1.25>SI>1.0	Quasi-stable slope zone	Minor destabilizing could lead to instability
1.0>SI>0.5	Lower threshold slope zone	Destabilizing factors are not required for instability
0.5>SI>0.0	Upper threshold slope zone	Stabilizing factors may be responsible for stability
0.0>SI	Defended slope zone	Stabilizing factors are required for stability

This model has some limitations:

1. The model is designed to simulate only shallow transitional landslides initiation zones controlled by shallow subsurface flow;
2. It is not applicable to deep-seated instability zones;
3. It simulates landslides potential initiation zones, not hazard areas;
4. Spatial accuracy is strongly dependent on DEM resolution.

[http://www.ejpau.media.pl/volume6/issue1/environment/art-03.html]

dSLAM

The dSLAM model [Wu and Sidle, 1995] currently is not available for public use and, hence, could not be fully evaluated. It couples DEM data with a planar infinite-slope stability model, a hydrologic algorithm that simulates groundwater movement as cinematic waves through topographic elements similar to those constructed in the SHALSTAB model, and an algorithm that explicitly characterizes root strength. Whereas contributing rainfall is treated as steady-state in the SHALSTAB model, this model can accommodate spatially constant but temporally varying rainfall input (i.e., single or multiple storm events). Hence, the model must calculate a factor of safety in time steps to simulate the measured rainfall patterns. The model requires as input site-specific data on soil properties, vegetation type and age, and individual storm hyetographs (e.g., actual or simulated). Consequently, this model is computationally more complex and labour-intensive than the SHALSTAB model. Outputs of this model are shown as landslide and debris-flow path location maps, factor-of-safety distributions, and distributions of failure (i.e., hazard) potential. Management criteria (i.e., low, moderate, high "hazard") must be assigned by the user based on local knowledge. The dSLAM model has been evaluated by the authors on its ability to

	reproduce physical characteristics of measured landslides in a small, tributary drainage in the Oregon Coast Range. [http://www.krisweb.com/biblio/gen_tfw_shawetal_1999_pr1099001.pdf]
	1.4 Slope stability analysis (contribution of POLIMI)
	The present model improves the pioneering approach by Montgomery and Dietrich [1994] indicating that simple models coupling soil mechanics with hydrology can provide an insight of shallow landslide initiation useful for mapping the potential hazard of landslide occurrence. The topographic description of hillslope elements is based on the flow tube approach. The hillslope stability model accounts for the key characteristics of the soil mantle, i.e. angle of shearing resistance, void ratio and specific gravity of solids. Hillslope hydrology is modelled by coupling the conservation of mass of soil water with the Darcy's law used to describe seepage flow. This yields a simple model capable of accounting for the combined effect of storm duration and intensity in the triggering mechanism of shallow landslides. Finally, coupling of the model for the hydrologic control on shallow landsliding with the simple scaling model for the frequency of storm precipitation [Burlando and Rosso, 1996] can help understanding the climate control on landscape evolution associated with the occurrence of shallow landslides.
Slope stability analysis	In mountainous and hilly areas, the surface of the slope is quite often underlain by a plane of weakness lying parallel to it. This potential failure surface generally lies at a depth z below the surface, and this depth is small if compared with the length of the slope. Because the thickness of the soil mantle is much smaller then the length of the slope, one can generally assume that edging effects are negligible, so one can determine the safety factor of the slope against slip, *FS*, from the analysis of a wedge or slice of material of unit width and unit thickness [*Skempton and De Lory*, 1957]. Let θ denote the slope angle to the horizontal, and z the depth of the potential failure plane (***Figure 1***). The water table is taken to be parallel to the slope at a height $h = \omega z$ above the failure plane, with $0 \leq \omega \leq 1$. Steady seepage is assumed to occur in the direction parallel to the slope. The side forces for any vertical slice are equal and opposite, and the stress conditions are the same at any point on the failure surface. One also assumes that the rigid perfectly plastic rheologic model holds for the soil, that is, there is null strain until failure and shear strength is constant after the failure independently on strain.

Figure 1: One dimensional sketch for slope equilibrium.

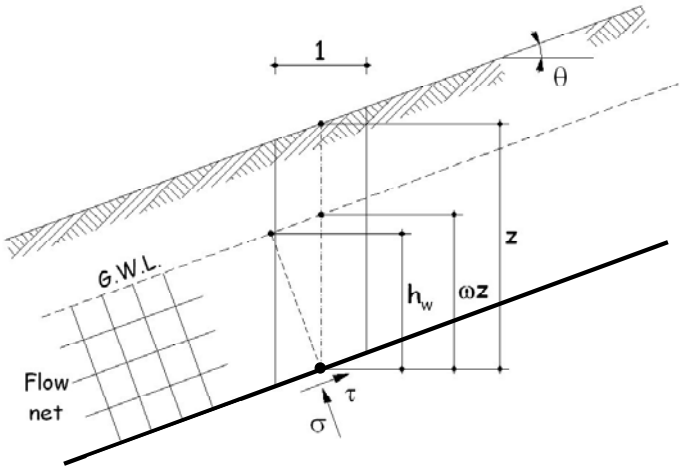

The shear strength of the soil along the potential failure plane is

$$\tau_f = c' + (\sigma - u)\cdot \tan\phi' \qquad (1)$$

with c' denoting soil cohesion, σ the normal total stress, u the pore water pressure, and ϕ' the angle of shearing resistance of the soil mantle. If τ_f is the shear stress, the safety factor is

$$FS = \frac{\tau_f}{\tau} \,. \qquad (2)$$

If one denotes with γ the average bulk unit weight of soil above the ground water level, and with γ_{sat} the saturated unit weight of soil under the ground water level, the expressions for σ, τ and u are

$$\sigma = \left[(1-\omega)\cdot\gamma + \omega\cdot\gamma_{sat}\right]\cdot z\cdot\cos^2\theta \,, \qquad (3a)$$

$$\tau = \left[(1-\omega)\cdot\gamma + \omega\cdot\gamma_{sat}\right]\cdot z\cdot\sin\theta\cdot\cos\theta \,, \qquad (3b)$$

$$u = \omega\cdot z\cdot\gamma_w\cdot\cos^2\theta \qquad (3c)$$

Substituting Eqs. (3) for σ, τ and u in Eqs. (1) and (2) yields the general expression for the safety factor in the form

$$FS = \frac{c' + \left[(1-\omega)\cdot\gamma + \omega\cdot\gamma'\right]\cdot z\cdot\cos^2\theta\cdot\tan\phi'}{\left[(1-\omega)\cdot\gamma + \omega\cdot\gamma_{sat}\right]\cdot z\cdot\sin\theta\cdot\cos\vartheta} \,. \qquad (4)$$

where $\gamma' = \gamma_{sat} - \gamma_w$ is the submerged unit weight of soil.

For cohesionless soils and normally consolidated clays cohesion is negligible, so that one can use $c' = 0$ in practice. If $c' = 0$ in Eq. (4) the safety factor is independent of thickness of soil mantle z, that is

$$FS = \frac{\left[(1-\omega)\cdot\gamma + \omega\cdot\gamma'\right]}{\left[(1-\omega)\cdot\gamma + \omega\cdot\gamma_{sat}\right]}\cdot\frac{\tan\phi'}{\tan\theta} \quad . \quad (5)$$

Let denote with $G_s = \gamma_s / \gamma_w$ the specific gravity of solids, $S_r = V_w / V_v$ the average degree of saturation and $e = V_v / V_s$ the average void ratio above the ground water table (being V_v, V_s, and V_w the volume of voids, that of solids and that of water in the control volume, respectively). Thus,

$$\frac{\gamma}{\gamma_w} = \frac{G_s + e\cdot S_r}{1+e} \quad , \quad (6a)$$

$$\frac{\gamma_{sat}}{\gamma_w} = \frac{G_s + e}{1+e} \quad , \quad (6b)$$

$$\frac{\gamma'}{\gamma_w} = \frac{G_s - 1}{1+e} \quad . \quad (6c)$$

These are substituted for γ, γ_{sat} and γ' in Eq. (5) to obtain

$$FS = \frac{\left[G_s + e\cdot S_r - \omega\cdot\left(1 + e\cdot S_r\right)\right]}{\left[G_s + e\cdot S_r + \omega\cdot e\cdot\left(1 - S_r\right)\right]}\cdot\frac{\tan\phi'}{\tan\theta} \quad (7)$$

The following special cases are of interest. If $\omega = 0$, i.e. the groundwater level lies at the potential failure surface,

$$FS = \frac{\tan\phi'}{\tan\theta} \quad . \quad (8)$$

If $\omega = 1$, i.e. the water table lies at the surface of the slope,

$$FS = \frac{\left(G_s - 1\right)}{\left(G_s + e\right)}\cdot\frac{\tan\phi'}{\tan\theta} = \frac{\gamma'}{\gamma_{sat}}\cdot\frac{\tan\phi'}{\tan\theta} \quad .(9)$$

One notes that the value of FS descending from Eq. (9) is about one half of that computed from Eq. (8) because $\gamma' \cong \gamma_{sat}/2$ in practice. If $0 \le \omega \le 1$, i.e. the water table lies between the potential failure surface and the slope surface, the limit equilibrium condition ($FS = 1$) occurs when the groundwater level index ω assumes a critical value, say, ω_{CR}. This means that the slope is stable for ω not exceeding ω_{CR}. This is given by

$$\omega_{CR} = \frac{\left(G_s + e \cdot S_r\right) \cdot \left(1 - \frac{\tan\theta}{\tan\phi'}\right)}{1 + e - e \cdot \left(1 - S_r\right) \cdot \left(1 - \frac{\tan\theta}{\tan\phi'}\right)} \quad (10)$$

For given G_s and e, Eqs. (8), (9) and (10) yield four states depending on actual slope and groundwater level index.

i) If $\frac{\tan\theta}{\tan\phi'} \le \frac{\left(G_s - 1\right)}{\left(G_s + e\right)}$, the slope is unconditionally stable.

ii) If $\frac{\tan\theta}{\tan\phi'} \ge 1$ the slope is unconditionally unstable.

iii) If $\frac{\left(G_s - 1\right)}{\left(G_s + e\right)} < \frac{\tan\theta}{\tan\phi'} < 1$ and $\omega < \omega_{cr}$, the slope is stable.

iv) If $\frac{\left(G_s - 1\right)}{\left(G_s + e\right)} < \frac{\tan\theta}{\tan\phi'} < 1$ and $\omega > \omega_{cr}$, the slope is unstable.

The present approach improves that introduced by Montgomery and Dietrich [1994] who neglected the effect of the void ratio and the degree of soil saturation above the groundwater table. ***Figure 2*** shows these four states for soils with specific gravity $G_s = 2.7$ and different values of average void ratio and average saturation degree of soil above the groundwater table. One notes that S_r has a negligible influence on slope stability. ***Figure 3*** shows model sensitivity to void ratio for different average saturation degree of soil above the groundwater table. One notes that S_r can be close to unity in practice, so the influence of void ratio can be moderate.

Figure 2: Soil mantle equilibrium for varying relative slope ratio, tanθ/tanϕ, vs relative groundwater depth, h/z, with specific gravity Gs = 2.7, and void index e of 0.5 (a), 1.0 (b), 1.5 (c), and 2.0 (d).

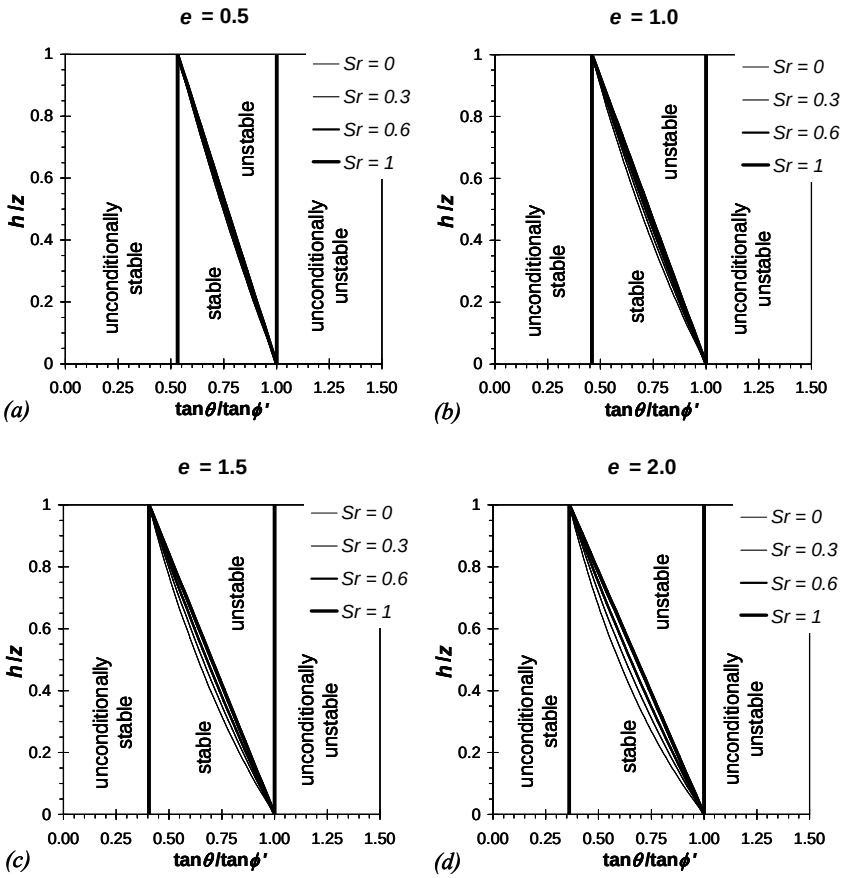

Figure 3. Model sensitivity to void ratio, e, for different degree of soil saturation above the groundwater table: dry (a), intermediate (b and c) and saturated (d).

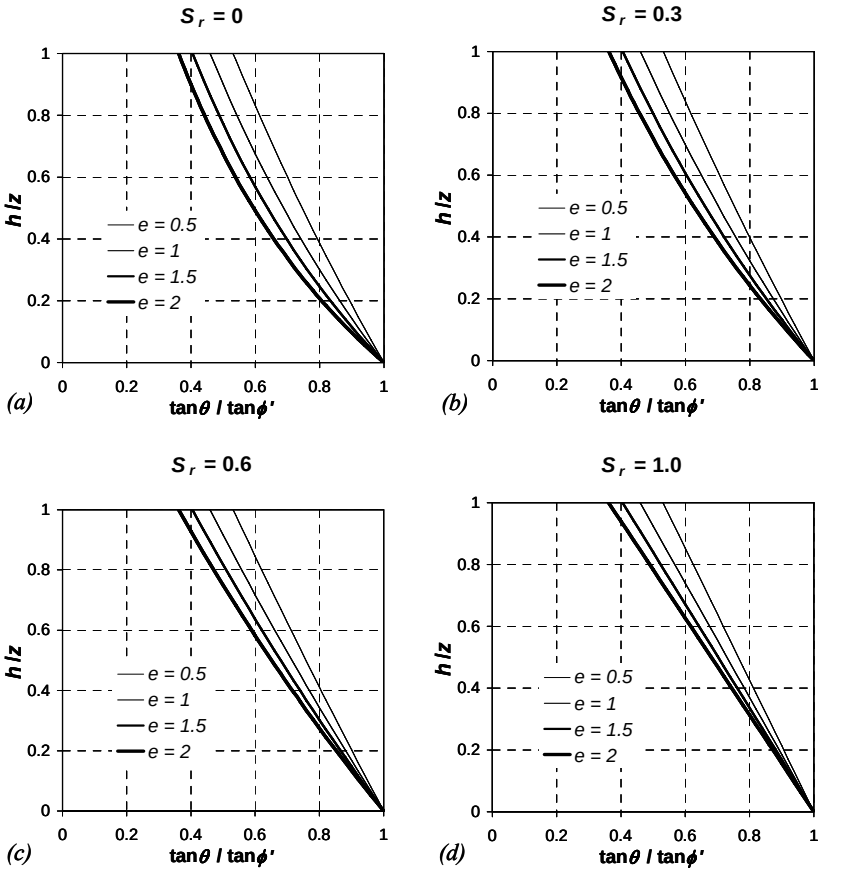

Hillslope hydrology modelling	The approach assumes that overland flow is generated by saturation excess. A hillslope is divided in topographic elements defined by intersection of contour and flow tube boundaries orthogonal to the contours (***Figure 4***).
Figure 4 Sketch of an elementary drainage area: planar view (a) and hydrological fluxes (b).	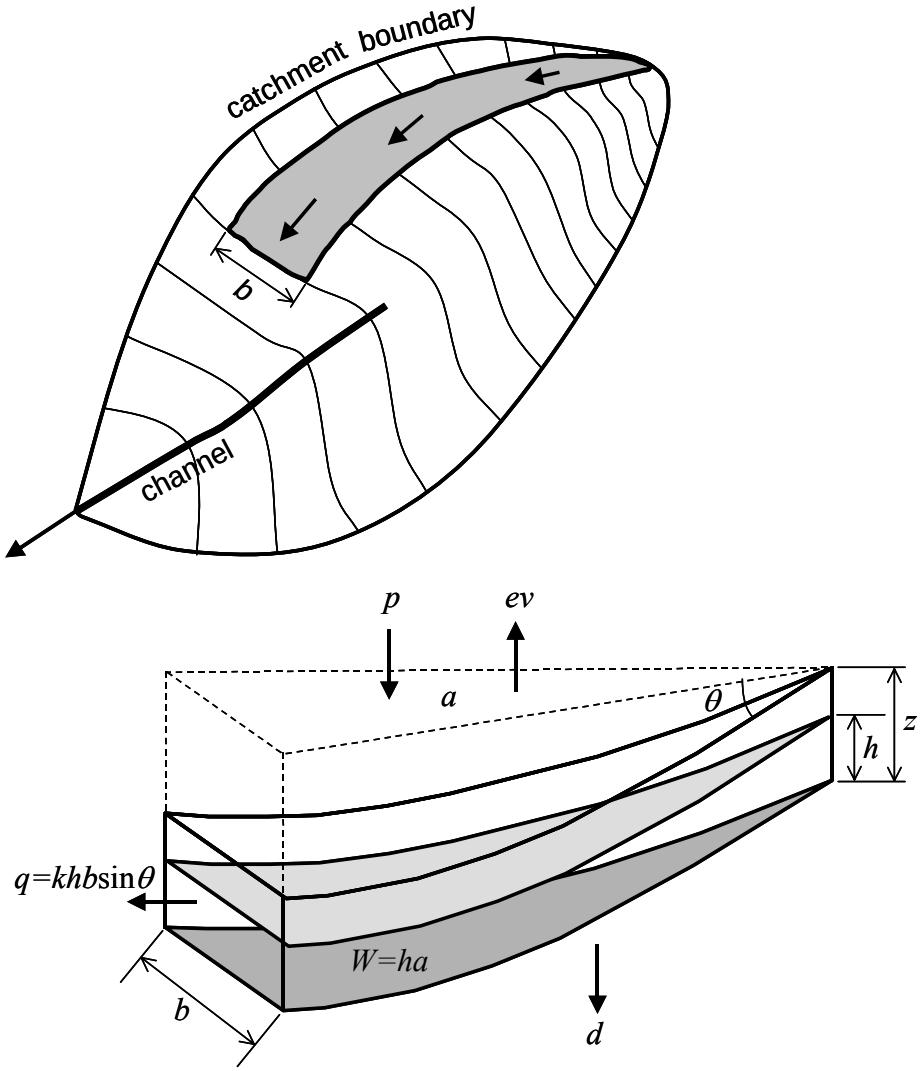
	Let consider a control volume defined as the sub-basin closed at one specific topographic element. It is assumed to occupy the entire flow domain by integrating out the spatial dependence of flux terms. Thus all flux terms are located on the boundaries of the flow domain and they can be grouped into bulk inflow rates and outflow rates. Let denote with p the net rainfall, i.e. precipitation less evapotranspiration and deep drainage into the bedrock, and a the upslope contributing area (i.e. the cumulative drainage area of all topographic elements draining into the examined element) draining across b, the contour length of the lower bound to each element. Under the assumptions of (*i*) zero soil volumetric strain (i.e., *average void ratio* is constant) and (*ii*) constant average soil saturation degree above the groundwater table (i.e., S_r is constant), conservation of mass yields $$ap - q = \frac{dS}{dt'} = a \cdot \frac{e}{1+e} \cdot (1 - S_r) \cdot \frac{dh}{dt'} \quad \text{, for } h \le z, \quad (11)$$

and

$$ap - q - r = 0 \text{, for } h > z, \quad (12)$$

with t' denoting time after the beginning of the storm, S the water storage in the element, and r the overland flow discharge occurring when soil is saturated (i.e. $S_r = 1$). The Darcy's law provides the seepage flow in the groundwater table. Thus,

$$q = (bh\cos\theta)K\tan\theta = bhK\sin\theta, \quad (13)$$

where K is the saturated conductivity of the soil, and $\tan\theta$ is the head gradient assumed to be parallel to the local ground slope.

Substituting Eq. (13) into (11) and integrating the differential equation for the initial condition of stable piezometric at the depth of $h_i(0) = h_i$, yields

$$h = \frac{apz}{Tb\sin\theta}\left[1 - \exp\left(-\frac{1+e}{e-eS_r}\frac{Tb\sin\theta}{az}t\right)\right] + h_i\exp\left(-\frac{1+e}{e-eS_r}\frac{Tb\sin\theta}{az}t\right)$$

$$\text{, for } \frac{ap}{Tb\sin\theta} > 1, \quad (14)$$

for a rainfall episode with duration t, with $T = Kz$ denoting the hydraulic transmissivity, i.e. the vertical integral along the soil depth of saturated conductivity of soil. By considering the simple case of the initial condition of stable piezometric at depth of $h(0) = 0$ and introducing the saturation precipitation rate, only depending on geometric and hydrologic properties of the hillslope and not from rainfall,

$$p^* = \frac{Tb\sin\theta}{a} \quad (15)$$

yields

$$h = \frac{p}{p^*}z\left[1 - \exp\left(-\frac{1}{A_1}\frac{p^*}{z}t\right)\right], \text{ for } p/p^* \le 1, \quad (16)$$

with

$$A_1 = \frac{e}{1+e}\cdot(1 - S_r) \quad (17)$$

denoting a dimensionless soil factor.

For $\frac{ap}{Tb\sin\theta} > 1$, i.e. $p/p^* > 1$, one obtains

$$h = \begin{cases} \frac{p}{p^*} z\left[1 - \exp\left(-\frac{1}{A_1}\frac{p^*}{z}t\right)\right] & , \text{if } t \le t^* \\ z & , \text{if } t > t^* \end{cases} \quad (18)$$

and

$$t^* = -A_1 \frac{z}{p^*} \cdot \ln\left(1 - \frac{p^*}{p}\right). \quad (19)$$

One notes that the characteristic time t^* depends on three factors, i.e. the dimensionless soil factor A_1 describing actual soil physics, z/p^* combining hillslope geomorphology with soil mantle characteristics, and p/p^*, that describes the relative precipitation rate to the critical value.

Figure 5 and ***Figure 6*** show the variability of h and $q+r$, respectively, with storm duration for different values of the topographic ratio a/b. For given slope, soil thickness, void ratio, degree of saturation of the soil above the groundwater table, soil transmissivity, drainage area and net rainfall rate, an increase of the topographic ratio a/b yields the steady state thickness of the groundwater table to increase. But the rate of increase of h in time is much higher for large a/b than that characterizing small values of a/b. Thus, large values of a/b yield runoff production to rapidly achieve steady state conditions, while much more time is needed for elementary areas with small values of a/b to achieve steady state runoff production.

Figure 5 Height of the groundwater table versus storm duration for different a/b under specified conditions.

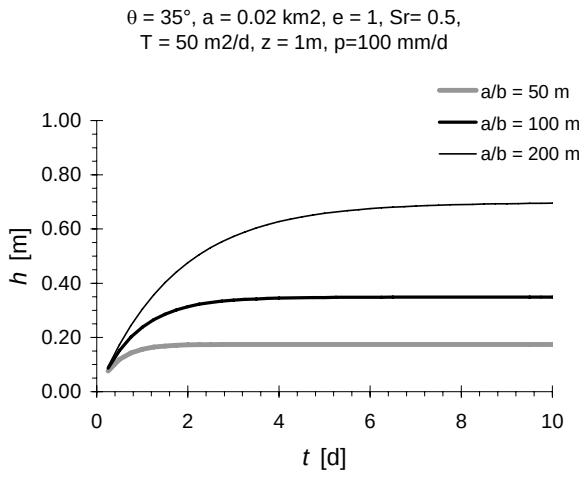

Figure 6 Runoff production versus storm duration for different a/b under specified conditions.

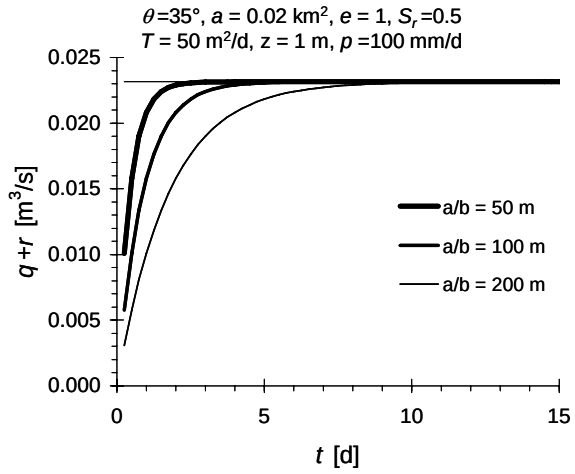

Introducing the groundwater level index, $\omega = h/z$, yields

$$\omega = \frac{p}{p^*}\left[1 - \exp\left(-\frac{1}{A_1}\xi\right)\right], \text{ for } p/p^* \le 1, \qquad (20)$$

and, for $p/p^* > 1$,

$$\omega = \begin{cases} \dfrac{p}{p^*}\left[1 - \exp\left(-\dfrac{1}{A_1}\xi\right)\right] & \text{, if } \xi \le -A_1 \ln\left(1 - \dfrac{p^*}{p}\right); \\ 1 & \text{, if } \xi > -A_1 \ln\left(1 - \dfrac{p^*}{p}\right); \end{cases} \qquad (21)$$

with $\xi = (p^*/z)t$ denoting a dimensionless time. ***Figure 7*** shows the variability of the groundwater level index ω with dimensionless time, ξ, for different values of dimensionless precipitation rate p/p^*.

Montgomery & Dietrich [1994] assumed that a steady state hydrologic model can mimic the effect of transient rainstorm with effective rainfall greater than a steady state

	value. Here one finds that the combined effect of rain rate and duration on hillslope stability can be significant. Also, the model is capable of describing the threshold effect occurring when full saturation occurs in the soil mantle, so triggering overland flow. This occurs, e.g., for p/p^* equal to 5 in ***Figure 7***.
Figure 7 Groundwater level index versus dimensionless time for different values of dimensionless precipitation rate, p/p, and soil dimensionless factor, A1.*	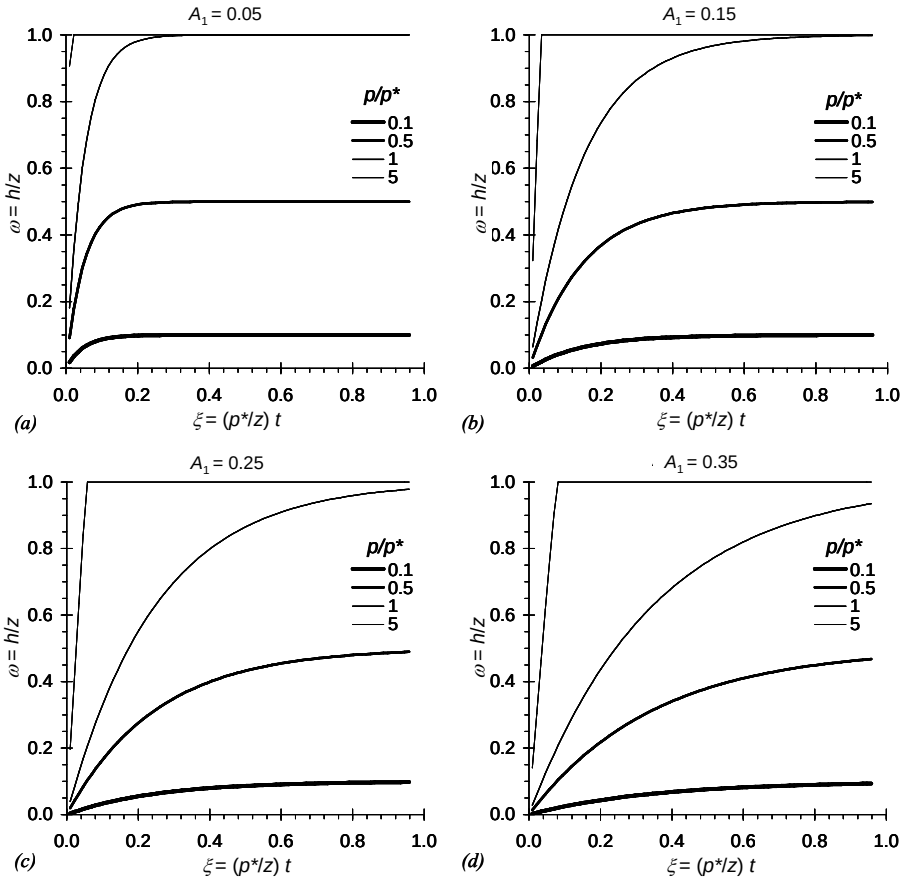
Precipitation threshold for slope instability	Coupling hillslope hydrology with geomechanics yields landslide triggering by precipitation. This is obtained by substituting the left-hand side of Eq. (10) with the right-hand side of Eq. (14) expressed in term of groundwater level index, ω. One obtains $$\frac{ap}{bT\sin\theta}\left[1-\exp\left(-\frac{1+e}{e-eS_r}\frac{bK\sin\theta}{a}t\right)\right]+\frac{h_i}{z}\exp\left(-\frac{1+e}{e-eS_r}\frac{Tb\sin\theta}{az}t\right)=$$ $$=\frac{(G_s+e\cdot S_r)\cdot\left(1-\frac{\tan\theta}{\tan\phi'}\right)}{1+e-e\cdot(1-S_r)\cdot\left(1-\frac{\tan\theta}{\tan\phi'}\right)} \quad , \qquad (22)$$ Solving Eq. (22) for p one obtains the rainfall rate threshold causing instability in the soil mantle under analysis, that is

$$p_{CR}(t)=\frac{T\frac{b}{a}\sin\theta\left[\frac{(G_s+e\cdot S_r)\cdot\left(1-\frac{\tan\theta}{\tan\phi'}\right)}{1+e-e\cdot(1-S_r)\cdot\left(1-\frac{\tan\theta}{\tan\phi'}\right)}-\frac{h_i}{z}\exp\left(-\frac{1+e}{e-eS_r}\frac{Tb\sin\theta}{az}t\right)\right]}{1-\exp\left(-\frac{1+e}{e-eS_r}\frac{Tb\sin\theta}{az}t\right)}, \quad (23)$$

with sub *CR* indicating the critical conditions for landslide initiation. Note that the precipitation threshold p_{CR} given by Eq. (23) is a function of measurable quantities describing the physical properties of the hillslope.

It is seen that the value taken by p_{CR} strongly depends on duration t of precipitation occurring at the constant rate p_{CR}, as displayed, e.g., in the examples shown in Figure 8 highlighting that the diffusive character of the equations smooth sudden peaks in rainfall intensity. Therefore, the steady state approach by *Montgomery and Dietrich* [1994] can overestimate landslide triggering conditions especially for storms with short duration, typically of less than one or two days. This also depends on initial moisture conditions, as one can see by comparing, e.g., the thresholds shown in Figure 8*d* ($S_r = 0.75$) with those shown in the other ones ($S_r = 0.5$). Finally, one can observe that the topographic index (a/b) still remains a fundamental factor in determining the rainfall threshold for shallow landslide initiation, as shown, e.g., in ***Figure 8***. The above approach for obtaining the rainfall rate threshold causing instability can be generalized to the case of non-constant hyetograph. The simple procedure considers the hyetograph subdivided in n time steps. For each time step the model computes the corresponding h considering as initial condition h_i the h calculated at the previous step. Finally P_{cr} will be obtained by substituting in Eq. (34) as h_i the h_{n-1}.

Eq. (34) can be written in dimensionless form as

$$\eta=\frac{p_{CR}}{p^*}=\frac{\frac{A_2\left(1-\frac{\tan\theta}{\tan\phi'}\right)}{A_3-A_4\left(1-\frac{\tan\theta}{\tan\phi'}\right)}-\frac{h_i}{z}\exp\left(-\frac{1}{A_1}\xi\right)}{1-\exp\left(-\frac{1}{A_1}\xi\right)}, \quad (24)$$

with

$A_2 = G_s + eS_r$, (25*a*)
$A_3 = 1 + e$, (25*b*)
$A_4 = e\,(1+ S_r)$, (25*c*)

	denoting dimensionless soil factors depending on specific gravity of soil particles, void ratio and saturation degree of soil above the groundwater table. The dimensionless critical precipitation rate $\eta = p_{CR}/p^*$ is plotted against dimensionless time $\xi = (p^*/z)t$ in ***Figure 9*** for different values of relative slope ratio ($\tan\theta/\tan\phi'$).

Figure 8 Relationship between critical rainfall rate and storm duration for different a/b under specified conditions (a = 0.02 km2, ϕ' = 42°, e = 1, Gs = 2.65, z = 1 m) and different combination of values taken by θ, Sr and T.

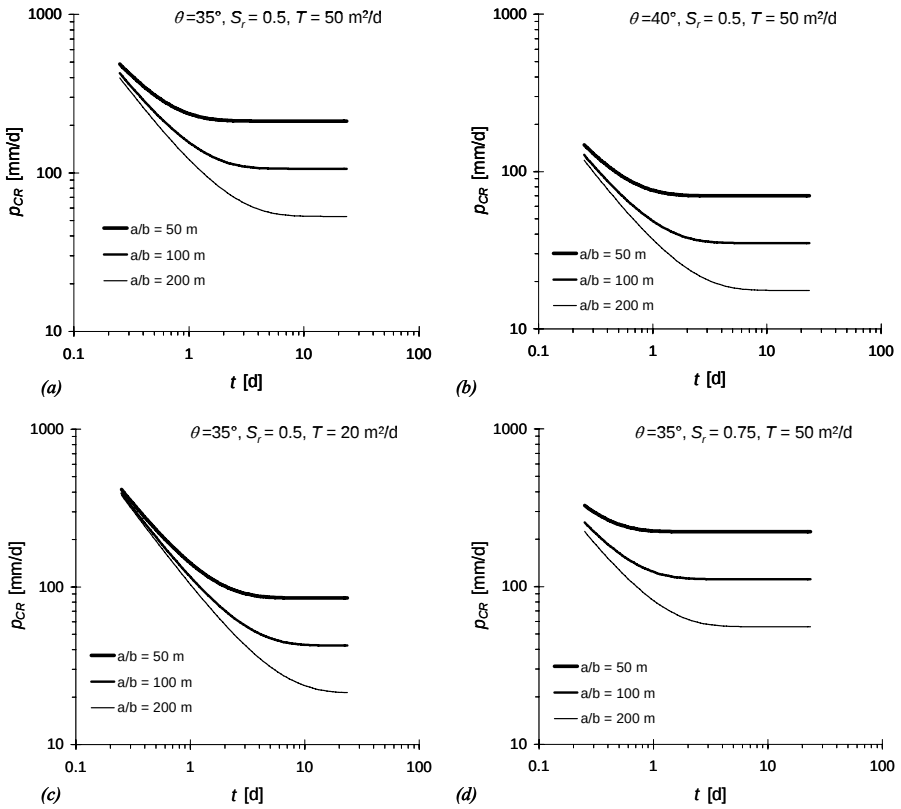

Figure 9 Dimensionless critical rainfall rate versus dimensionless time for different values of relative slope ratio and specified soil parameters e, Sr and Gs.

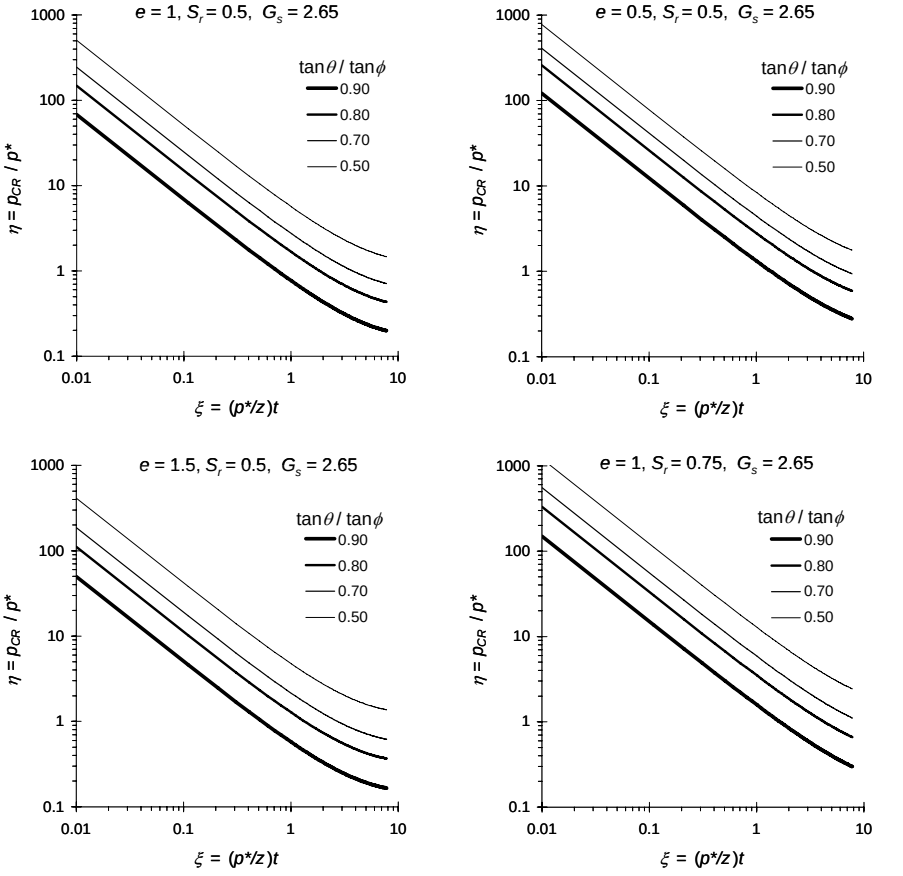

1.5 A probabilistic approach to slope stability analysis

GEOtop-SF computes the probability of shallow landslides being triggered under a given climatic and topographical frame. Taking as input the volumetric soil moisture content computed by the hydrological distributed model GEOtop [Bertoldi2005] and the geotechnical parameters characterizing the soil in the study area, SF maps the zones which are more prone to fail. Unlike groundwater-flow models used in SHALSTAB and dSLAM, which assume that water can flow only parallel to the slope and account for steady or quasi-steady pore pressure distributions only, GEOtop-SF also accounts for transient responses of pore pressure to rainfall infiltration. This reflects on a safety factor which varies with time according to the soil moisture conditions. SF has a 3D-layered structure that aims at reproducing the regional topography, the stratigraphy of the site and the vertical variability of soil properties. The thickness and the number of the layers are identified according to similar soil types and properties. Despite the fact that they match the horizontal layer sequence set in GEOtop, neither a preferential sliding direction nor a sliding thickness is a priori set in SF [***Figure 1***]. A superficial layer reproduces the root zone, allowing to account for the additional soil cohesion due to the bonding strength of roots in the soil. In addition, SF accommodates a horizontal variability of soil type, soil properties and vegetation cover. Maps of these parameters can then be input in the model. It is designed to tackle three main aspects:

- Dynamic 3D-hydrological processes;
- Hydrological and geotechnical soil characterization;
- Probabilistic and dynamic computation of the stability factor.

Hydrological processes are investigated by GEOtop which, in a distributed way, simulates the fluxes and budgets of energy and water on a landscape defined by three-dimensional grid boxes, whose surfaces is given by a DEM and whose lower boundaries are located at some specified spatially-varying depth. It also accounts for the presence of snow by adding a new layer on top of the DEM, as described in [Zanotti et al. 2004]. Surface boundary conditions are given by hydrometerological measurements (rainfall, temperature, wind velocity) regionalized, as described in [Bertoldi 2005].

On site geotechnical and geophysical campaigns provide useful information about substratum morphology, lithology and soil stratigraphy. In addition, geotechnical analyses performed on available soil samples, allow a more accurate soil characterization and therefore a more reliable simulation of soil behaviour. The model also accounts for the additional soil cohesion due to vegetation within the root zone. It accommodates distributed input but, in case this information is not available, lumped values can be assigned in the parameter file.

A probabilistic approach to the computation of the safety factor is motivated by a variety of uncertainties in the parameters having a leading role in landslide triggering. In fact, a deterministic approach based on a failure threshold would result scarcely reliable due to the fact that this threshold is determined assigning single values to parameters instead of distributions. Therefore each parameter is considered as a

	random variable associated with its variance whose values have to be estimated from data through statistics.
Figure 10 Scheme of GEOtop-SF. It presents a 3D-layered structure that can accommodate a simple geologic stratigraphy. Layers can be set (left) according to results from a drilling survey (right).	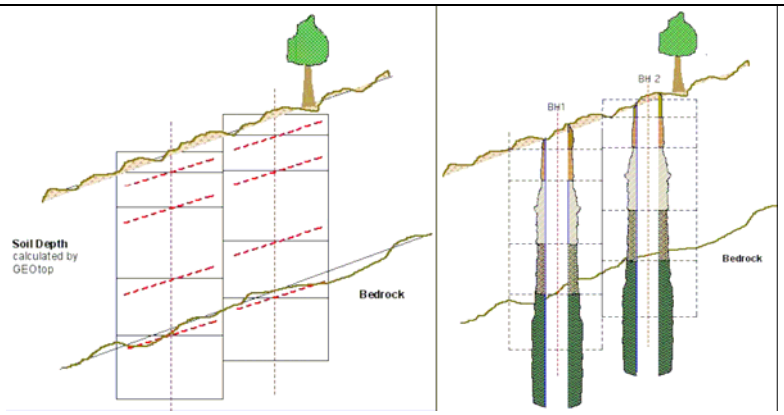
Hydrological Process	GEOtop, whose detailed description can be found in [Bertoldi 2005], models the following processes: (1) water and energy budget, (2) subsurface saturated and unsaturated flow, (3) surface runoff, (4) channel flow, (5) turbulent fluxes. Subsurface saturated-unsaturated flows strongly influence soil moisture, soil water potential (matric suction) and the water table position, which are elements relevant to landslide triggering. Soil moisture and matric suction within the soil layers are computed by integrating Richards' equation [Richards1931, Freeze1972], in a quasi-3D-scheme. This is done recursively, every time step, so that it is possible to follow the soil response to precipitation. The use of Richards' equation removes the need for the assumption of stationary conditions in subsurface flows and therefore it is possible to describe transient flows and infiltration. Richards' equation is here written according to [Paniconi & Putti 1994] as: $$\mathbf{q}_{\mathbf{sub}} = -K_s\, K_r(S_W)\nabla\,(\eta_z + \psi) \qquad (26)$$ $$\sigma(S_W)\frac{\partial \psi}{\partial t} = \nabla\cdot(K_s(T)\, K_r(S_W)\nabla\psi + \eta_z) - S, \qquad (27)$$ where the dependence from space and time of the variables has been dropped for notational simplicity, $\sigma(S_W) = S_W S_s + \phi\,\partial S_W/\partial\psi$ is the storage term [L^{-1}], $S_W(\psi) = \theta/\theta_s$ is the relative water saturation (the ratio between the volumetric soil moisture content θ_s), ϕ is the porosity [dimensionless], S_s is the aquifer specific storage coefficient [L^{-1}], ψ is the pressure hydraulic head [L], ∇ is the gradient operator, $K_s(T)$ is the saturated hydraulic conductivity, and T is the temperature [K]. $K_r(S_W) \equiv K(S_W)/K_S(T)$ is the relative hydraulic conductivity, $\eta_z = (0,0,1)^{\mathbf{T}}$, z is the vertical upward coordinate and S represents the modulus of the source or sink volumetric flow per unit volume. The saturated hydraulic conductivity $K_s(T)$ has in fact two components, the vertical, $K_{sv}(T)$, and the lateral $K_{sh}(T)$ grid-averaged values [Kumar2004b]. In the model they are considered

proportional according to an anisotropy ratio given by $\alpha_K = K_{sh}/K_{sv}$, which is used as a calibration parameter.

In GEOtop the relation between ψ and θ (equation 27) is given through the model,

$$\psi = \frac{1}{\alpha}\left(\left(\frac{\theta-\theta_r}{\theta_s-\theta_r}\right)^{-1/m} - 1\right)^{1/n}, \qquad (28)$$

where θ_r is the dimensionless residual water content, α [1/L], m and n are fitting parameters.

These parameters and the saturated hydraulic conductivity are 3D-fields in the model and many different strategies are possible for their assignment. In this work they have been derived from the sampled soil texture by means of the pedotransfer functions proposed by [Vereecken et al 1989] and [Leij et al 2004]. The relative hydraulic conductivity is expressed as a function of the water content as in [Mualem 1976]. The description of vertical infiltration in GEOtop takes into account the surface fraction actually covered in water, assuming the presence of micro-relief in the terrain, which is parameterized by a surface roughness parameter according to Smith 2002 as

$$\begin{aligned} &I = I_0 \quad if \quad d \geq h_0 \\ &I = I_0\, d/h_0 \quad if \quad d < h_0, \end{aligned} \qquad (29)$$

where I is the effective infiltration rate, I_0 is the infiltration rate with no micro-relief, d the surface water depth, and h_0 the micro-relief height. Runoff at the surface is generated because the precipitation intensity exceeds the soil surface infiltration capacity (infiltration excess runoff, [Horton 1993]) or the water table level rises above the soil surface (saturation excess runoff [Dunne1978}). Both of these possibilities are dealt with the Richards' equation solver and are implemented according to the comprehensive analysis of boundary conditions made by Paniconi1994. In addition, Richards' equation allows water to redistribute laterally and move uphill or exfiltrate according to local suction. GEOtop computes the hydraulic conductivity through Mualem1976 equation:

$$\begin{aligned} &K(\Theta) = K_s \Theta^v \left[1 - \left(1 - \Theta^{1/m}\right)^m\right]^2 \mathrm{mod}0.5cm \\ &where \\ &\mathrm{mod}0.5cm\Theta = \left(\frac{\theta-\theta_r}{\theta_s-\theta_r}\right) \end{aligned} \qquad (30)$$

where m has been set to 1 and v is usually set to 0.5.

Soil Characterization	Hydraulic and geotechnical soil properties strongly influence water flows and redistribution in porous media and determine the soil resistance to shear stress. Soil hydraulic conductivity, porosity, residual and saturated volumetric water content are parameters that control hydraulic mechanisms, whereas bulk density, lithology, stratigraphy, internal friction angle and soil cohesion, which includes cohesion due to cementation among soil particles, cohesion due to suction stress and cohesion due to vegetation, control the shear resistance, for a given moisture condition. These parameters assume distributed values and also vary with depth. The availability of data is therefore relevant to characterize the soil tendency to fail. The description of infiltration and redistribution processes requires the soil moisture retention curves (MRC), to be estimated. Since these are difficult to measure in the field, time consuming, costly and frequently impractical due to the high degree of spatial and temporal variability, methods able to relate easily measured soil physical properties to soil water characteristics are essential. Actually these relations are not unique and affected by a number of environmental and soil factors. Temperature, irregular pore geometry and discontinuities, variations in texture and mineralogy are the primary soil properties influencing soil water retention. Variability in these soil factors increases the uncertainty of predicting soil water retention values. As a consequence, methods for defining the soil hydraulic characteristic using mathematical models have been developed Vereecken1989 and Rawls1989. In this study the model proposed by Van Genuchten VanGenuchten1980 and modified by Vereecken setting the m-VanGenuchten parameter to 1, is used. The parameters defining the shape of the moisture retention curve implemented in GEOtop ($\theta_r, \theta_s, \alpha,$ n, equations 31-32-33-34) are evaluated according to [Vereecken et al. 1989]. $$\theta_r = 0.015 + 0.005 \cdot Cl + 0.0014 \cdot C \quad (31)$$ $$\theta_s = 0.81 - 0.283 \cdot \rho_b + 0.001 \cdot Cl \quad (32)$$ $$ln(\alpha) = -2.486 + 0.025 \cdot S - 0.351 \cdot C - 2.617 \cdot \rho_b - 0.023 \cdot Cl \quad (33)$$ $$ln(n) = 0.053 - 0.009 \cdot S - 0.013 \cdot Cl + 0.00015 \cdot (S)^2 \quad (34)$$ These relations have been empirically obtained through regression analyses on large soil database. They describe the dependence of the water content on soil texture in terms of sand, S, clay, Cl and carbon, C percentage and eventually on bulk density, ρ_b, and on pore size distribution. The soil texture, the parameters describing the shape of soil MRC, α and n, the saturated and unsaturated hydraulic conductivity k_s and $k(\theta)$, can be estimated at a reasonable level of accuracy from particle-size distribution analyses [Vereecken1989, Brooks1964]. Soil strength parameters, internal friction angle and cohesion at zero normal stress, are derived from drained shear tests.

	Values of additional soil cohesion due to vegetation root are assigned according to literature and to the vegetation type present on site. Lithology and stratigraphy can be investigated using seismic prospects and geological maps if available. The new coupled model GEOtop-SF is able to describe the soil behaviour under failure conditions if the input parameters are obtained from accurate soil analyses.
Dynamic Computation of the Safety Factor	The idea behind this coupled hydrological-geotechnical model is to describe in detail the interaction between 3D-hydrological fluxes and soil behavior in order to reproduce transient pattern of pore water pressures and understand their impact on slope stability. We believe that this constitutes a reliable framework for studying shallow soil slip. Soil failure mechanisms are described through an infinite-slope scheme (***Figure 11***) which takes into account the forces acting on a prismatic soil element with a unit plane area.
Figure 11 Infinite-slope model	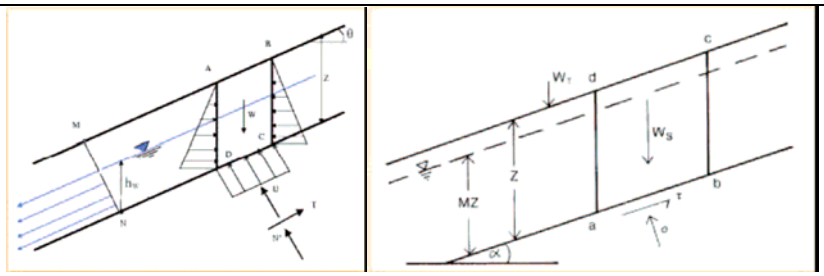
	The stability analysis of a natural slope can be tackled with respect to the long-term and to the short-term. The former is the case when the soil is drained and the excess of pore pressures have dissipated. In this case soil particles experience an effective stress due to actual loading conditions. The effective stress is the actual stress sustained by the soil skeleton [Terzaghi1943]. Failures can occur only as a consequence of an increment in loading conditions that exceed the soil shear strength. In this case flow mechanisms can be reasonably described by a steady or quasi-steady state. SF does not cope with this analysis. The latter is usually the case during and after rainfall when the soil gets wet and its volumetric water content increases. The generation of pore water pressures causes a reduction in soil effective strength [Terzaghi1943] and, as a consequence, the soil fails. Under saturation the soil effective stress σ' is given by the difference between the total stress σ and the pore water pressure u [Terzaghi1943], i.e. $\sigma' = \sigma - u$. Therefore the actual value considered for the computation of the safety factor is σ'. Despite the evidence that failures in natural slopes can occur also in unsaturated soil, where the pore water pressure is no longer a neutral stress [Lu2005], the version of SF here described only deals with saturated conditions. It computes the water table depth from the volumetric water content of each layer. This also allows perched water table to be considered. Unlike models which solve transient pore pressure redistributions through analytic solutions as function of time and depth [e.g. TRIGRS, Baum2002], GEOtop-SF solves the problem numerically. It simulates moisture content and the evolution of pore pressures, resulting from infiltration, solving water and energy budget equations for each pixel and for each time step. Therefore maps of volumetric soil water content,

	suction potential, water table depth and other hydrological parameters are available at a user-defined time. The module SF, assessing the stability of each pixel, runs at every time step with different soil moisture conditions. This provides a safety factor which varies in time and space. In addition, the calculation is iterated for each layer to investigate the stability at different depth. The layers are set in the GEOtop's parameter file imposed after having geotechnically characterized the soil. It is relevant to underline that these layers do not represent planes of imposed failure but only homogeneous soil horizons; in fact, the depth of a potential failure is allowed to vary from the surface to the bedrock. The computation of the active forces also considers the role of vegetation; in fact, according to Bischetti2004 the cohesion due to vegetation, depending on the type, on the rooted area (i.e. the ratio between the cross sectional soil area actually occupied by roots and the surface considered), on the root depth, on the root diameter and on the season, ranges from 20 to 50 kPa in the first 40 cm of the soil and from 5 to 20 kPa up to 1 m depth. The basic equation for the safety factor used in GEOtop-SF as starting point for the probabilistic approach is the following: $$sf(l,i,j) = \frac{F_{stabilizing}}{F_{destabilizing}}$$ $$sf(l,i,j) = \frac{2\left(c'(l,i,j)+\Delta_c(l,i,j)\right)}{\gamma_w L(l,i,j)\sin 2\alpha} + \frac{L(l,i,j)-\tan\phi(l,i,j)\cdot\sum_{k=1}^{l} d(k)\cdot\frac{\theta(k,i,j)}{\theta_s(k,i,j)}}{L(l,i,j)\cdot\tan\alpha(i,j)} \quad (35)$$ where $$L=\frac{W_T(i,j)+\sum_{k=1}^{l} d(k)\cdot\gamma(k,i,j)}{\gamma_w}, \quad (36)$$ c' is the effective cohesion due to soil particle cementation, Δ_c is the additional soil cohesion due to tree roots, ϕ is the internal friction angle, $d(k)$ is the thickness of layer k, θ is the volumetric water content, θ_s is the volumetric water content at saturation, α is the slope angle and $W_T(i,j)$ is the tree weight per unit area. (k,i,j) refers to the layer k in the column (i,j).
	1.6 Model application: CUDAM GEOtop model
GEOTOP model	Soil parameters uncertainty is incorporated considering the cohesion and the friction angle as random variables with a given distribution. As a first approximation soil parameter variability is assumed to be described by a Gaussian distribution, whose parameters, mean μ and variance σ^2, are taken from the analysis of the available geotechnical data.

$$\hat{f}_C = \frac{e^{-\frac{(c-\mu_c)^2}{2\cdot\sigma_c^2}}}{\sqrt{2\cdot\pi}\cdot\sigma_c};\quad \hat{f}_{\Delta_c} = \frac{e^{-\frac{(\Delta_c-\mu_{\Delta_c})^2}{2\cdot\sigma_{\Delta_c}^2}}}{\sqrt{2\cdot\pi}\cdot\sigma_{\Delta_c}};\quad \hat{f}_{tan\phi} = \frac{e^{-\frac{(tan\phi-\mu_{tan\phi})^2}{2\cdot\sigma_{tan\phi}^2}}}{\sqrt{2\cdot\pi}\cdot\sigma_{tan\phi}} \qquad (37)$$

Rewriting equation 2 in terms of random variables, C, Φ and Δ_C and highlighting the three terms constituting the safety factor, it is possible to associate a probability density function to the safety factor, which, in turns, becomes a random variable.

$$SF(l,i,j) = \frac{2C'(l,i,j)}{\gamma_w L(l,i,j)\sin 2\alpha} + \frac{2\Delta_C(l,i,j)}{\gamma_w L(l,i,j)\sin 2\alpha} + \frac{L(l,i,j) - \tan\Phi(l,i,j)\cdot\sum_{k=1}^{l} d(k)\cdot\frac{\theta(k,i,j)}{\theta_s(k,i,j)}}{L(l,i,j)\cdot\tan\alpha(i,j)} \qquad (38)$$

It is the sum of three independent random variables whose density probability can be calculated applying twice a convolution integral. In general, if Y is the sum of three random variables X_1, X_2 and X_3 and their pdf f_{X_1}, f_{X_2} and f_{X_3} are known, the pdf associated to Y is:

$$\hat{f}_Y(y) = \int_{-\infty}^{+\infty}\int_{-\infty}^{y-x_1} \hat{f}_{X_1X_2}(s,t)\cdot\hat{f}_{X_1X_2X_3}(y-s-t)dtds \qquad (39)$$

where $\hat{f}_{X_1X_2}$ and $\hat{f}_{X_1X_2X_3}$ are respectively the conditional probability of X_1 given X_2 and of X_1, X_2 given X_3. Applying this to the computation of the safety factor yields another Gaussian distribution.

$$\hat{f}_{SF(i,j)} = \frac{A\cdot D\cdot e^{-\frac{\left(A\cdot(D\cdot sf-\mu_b)-D\cdot(\mu_c+\mu_v)\right)^2}{2\cdot\left(A^2\cdot\sigma_b^2+D^2\cdot(\sigma_c^2+\sigma_v^2)\right)}}}{\sqrt{2\cdot\pi}\cdot\sqrt{\left(A^2\cdot\sigma_b^2+D^2\cdot(\sigma_c^2+\sigma_v^2)\right)}} \qquad (40)$$

$$SF = \frac{\mu_{\tan\Phi}}{D} + \frac{\mu c+\mu_{\Delta c}}{A} : \sigma_{SF}^2 = \frac{\sigma_{\tan\Phi}^2}{D^2} + \frac{\sigma_c^2+\sigma_{\Delta c}^2}{A^2} \qquad (41)$$

where

$$A = \frac{L(l,i,j)\gamma_w \sin 2\alpha(i,j)}{2};$$

$$D = \frac{L(l,i,j)\tan\alpha(i,j)}{L(l,i,j) - \sum_{k=1}^{l} d(k)\cdot(\theta(k,i,j) + 1 - \theta_s(k,i,j))} \quad (42)$$

The concept that a slope is unstable when the safety factor is less than 1 can be reinterpreted in probabilistic terms using the cumulated probability $F_{SF}(sf)$ which estimates the likelihood that the random variable SF takes a certain value sf. If this value is 1, the cumulated probability represents the probability that a failure occurs. ***Figure 12*** shows a plot of the cumulated probability, as a function of SF, obtained for three different values of the friction angle. It points out that the probability of failure is strictly related to soil properties. For a given slope and for a set of hydrologic parameters it decreases with the friction angle. In fact, the soil shear resistance is proportional to the tangent of the friction angle and therefore soils with larger friction angles exhibit a higher shear strength. GEOtop-SF computes the safety factor. This gives the mean value of the safety factor, also computed by GEOtop-SF, it provides a more reliable estimate of shallow landslide hazards.

$$F_{SF}(i,j) = P(SF \leq 1) = \int_{-\infty}^{1} \hat{f}_{SF(i,j)}\, dsf(i,j) \quad (43)$$

Figure 12 Cumulated probability of failure for three different values of the friction angle. The failure probability is strictly related to soil properties; for a given slope and for a set of hydrologic parameters it decreases with the friction angle.

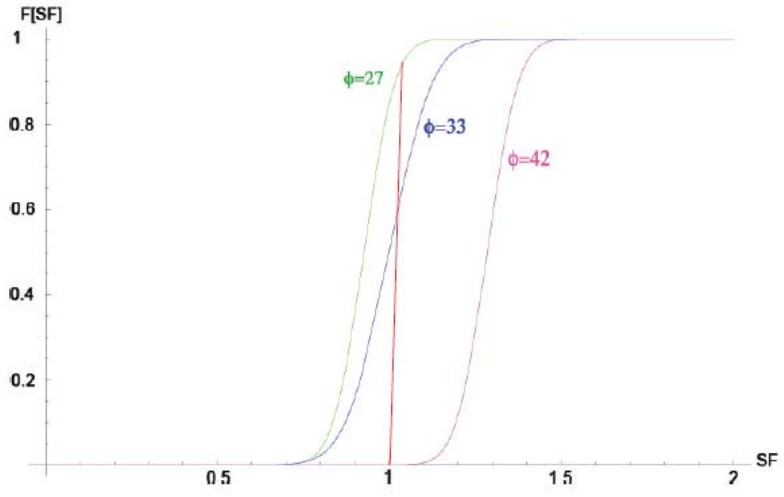

CUDAM Case study

The analysis presented has been carried out for an alpine watershed, located in the Friuli region, Italy, for which some geological and geotechnical data were available. In the past, this watershed experienced landslides and debris flows during intense storms following long and moderate intensity rainfall events. The distributed coupled GEOtop-SF model has been calibrated by reproducing some of these events and validated in order to map future failure probabilities.

	The data provided are: Volumetric soil moisture (computed by GEOtop); Geotechnical parameters characterizing the soil in the study area. In this section we present an application of the model whose target is testing its capability of simulating the large landslide occurred in 1817, using 250-year rainfall volume. The model was run for a year-time period so that the system has sufficient time to respond to the forcing and to reach a mean steady-state condition. The rational for that is that long-term average quantities are more representative of conditions at a particular catchment location if compared to short-term dynamical variations. We believe that this average steady-state conditions and dynamic equilibrium in surface and subsurface states prior to the analysis period. Boundary conditions have been set considering that we are interested in understanding and modelling shallow phenomena which occur in the first meters of soil, therefore taking into account the whole thickness of soil above the bedrock (up to 40 m) is not necessary. As a consequence, boundary conditions were set, according to the topography, at a variable depth of 3-4 m, in terms of gravity flux. This depth is divided into 5 layers of different thickness, 0.1, 0.3, 0.5, 0.6 and 1 m. The model was calibrated using the available meteorological data (years 2003-2004-2005), this provided initial conditions for the landslide event we wanted to simulate. Using a series of historic precipitation data, constituted by the maximum annual rainfall intensities for 1, 3, 6, 12, 24 hours, intensity-duration-frequency (IDF) curves were produced for several return periods. A return period of 250 years was assumed for the event of interest and the volume of water fell on the ground in a given period of time was computed using the corresponding IDF. At that stage, the pattern given by the available and more recent rainfall data (2003-2004-2005) was amplified for a 1-month-period, to obtain the same critical 250-year rainfall volume and with such a pattern GEOtop-SF was run to verify slope stability. GEOtop-SF run on Sauris catchment for 220 days; within this period, the rainfall pattern previously described presents its peak at 26 august 2004. Results were analyzed from two points of view. Firstly, a correspondence between soil moisture variation with time and probabilities of failure was sought to detect possible triggering conditions. Secondly the variation of unstable areas with depth was analysed to understand any possible trend

Figure 13: Variation of the failure probability with volumetric soil moisture evolution. Grey areas are rocky outcrop characterised by a very steep topography where the slope angle is larger than the internal friction angle and areas with scarce sediment availability.

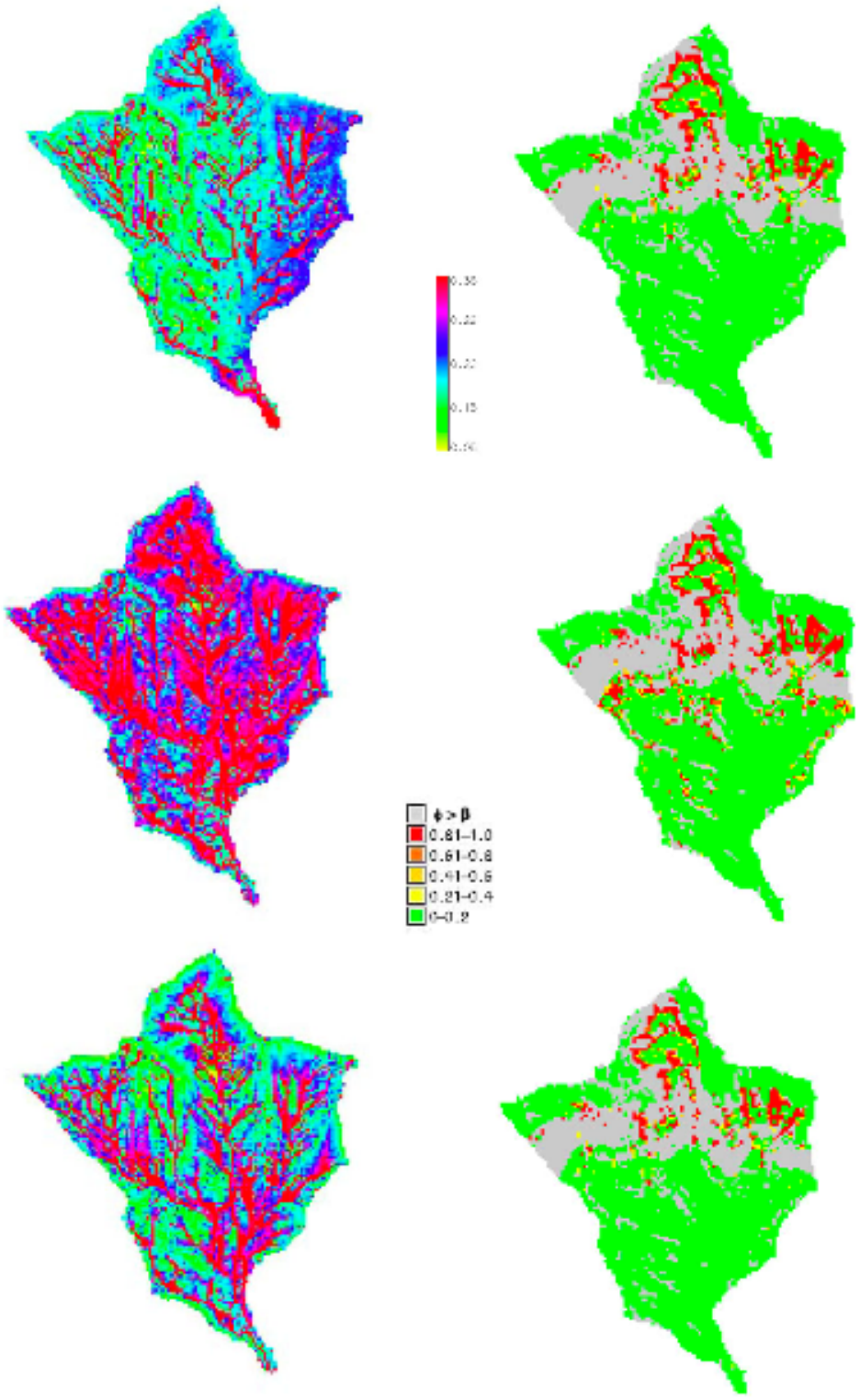

Figure 13 displays patterns of soil moisture and the relative probability of failure. The maps on the left hand-side show soil moisture evolution before and after the storm peak, the maps on the right hand-side show the probability of failure for each soil moisture condition. The first map, on the top left, refers to 10 days before the events, the middle map to maximum saturation day and the last, at the bottom left, to 10 days after the event. It is relevant to point out that the day of maximum saturation is shifted with respect to the peak of the storm. This delay, which is common in highly

	permeable soils where saturation occurs from below, is faithfully simulated by GEOtop. The effects of the increase in soil water content affect the probability of failure which assumes its maximum value in the same day. In fact, pore water pressure that develop in soil reduces its effective stress and, as a consequence, its shear strength. As soil begins to desaturate, pore water pressure decreases to pre-event conditions and consequently the probability of failure decreases. GEOtop-SF output shows that the Safety Factor is a time-dependent index which is strictly correlated to moisture conditions and therefore it has to be calculated at each time step to describe slope stability evolution during a storm. Grey areas have not been considered in the slope stability analysis since, from the geologic and the sediment maps (*Figure 14* and *Figure 15*), these areas are rocky outcrop characterized by a very steep topography where the slope angle is larger than the internal friction angle and areas with scarce sediment availability. As a consequence, the failure probability in such areas is, anyway, very low. The analysis of the variation of stable and unstable areas with depth is resumed in *Figure 16*, *Figure 17*, *Figure 18* and *Figure 19*. *Figure 16* suggests three main comments: 1. stable, green areas (whose probability of failure ranges from 0 to 20 %) decrease with depth; 2. unstable, orange and red areas (whose probability of failure ranges from 60 to 100 %) increase with depth; 3. the number of the areas characterized by mild instability (whose probability of failure ranges from 20 to 60 %, yellow and dark yellow areas) show a weak dependency on depth. Analyzing this issue in more details, two reasons may be found to explain such a behavior: the areas themselves do not change or, if a certain portion of areas, whose instability ranges from 0 to 20 %, increases such instability to 20-60 %, the same portion shifts its instability to 60-100 % range. In addition, *Figure 17* shows that the number of relatively stable areas (whose probability of failure ranges from 0 to 20 %), slightly changes in time, reflecting a weak dependency on soil moisture content. *Figure 18* and *Figure 19* highlight that: for a given range of failure probability (40-60% and 60-80% respectively), unstable areas increase toward the peak of the storm, t_2 (coarse dashed line), if compared to unstable areas in a interstorm period (fine dashed line). This reflects the trend of the soil moisture content and underlines physical connections between hydrological and geotechnical processes. Furthermore, the dependency between unstable areas and depth reflects a general trend toward an increase in unstable areas with depth; this increase is not linear, it is more emphasized within the first two layers than in the deeper ones.
Figure 14: Sauris geologic map.	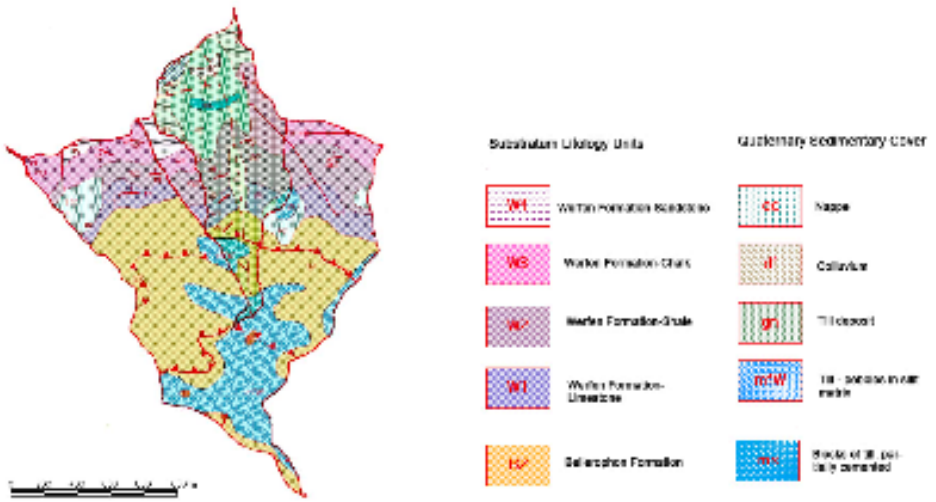

Figure 15: Sediment analysis according to the photo-geology interpretation.

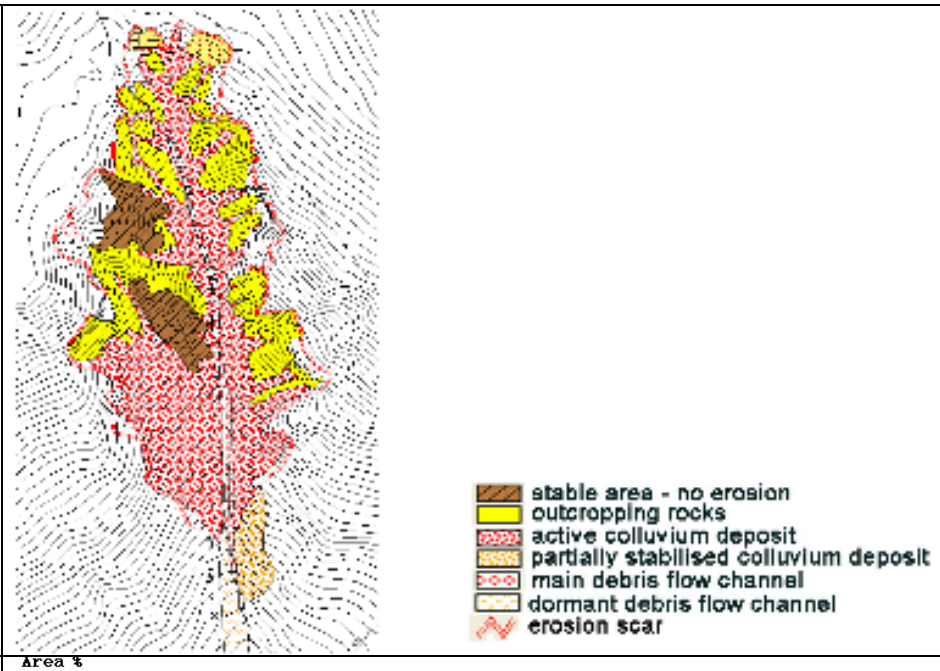

Figure 16: Variation of stable and unstable areas with depth. Soil depth is represented through 5 layers of 0.1 m, 0.30 m, 0.5 m, 0.6, m and 1 m respectively.

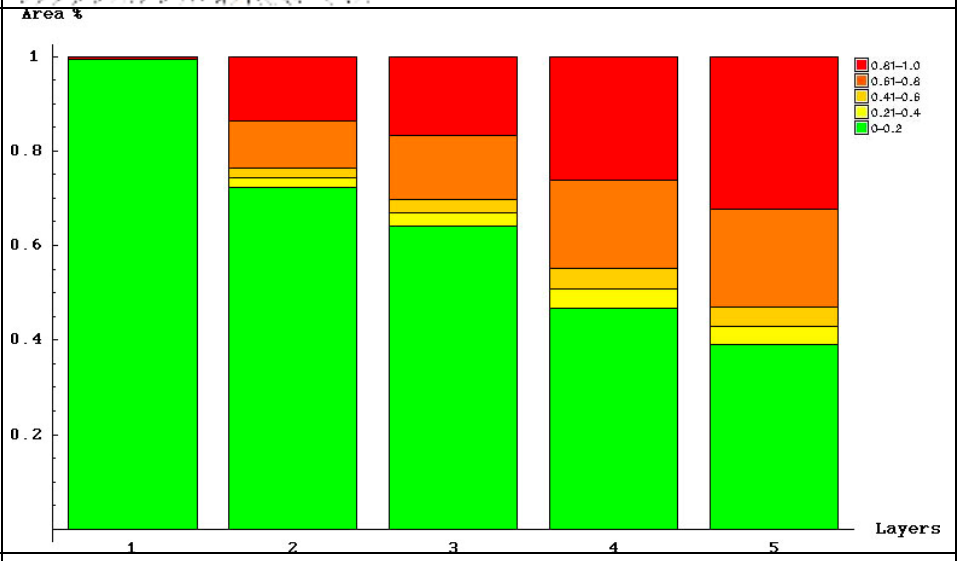

Figure 17: Variation of the stable areas with respect to time and depth. Stable areas refer to a triggering probability ranging from 0 to 20%. t1 refers to a day within the interstorm period and t2 refers to a day after the precipitation peak

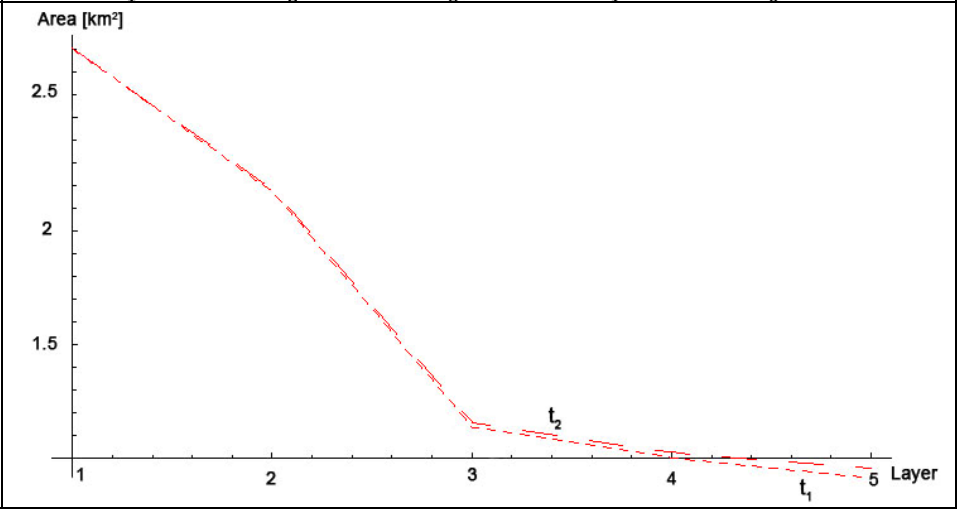

Figure 18: Variation of the areas, whose failure probability ranges from 40 to 60 %, with respect to time and depth. t1 refers to a day within the interstorm period and t2 refers to a day after the precipitation peak.

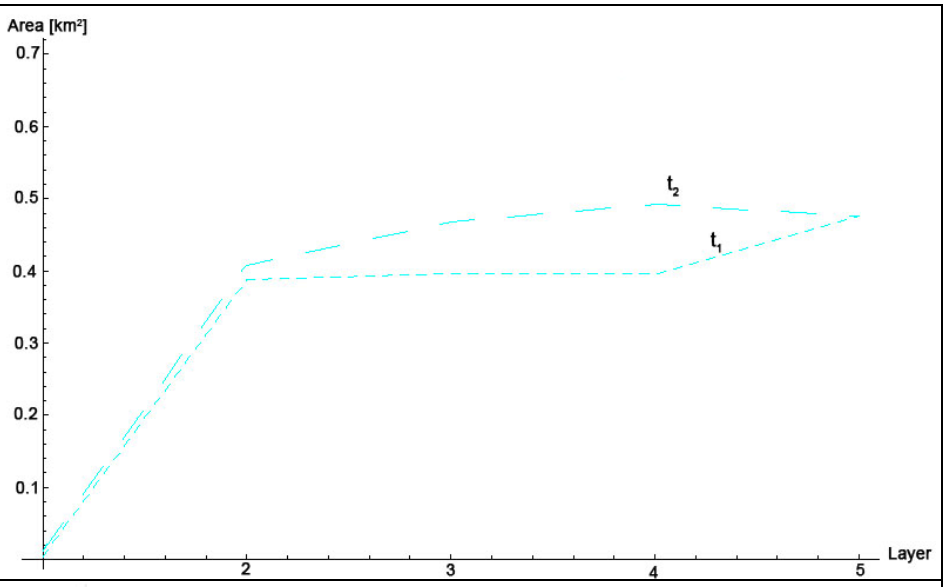

Figure 19: Variation of the areas, whose failure probability ranges from 60 to 80 %, with respect to time and depth. t1 refers to a day within the interstorm period and t2 refers to a day after the precipitation peak

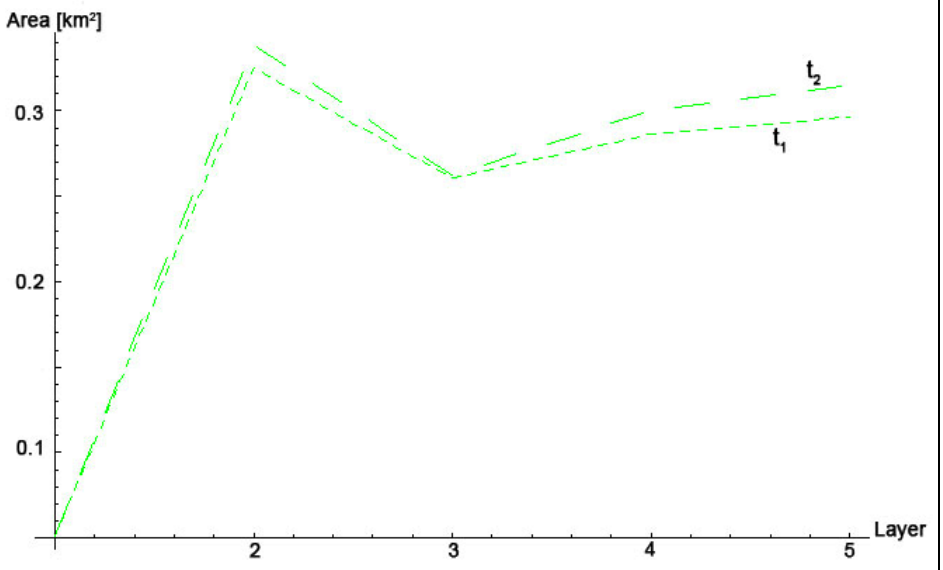

1.7 Regional investigations

Rainfall thresholds in Switzerland

Some rainfall threshold lines for debris-flow occurrence are compared with data from Switzerland in Figure 20. Two kinds of meteorological events can be distinguished for the triggering of debris flows (they are also represented by the two clusters of data points in Figure 20).

Type A events: Short thunderstorms or high-intensity downpours are likely to generate flood events in torrents which promote debris-flow formation by material entrainment along the main channel. In Switzerland, a minimal rainfall intensity of about 30 mm/h and a minimal cumulative rainfall of about 40 mm are necessary to trigger type A events. The precipitation may also partly occur in form of hail, a fact often emphasised by local observers. In Switzerland, most thunderstorm related debris flows occur in the months from June through September.

Type B events: Sustained regional rainstorms result in substantial water infiltration,

subsurface runoff and partial or complete saturation of the soil. These soil conditions favour increased surface runoff, and the soils are susceptible to slope failures which may trigger the formation of debris flows. Another triggering situation is a combined effect of rainstorm and snowmelt. In Figure 20 the two Swiss debris-flow events with an average rainfall intensity below 1 mm/h occurred during snowmelt periods.

Note that there is a considerable uncertainty in defining threshold conditions as given in *Figure 14*. The rainfall data may not necessarily be representative for the debris-flow initiation site, have a limited temporal resolution, and the relevant rainfall duration is generally unknown. Furthermore, differences in geological and hydrogeological conditions are not accounted for in the above threshold relationships which are based on data from many different areas.

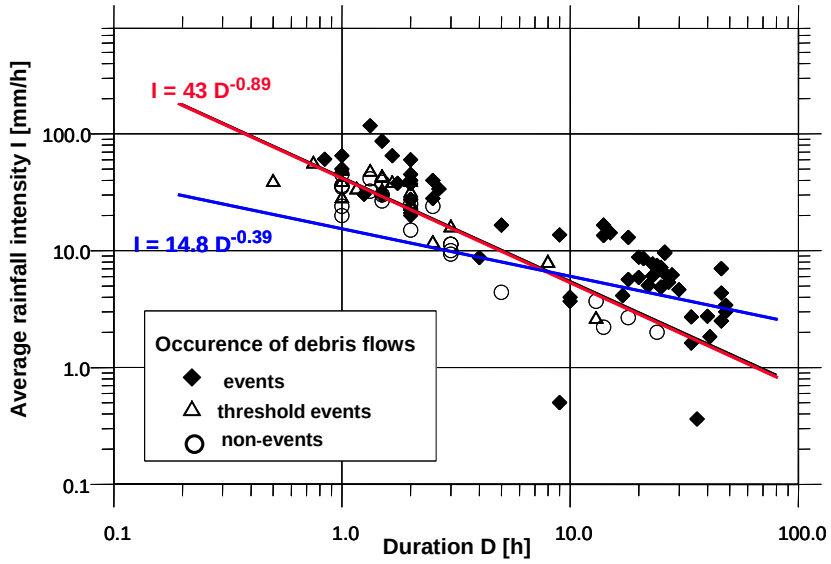

Figure 20 Relation between critical rainfall intensity and duration for debris-flow occurrence: data from the Swiss Alps (from Zimmermann et al., 1997a), and comparison with other threshold lines.

1.8 Catchment specific investigations on sediment availability

The first step to estimate the state of sediment filling of the channel is to obtain precise measurements of the soil surface. Such topographic data can be acquired on the field or from aerial photographs through stereophotogrammetry techniques. To avoid collecting complete DEMs of the channel, an optimal sampling procedure has been established which guarantees a sufficient representation of the topographic surface while measuring as few points as possible. This procedure consists in measuring "enriched" long profiles: series of cross-sections spaced out by 50 m (or less in case of abrupt slope changes) along the channel, each cross-section comprising only four well-chosen data points.

The second step is then to assess the lowest possible level for debris flow erosion. This reference level necessarily passes through all the hard points of the channel (check dams, natural rocky escarpments…). Between the hard points, however, this reference level is generally unknown, and two hypotheses have been proposed (***Figure 21***). The first one is that the reference level corresponds to the dynamic equilibrium profile between the hard points. However, it is relatively frequent to observe erosion levels

	well below this equilibrium profile, and so this hypothesis yields an upper bound for the reference level. The second hypothesis is constructed from the maximum erosion slope observed in the channel (typically, downstream of sediment traps) and is most likely to represent a lower bound for the reference level. Once both the actual topographic surface and the reference level are determined, it is relatively easy to compute the volume of sediments comprised in between (assuming a U-shape for the hypothetical cross-section eroded by debris flows). This volume represents the quantity of sediments potentially available for feeding a debris flow. In spite of the simplified sampling procedure adopted, modern topographic techniques are sufficiently precise to yield errors on volume estimates less than 10%. The main source of uncertainty comes from the determination of the basal reference level for which, at present, only extreme bounds can be drawn.
Figure 21(from Veyrat-Charvillon & Memier, 2006): The two reference levels used to estimate sediment volumes in the channel. Hypothesis A (profile a): reference level as a dynamic equilibrium slope gradient. Hypothesis B (profile d): reference level in between the equilibrium slope gradient and the observed maximum erosion slope (profile c).	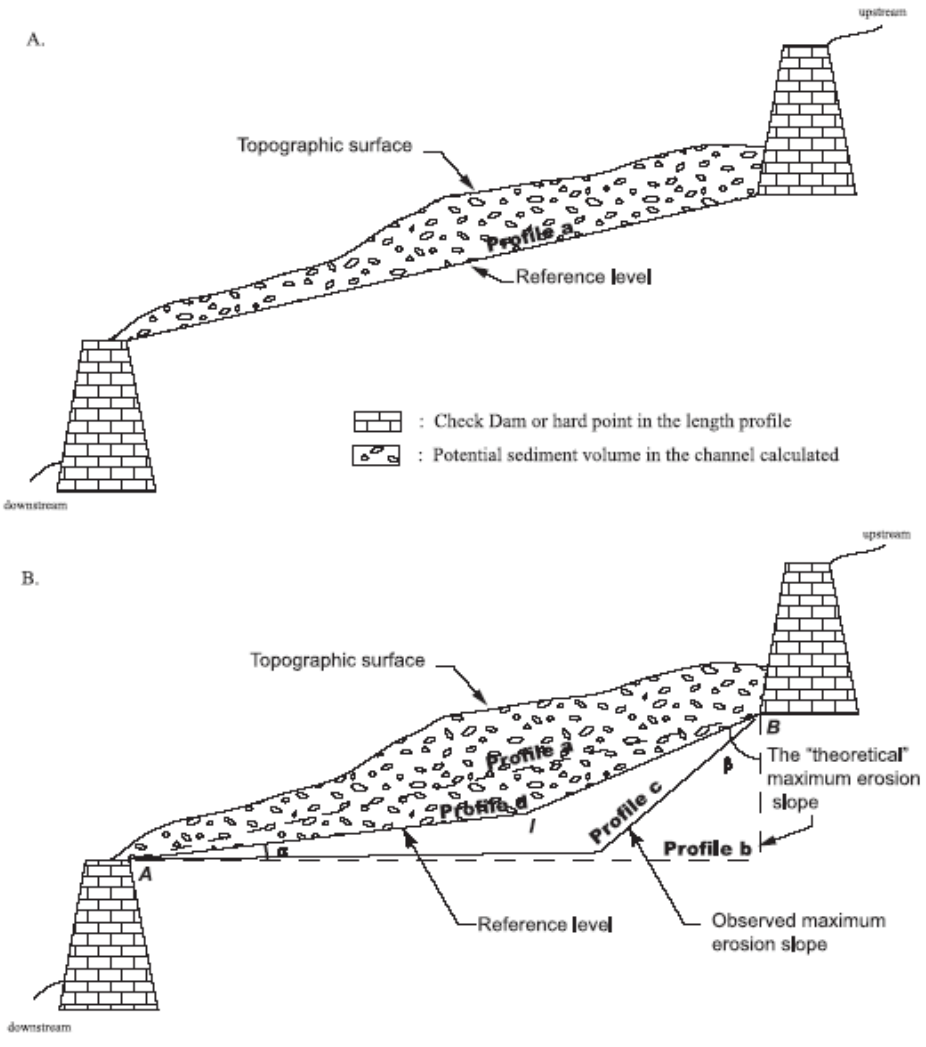
Study area	The proposed methodology has been extensively applied on a small torrential catchment located near Grenoble, France: the Manival torrent. Total drainage area of the basin is about 7 km^2, and the mean slope of the channel is 20%. The largest debris flow for which volume has been estimated, occurred in 1968 and deposited about 60 000 m3 of material on the fan. This torrent has received a considerable amount of study

	and its activity is continuously monitored since the end of the 19th century. The channel has been equipped with more than 100 checkdams and a sediment trap (on the alluvial fan) by the RTM agency. Series of aerial photograph allow to reconstructing and comparing the topography of the channel at 12 different dates since 1963, using the methodology presented above. It has been checked, in particular, that the minimum topographic level of the channel recorded during this period is effectively comprised in between the two hypotheses proposed for the reference erosion level.
Geomorphological inferences	The sediment content of the channel displays large fluctuations through time. A detailed study of the spatial distribution of the sediments led to identifying 9 homogeneous zones characterized by similar values of potential accumulation (*Figure 16*). Large values of this quantity indicate zones of preferential sediment accumulation, whereas small values denote zones of sediment transfer. In parallel, a functional mapping of the sediment-supply areas in the Manival catchment has been conducted. As shown in ***Figure 22***, the most productive areas are located in the upper part of the basin where hillslope terrains are steep and loose. This explains why zone 1, though characterized by high slopes around 20%, is an accumulation zone. Once conveyed into the channel by the various hillslope erosion processes, sediments are then transported from one accumulation zone to the next by the mean of frequent, small-scale debris flows (< 1000 m^3) triggered by hydro-meteorological events.

Figure 22(from Veyrat-Charvillon & Memier, 2006): Maximum specific potential accumulation (in m3/m2) of the 70 reaches initially defined in the Manival channel. This quantity is computed as the difference in specific volume between the states of maximum and minimum sediment accumulations recorded for each reach during the period of the study (1963-2000).

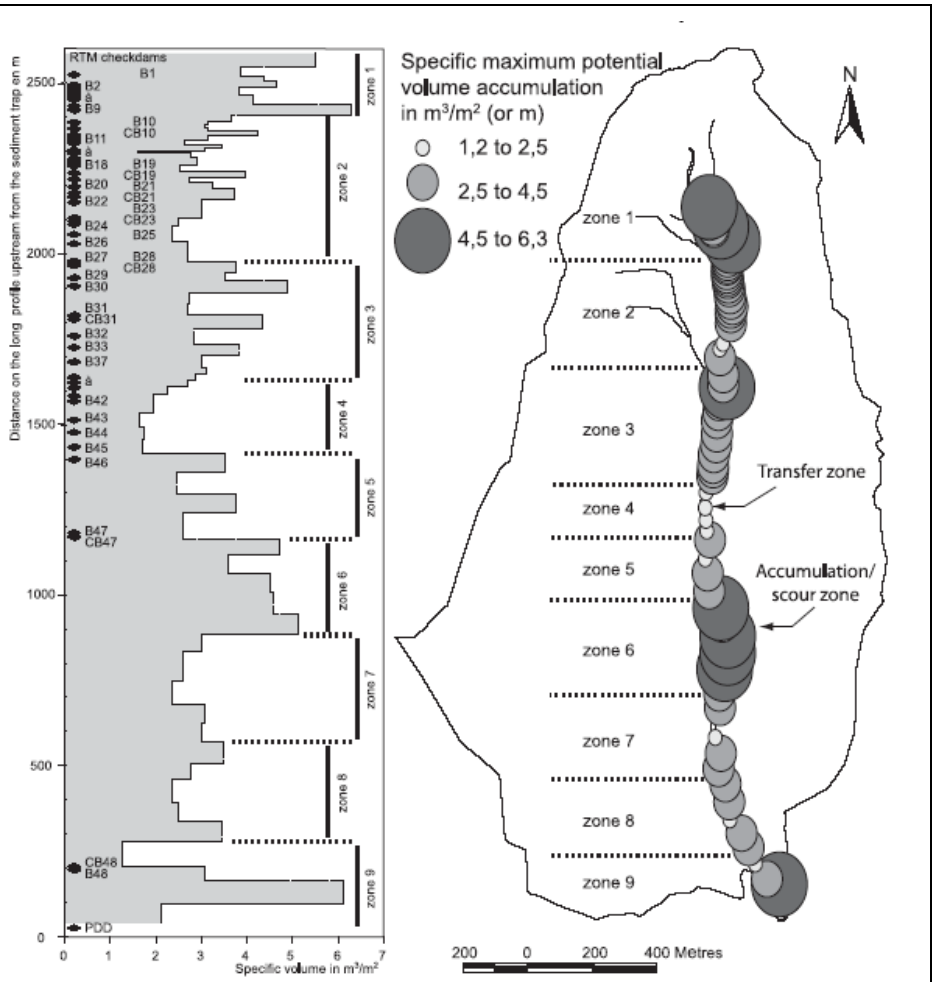

Figure 23 (from Veyrat-Charvillon & Memier, 2006): Functional map of the sediment-supply areas for the Manival torrent catchment. The method used to establish this map is developed in Veyrat-Charvillon (2005). As shown, ten classes have been defined corresponding to combinations of 4 different criteria (channel connectivity, vegetation, lithology, geomorphology), and each class is then associated to a qualitative index of sediment productivity. Note that this determination key does not account for large-scale mass movements (such as large landslides for instance), which are absent from the Manival catchment.

A. 3-D vue of the Manival watershed (orthophotography drapped on V-DEM with ErMapper software).

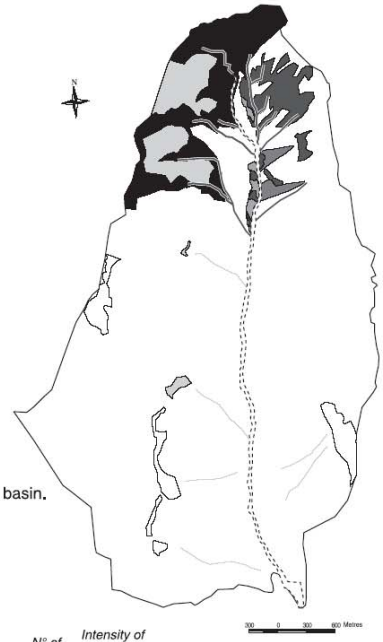

B. Functional map realised on Manival basin.

C. Determination key of sediment supply showing the different classes used for the mapping.

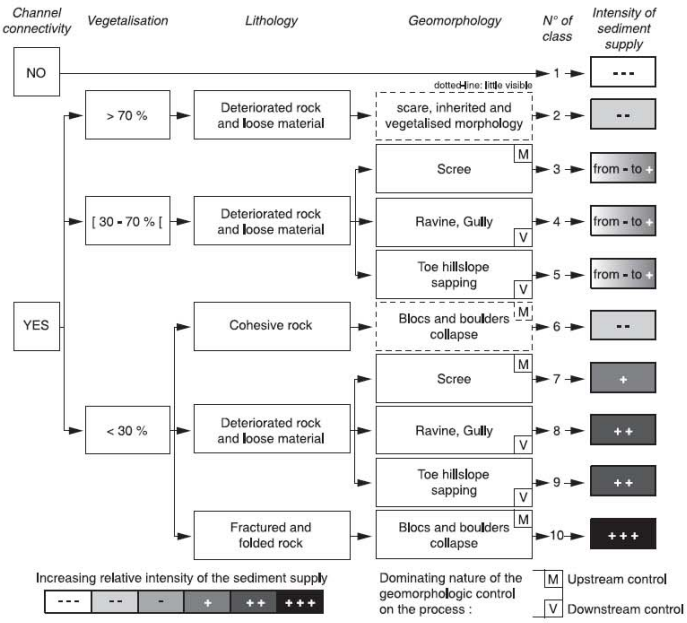

Interestingly, the state of sedimentary filling of channel upper zones appears well correlated with the average annual precipitations recorded in a nearby meteorological station (***Figure 23***). This indicates that the geomorphic processes that are responsible for the progressive migration of the sediments from the hillslopes towards the channel are activated by large cumulated precipitations, in particular if these precipitations occur during winter time. On the contrary, the processes responsible for the progressive transfer of the sediments along the channel (micro-debris flows) appear to be disconnected from the cumulated precipitations: they are rather triggered by intense and localized storms occurring preferentially during summer.

Figure 24(from Veyrat-Charvillon, 2005): Relation between variations in sediment accumulation for the 9 homogeneous zones defined in the Manival channel (in m3/year: histogram) and annual precipitations recorded in the nearby station of St-Pierre de Chartreuse. The dotted line represents the annual cumulated precipitations, and the full line represents the averages over the periods for which sediment data are available.	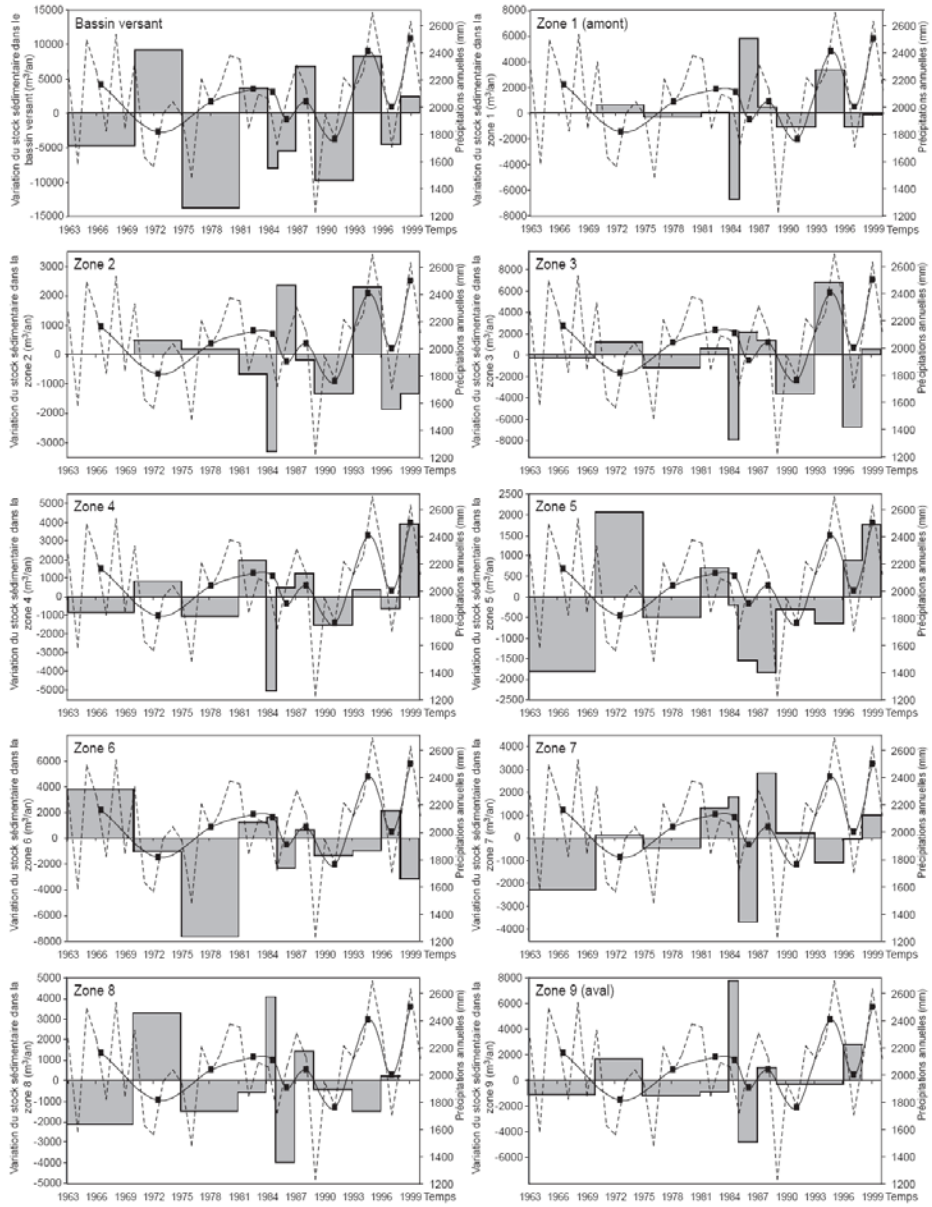
	The knowledge of sediment volumes stocked inside the channel at various dates, combined with the records of the sediment outputs on the fan (periodically extracted from the terminal sediment trap and from the channel) also permits to establish partial sediment budgets of the catchment. From these, it has been possible to compute estimates of specific erosion rates for the sediment-supply areas. The average value obtained is about 7.6 mm/year, and appears to be compatible with values reported in the literature for similar types of terrains. This constitutes a further validation of the methodology adopted to study the sedimentary filling of the channel.
Proposal of a new method	The detailed study of the sedimentary dynamics of the Manival catchment led the author to propose a new predictive method to assess: (1) the probability of occurrence of a major debris flow; (2) the maximum potential volume of this debris flow.

Occurrence of a debris flow: SPOTS zones	The migration of sediments in a torrential catchment is mediated by a large number of geomorphic processes occurring over various space- and time-scales. From the hillslopes, sediments are progressively fed into the channel where they are temporarily stocked prior to eventually transform into a debris flow. The channel thus plays a key role in the dynamics of this complex system. Furthermore, close inspection reveals that sediment filling is not uniform inside this channel: There exist a certain number of characteristic zones in which sediments preferentially accumulate. These are called SPOTS zones. Partially-filled or empty SPOTS zones tend to stop debris flows that have formed upstream. Hence, the probability for a debris flow to reach the alluvial fan is small in this case, limited to extreme hydro-meteorological events. On the contrary, a complete filling of all the SPOTS zones is the sign of a huge probability for a large debris flow to occur, even in case of a moderate hydro-meteorological event. Accordingly, the observation of the filling state of the SPOTS zones constitutes a good indicator of the probability for a debris flow to reach the alluvial fan. At present, this indicator is only qualitative but it is expected that detailed studies in the future may lead to quantitative probability assessments based on the SPOTS zones The identification of these SPOTS zones is direct when one is able to reconstruct the sedimentary history of the channel through time. In general, however, this is not possible. The Manival case shows that these zones systematically correspond to slope reductions or to enlargements of the channel. More precisely, one observes that the slope factor only is sufficient to fully characterize these zones (because channel width is generally correlated to slope): SPOTS zones correspond to local concave slope ruptures. This criterion can be used to directly determine SPOTS zones by visual inspection on the field. In principle, an objective localization of these zones using long profiles is also possible, but proved to be rather imprecise due to the large errors introduced when computing linear slopes from topographic data.
Potential volume of the debris flows: PREVENT method	As stated above, the determination of the amount of sediments stocked inside the channel should give a direct estimate of the maximum potential volume of a debris flow. However, it turned out in the case of the Manival torrent, that the stocked volume may at times reach more than 260 000 m^3, and constantly oscillates around an average value of 100 000 m^3. Such values are much larger than the volume of the largest debris flow observed in this torrent (60 000 m^3). Hence, the author proposed to limit the sediments taken into account in the volume calculation by introducing a slope criterion: Only channel reaches whose slope exceeds 8% will be considered in the estimation of debris flow volumes. This method is called PREVENT. The justification for this threshold is the commonly-accepted observation that debris flow fronts tend to decelerate, and even stop, on slopes less than 8%. Consequently, the erosive power of a debris flow on slopes less than 8% is likely to be very weak. *Table 2* show the results of the PREVENT method for the Manival torrent. On average, the volume of sediments stocked in slopes exceeding 8% is of the order of 50 000 m^3. This value is in very good agreement with the volumes of the known debris flows that occurred in this torrent.

Table 2 (Veyrat-Charvillon, 2005): Sediment volumes (in m3) potentially available for a debris flow in the Manival channel, calculated according to the PREVENT method. For each date, the two values corresponding to the two extreme hypotheses on the reference erosion level are given, as well as the average value.

Date	Volume en amont du barrage RTM n°47 (Pente du chenal supérieur à 8°)		
	Hyp.minimaliste (PLAN sup.)	Hyp.maximaliste (PLAN inf.)	Médiane
1963	44 401	64 866	54 633
1970	27 788	52 387	40 087
1975	48 630	78 279	63 454
1981	34 222	60 591	47 406
1984	43 690	68 512	56 101
1985	25 580	45 318	35 449
1987	38 959	63 938	51 449
1989	41 597	65 778	53 688
1993	18 993	42 144	30 568
1996	53 750	78 407	66 079
1998	34 985	59 514	47 250
2000	41 730	68 791	55 260
Moyenne	37 860	62 377	50 119

Application to two other torrents

To validate the proposed method, it has been applied to 2 other torrents located near Grenoble: the Merdaret torrent and the Arches torrent. These two torrents share common characteristics with the Manival: they are all clearly supply-limited, and the source of sediments is relatively localized in the upper basin (scree, rockfalls,…). The sedimentary filling of the channels has been determined using both field surveys and aerial photographs. This allowed to determining the characteristic SPOTS zones and to estimate the volumes of the maximum potential debris flows. The obtained values proved in good agreement with the volumes of known debris flows recorded in these catchments.

Chapter 2

ROCK AVALANCHES

Defining rock avalanches

Rock avalanching is the extremely rapid (>30 m/s), flow-like movement of large volumes (>10^6 m^3) of rock being increasingly fragmented during the runout process.

From a physical perspective, rock avalanches (or "sturzstroms"; Hsü [1975]) are extremely rapid granular mass flows, often involving solid, liquid, and gaseous phases [Hungr et al., 2001]. The unusual long runout produced by rock avalanching cannot be readily explained by conventional friction physics, and a number of semi-quantitative as well as mechanistic theories have attempted to explain the excess travel distance.

Rock avalanches differ from *volcanic debris avalanches* in that they usually contain less water during motion, and in that their movement gives rise to catastrophic comminution of rock particles down to sand and silt size. This characteristic fragmentation effect during flow motion is what distinguishes rock avalanches from large rock(-block) slides, in which large parts of the moving mass remains more or less intact.

3.1 Modelling Approaches

Introduction

Why model?

The modelling of large catastrophic landslides in general, and long-runout rock avalanches in particular, is of interest for several reasons. First, the encapsulation of what appears to be a highly energetic and destructive process of relief destruction is of intrinsic interest to geosciences in terms of its mass-transport capability and resulting

	landform changes, particularly disciplines such as process geomorphology, Quaternary geo(morpho)logy, or long-term landscape evolution. The process of rock avalanching itself, however, poses many interesting questions and challenges to analytical and fluid mechanics, the physics of Coulomb friction and granular mass flows, as well as conservation of mass and energy. From an applied perspective, modelling of rock-avalanche dynamics and their runout is of utmost interest to natural hazard and risk management. Model outputs should ideally serve to spatially delineate the area of direct physical impact from a spreading rock-avalanche deposit as a function of well-defined initial and boundary conditions, such as, among others, the initial volume of the rock avalanche, and the surrounding valley geometry. To be effective, hazard map zonation further requires a combination of these simulated final runout dimensions together with estimates of the average recurrence interval for a defined event volume.
Types of models	Four main types of models have governed research on the causes, dynamics, and geomorphic effects of rock avalanches: • empirical (semi-quantitative) models; • physical ("sand-box") models; • geophysical (site-specific) models; and • numerical process models. Though each of these model types have their advantages and disadvantages, they have served to promote our knowledge on the phenomenon of rock avalanches and related granular mass flows and rapid mass movements, in general. The following overview gives a brief summary of the input requirements, underlying assumptions, applicability, and limitations of various models used to explain the physics of rock avalanches.
3.2 Types of Models	
	3.2.1 Data input requirements
Initial topography	The success of any modelling effort in terms of reliably predicting rock-avalanche runout is strongly dependent on the quality and accuracy of input data for initial and boundary conditions. Generally speaking, for any model, the quality of the output is determined by the quality of its input. For large rock avalanches, this poses an interesting and far from trivial problem, since

	the initial conditions for many events remain poorly defined or mostly unknown. Only in a number of historic occurrences is it for instance possible to reconstruct the initial, i.e. pre-failure, topography from photography, topographic maps, or ideally, even digital topographic data. Geotechnical back analyses only address the limit force equilibria prior to failure, while only indirectly indicating any requirements of the pre-failure topography. Likewise, volume estimates of rock-avalanche deposits may differ quite substantially from those of source areas, even when they are seemingly obvious and well-defined by topographic break lines, such as amphitheatre-shaped detachment areas [e.g. Abele, 1974]. Likewise, the initial internal rock-mass structure of the original source area, which may have exerted considerable control on the shape and size of the detaching rock mass, is usually intractable to reconstruct. The problem of initial conditions is much easier dealt with in terms of the causes and trigger mechanisms of rock avalanching, since most models are designed to commence at the onset of the failure process without prior knowledge on the underlying process history. For event-based triggers such as earthquakes or rainstorms, this instance may be applicable, although there remains in some cases the problem of potential initial motion prior to catastrophic failure (see below).
Runout behaviour and valley geometry	The topography of the failure site and its immediate surroundings are important boundary conditions for modelling the runout characteristics of rock avalanches. Nicoletti and Sorriso-Valvo [1991] demonstrated that the runout behaviour of rock avalanches may be a function of major landform elements in the runout zone. However, several studies have also shown that large rock avalanches may obliterate minor valley-floor landforms, and, in exceptional cases, contain phases of pure falling motion without significant bedrock contact [Heim, 1932], or even override minor interfluves [e.g. Hewitt, 1998; McSacveney, 2002], representing extreme cases of the typical phenomenon of swash or run-up on opposite valley flanks. Typically, sudden impact of the moving rock-avalanche mass against major obstacles such as the juxtaposed valley flank may also cause substantial diversion of the bulk rock mass of directions normal to that of initial movement, usually along the major valley axis, causing a characteristic L-shaped deposit planform to develop. Hence, it is critical to capture the three-dimensional valley topography below the detachment area on a 10^1-km scale as accurately as possible. This should also include any water bodies in the runout path, since the fragmentation mechanics and runout behaviour of rock avalanches will significantly differ when in contact with underlying water bodies. The corresponding and newly emergent field of research on landslide tsunami [Pedersen et al., 2002] deals predominantly with the dimensions and propagation of displacement waves as the main issue of concern [e.g. Lynett and Liu, 2005; Panizzo et al., 2005],

	whereas the actual runout underwater is only of secondary concern.
Flow conditions	Other critical parameters to calibrate models of rock-avalanche dynamics and runout include estimates of flow conditions, which usually address a mean or maximum velocity of the moving mass. Similarly to debris flows, several rock avalanches have been documented to show effects of superelevation, especially where they have been subject to channelization along major valley axes. This superelevation effect can be exploited to infer mean flow velocities. Clavero et al. [2002] used impact marks of projectiles from volcanic debris avalanches on exposed rock surfaces to infer the flow velocity required.
	3.2.2 Underlying assumptions
	Iverson [2003] recently summarised the basic approaches and shortcomings to the modelling of runout of large landslides. Many of his findings also apply to rock avalanches. On the process side, however, a considerable range of sometimes diverging theories have addressed the unusual runout of rock avalanches with regard to conventional frictional theory.
Coulomb friction – applications and limitations	One of the earliest approaches to model the runout of rock avalanches was undertaken by Heim [1932], who used a Coulomb slide-block model, based on Newton's second law: $$\rho h \frac{dv}{dt} = \rho g h \sin\theta - \rho g h \cos\theta \tan\phi \quad (3.1)$$ where ρ is density of a rigid rock mass; h is its (uniform) height; v is velocity; t is time; g is acceleration due to gravity; θ is hillslope angle; and ϕ is the Coulomb friction angle, i.e. the ratio of shear to normal forces at the sliding plane. This important rock property is readily obtainable from laboratory experiments ($30° < \phi < 40°$), and has therefore greatly contributed to the popularity of this approach. Integration of equation (3.1) over travel distance x, while implicitly assuming a point mass with zero volume, yields the well-known morphometric characterisation $$\frac{H}{L} = \tan\phi \quad (3.2)$$ where H is the maximum vertical drop height of the rock avalanche, i.e. the vertical elevation difference between its crown scarp and deposit toe; and L is the maximum runout length. Scheidegger [1973] interpreted the ratio in equation (3.2) as the coefficient of internal friction of a given rock avalanche. The most important limitation to this simple model comes from empirical

	observations of rock-avalanche runout L, which beyond a somewhat diffusely defined "threshold" volume $V \sim 10^6$ m^3, is higher than predicted by the range of typical values of ϕ in equation (3.2). In other words, larger rockslide and rock avalanches do travel for longer distances than one would expect from conventional frictional theory. This is the reason, why simple sand-pile laboratory experiments do not represent the mechanics of large rock avalanches in the field [Davies and McSaveney, 1999]. A measure of this "excess runout" was proposed by Hsü [1975]: $$L_e = L - \frac{H}{\tan 32°} \quad (3.3)$$ assuming that $\phi = 32°$ would represent a typical angle of friction. L_e however scales somewhat systematically with V over several orders of magnitude, and hence remains unaccounted for when using both point-mass assumptions and a Coulomb friction term as in equation (3.1). Dade and Huppert [1998] extended this empirical prediction potential by a formulation based on the conservation of energy: $$A = \lambda^{1/3}\left(\frac{gMH}{\tau}\right)^{2/3} \quad (3.4)$$ where A is the total area covered by the rock-avalanche deposit; λ is the mean width-length ratio of the rock-avalanche deposit; M is deposit mass; and τ is resisting shear stress.
The case for low basal friction	As Iverson [2003] notes, there have been several modifications of equation (3.1) to include e.g. changes in mass resulting from entrainment or deposition during runout [Hungr and Evans, 2004]. However, in some way or the other they neglect to satisfyingly address basic physical constraints, such as conservation of mass or momentum. Conservation of volume, which is employed for studying extraterrestrial long-runout rock-slope failures [e.g. Barnouin-Jha et al., 2005]: $$\frac{\partial h}{\partial t} = \frac{\partial}{\partial x}(hu) = 0 \quad (3.5)$$ where u is mean rock-avalanche velocity; is a premise not directly applicable to rock avalanches (or other large landslides, for that matter), given the importance of dilatance of the moving mass, and any processes of entrainment or deposition during motion [Hungr and Evans, 2004]. Nevertheless, the observed excess runout of rock avalanches has invoked various a number of physically-based theories that advocate modes of reducing internal and/or basal friction in a way that would allow for the extreme travel distances observed.
Lubrication due to gas and fluid pressures	Early avenues of explanation postulated that trapped air cushions below the moving rock-avalanche mass, or entrainment of groundwater-saturated valley fills would

	rock-avalanche mass or entrainment of groundwater-saturated valley fills would produce high enough fluid pressures to sufficiently reduce basal friction during motion [Abele, 1997]. The generally higher pore-water water content in "cold" volcanic debris avalanches or mixed ice/rock avalanches indeed appears to produce much higher runout (>10 km; Capra and Macías, 2002; Shang et al., 2003; Huggel et al., 2005], and lower values of mean deposit thickness, than for non-volcanic rock avalanches. The detection of giant rock avalanches on extraterrestrial bodies such as the Moon or Mars [e.g. Barnouin-Jha et al., 2005; Bulmer and Zimmerman, 2005], however, casts serious doubts on the need of additional lubricant media to produce excess runout (although there are circular arguments that spell out the necessity of extraterrestrial liquid water for producing such phenomena). Moreover, Brodsky et al. [2003] argued on the basis of teleseismic data of three large volcanic debris avalanches that volcanic gas would not affect the apparent friction during motion.
Acoustic fluidisation	Another attempt to explain L_e is that of acoustic fluidisation, during which "transient, high-frequency pressure fluctuations, generated during the initial collapse and subsequent flow of a mass of rock debris, may locally relieve overburden stresses in the rock mass and thus reduce the frictional resistance to slip between fragments." [Collins and Melosh, 2003].
Processed image of field photograph of right-hand flank of the 1987 Val Pola rock-avalanche deposit close to the slope foot (65 m^2, 6272 fragments) [Crosta et al., 2007].	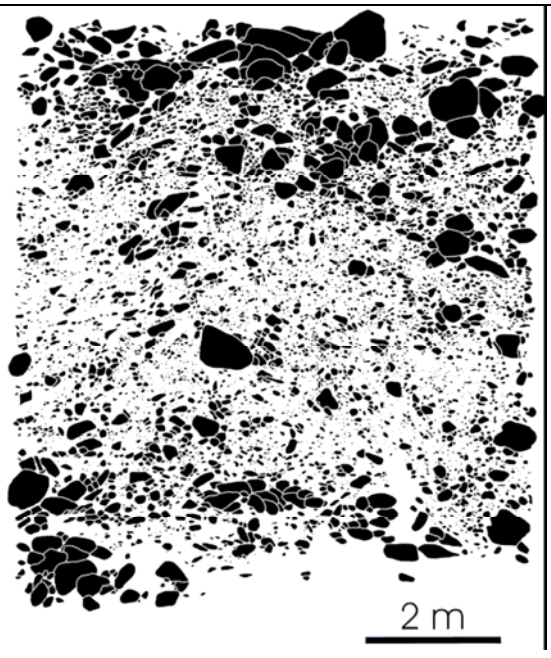
Dynamic fragmentation	A recently developed theory introduces the concept of dynamic fragmentation associated with high dispersive pressures due to close grain-to-grain interactions, which lead to break up of clasts along failure surfaces [Davies et al., 1999]. This fragmentation-driven dispersive force P_f can be expressed in one-dimensional terms as

	$$P_f = -c\frac{\partial d}{\partial x} \quad (3.6)$$ where c is a dimensional constant, d is the depth of the moving rock avalanche at longitudinal position x [Davies and McSaveney, 2002]. Importantly this theoretical approach does not require the initial rock mass to be jointed in any way at initial detachment time $t = t_0$, nor does it require the moving rock mass to contain and/or entrain any potential "lubricants" en route. Moreover, it explicitly accounts for the often observed comminution of rock-avalanche deposits with a grain size distributions that have a fractal dimension similar to that recently produced by a 3D granular shear model of a lattice solid [Abe and Mair, 2005]. Hence, it is one of the few physical-based theories that addresses the important effect of variable grain size distributions during motion. The theory of fragmentation also challenges the assumptions of homogeneous and constant mechanical properties of rock avalanches during flow common to many numerical runout models. There is abundant field evidence for fragmentation in rock-avalanche deposits [e.g. Davies and McSaveney, 2002; Dunning, 2006, Crosta et al., 2007]. Crosta et al. [2007] conducted a particle size analysis of the 1987 Val Pola, Italy, rock-avalanche deposit, showing that a fractal (power-law) distribution yielded the best fit to this particular deposit. Based on the obtained fractal dimension, they were able to relate the energy required for fragmentation during rock avalanching to the initial potential energy. They also noted that segregation of particles was negligible apart from locations in the bouldery carapace or at the front of the deposit, while demonstrating the possibility for various populations of particles.
Plot of the energy required for fragmentation, computed by different approaches, with respect to available potential energy as a function of fractal dimension. Hatched area represents the interval of the most frequent values computed for the 1987 Val Pola rock avalanche deposit [Crosta et al., 2007].	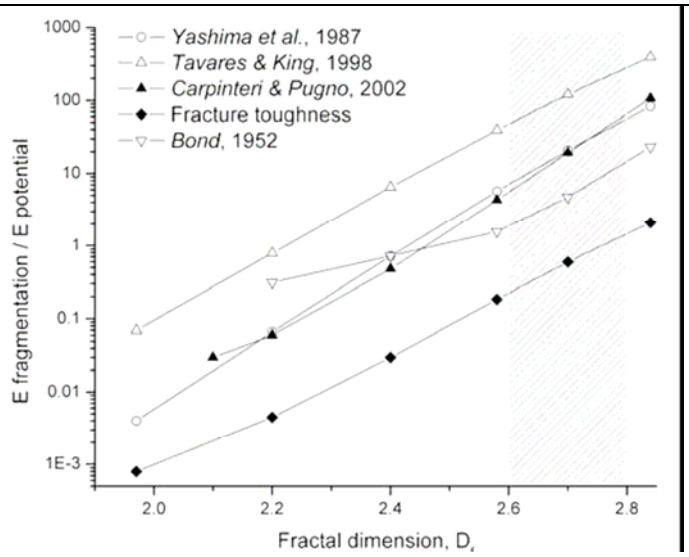
Granular models	The physics of granular flows provide further insight into modelling of rock avalanches, although not all features observed in nature can be faithfully reproduced in laboratory experiments [Friedmann et al., 2006]. Ward and Day [2006] presented a

	new modelling approach that involved the motion of independent particles under the influence of topographically derived gravitational and centripetal acceleration. They used random perturbations along and across particle tracks to simulate the frictional dynamics, particle-to-particle interactions, fluctuating basal contacts, and topographic roughness. This model was tested for the 1980 Mount St Helens debris avalanche, and gave promising preliminary results. The introduction of a random component into this granular model, however, does not contribute to a better understanding of the governing physical processes, nor does it consider the fractal nature of particle fragmentation discussed above.
Qualitative models	Other, empirical, model approaches have remained more qualitative, yet nonetheless taking into account detailed field observation of the surficial and internal geometry of rock-avalanche deposits. Valuable information can be gained from such studies, especially when they document the entrainment of material other than from the rock avalanche itself [e.g. Pollet et al., 2005]. The same applies for detailed investigations of rock-mass properties in rock-avalanche detachment areas, which in some cases may contain critical rock-mass defects or antecedent shear [Weidinger et al., 2002; Friedmann et al., 2003].
Constraints from petrography and sedimentology	One such important field observation concerns the occurrence of micro-shears together with so-called frictionite or pseudotachylyte, a glass-like material found in thin discontinuous layers along the basal shear planes of very large ($V > 10^9$ m^3) rockslide/rock avalanches, mainly composed of crystalline rocks [Erismann et al., 1977]. For the case of the famous 2.5×10^9-m^3 Köfels rock avalanche, Austria, Sørensen and Bauer [2003], estimated the necessary increase in temperature at the moving rockslide base $$\Delta\Theta = \frac{u^2 h}{2 c_p \delta} \quad (3.7)$$ where is Θ is temperature; c_p is specific heat capacity of the heated rock; and δ is the thickness of rock heated in the vicinity of the basal shear surface. Occurrence of such material was argued to indicate frictional melting and rock degassing without any significant decreases of u during motion. Nevertheless, there are very few documented occurrences of landslide-related frictionite, i.e. the one at Köfels, two mega-rockslide sites in leucogranites of the High Himalayas [Weidinger et al., 2002; Weidinger and Korup, in press]; and below the Arequipa volcanic debris avalanche deposit, Peruvian Andes [Legros et al., 2000]. This suggests that energy dissipation during rock-avalanche motion rarely takes place at the basal shear surface exclusively [Crosta et al., 2003].

	3.2.3 Simulating the disposition, dynamics, and runout of rock avalanches
Disposition models of rock avalanches	There are very few physical experiments that take into account any antecedent rock-mass defects or structural lineaments that may render rock-slopes conducive to catastrophic rock avalanching. Bachmann et al. [2004] used a sand-box model to investigate the scaled failure behaviour of large rockslides triggered by accelerated ground motion, and which were preconditioned by large fracture patterns. They argued that the initiation of deep-seated rockslides, which may deteriorate to rock avalanches, was defined primarily by the mechanical structure of upper hillslopes and pre-existing weathering rather than by the occurrence, which seemed to largely control the shape and size of the failure volume.
Rock-avalanche dynamics and runout	There exists a number of numerical models that were developed to simulate the runout of granular flows, and which have been applied to rapid mass movements of the flow type. The practical application of models of granular flows were also the subject of the previously EU-funded project DAMOCLES ("Debrisfall Assessment in Mountain Catchments for Local End-Users"; Contract No. EVG1-CT-1999-00007), and Crosta et al. [2001; 2003] provide a good overview on available models and underlying assumptions. McDougall and Hungr [2004] further developed the continuum mechanics process model of Hungr [1995] for the analysis of motion of rapid flow slides, debris flows, and avalanches across three-dimensional (3D) terrain, based on the physical principles of mass and momentum conservation. Importantly, their model takes into account the effects of centripetal acceleration on rock-avalanche motion due to curvature of the underlying slopes: $$\sigma_z = \rho h(g\cos\alpha + v^2\kappa_z) \quad (3.8)$$ where σ_z is bed-normal stress; h_z is the bed-normal flow depth; α is the inclination of the x-y plane from the vertical; v is depth-averaged flow velocity in the direction of motion; and κ_z is the bed-normal curvature of the flow path in the direction of motion. They defined the frictional rheology at the bed by: $$\tau_{zx} = \frac{v_x}{v}\sigma_z \tan\phi_d(1-r_u) \quad (3.9)$$ $$\tau_{zy} = \frac{v_y}{v}\sigma_z \tan\phi_d(1-r_u) \quad (3.10)$$ where τ_{zx} and τ_{zy} is bed shear stress opposing the direction of motion; v_x and v_y are the components of velocity v in the x- and y-direction, respectively; r_u is the ratio of pore pressure to total bed-normal stress; and ϕ_d is the dynamic basal friction angle. Pirulli

	[2004] has adapted this model for simulating the runout of three large rock-slope failures in the European Alps. Crosta et al. [2004] used a similar 3D runout model based on Voellmy rheology within a Lagrangian frame of reference to model the travel distance and deposit shape of the 1987 Val Pola rock avalanche, Italy, Denlinger and Iverson [2004] developed model of granular avalanche-type landslides across 3D terrain solely on the basis of continuum mass and momentum conservation, and stress generation between moving grains controlled by Coulomb friction. The obvious advantage of this model and the one of McDougall and Hungr [2004] is their applicability to rock avalanches, snow avalanches, debris flows, and pyroclastic flows alike, highlighting their general physical principles and interrelationships. What is more, the prediction potential of the model was directly tested and verified by physical laboratory experiments involving the avalanche-like movement of dry sand over 3D terrain [Iverson et al., 2004]. The majority of these models are based on physical laws from fluid dynamics and based on conservation of mass or energy. However, Chemenda et al. [2005] note that, although numerical modelling appears to be the most powerful simulation tool for large landslides at present, physical lab experiments may be more appropriate to compensate for difficulties experienced when numerically modelling 3D brittle failures and large inelastic strain. Based on the same physical principles, Kelfoun and Druitt [2005] presented a model for the catastrophic dry volcanic debris avalanche derived from a sector collapse of Socompa volcano, Chile, by assuming a constant retarding stress during runout, while using the surficial deposit morphology as well as its runout as further constraints for calibration. Thus it is not surprising that very few models explicitly address the effect of rock-mass fragmentation and comminution during rock-avalanche motion, especially given that many rock avalanches initiated as more or less intact rock blocks. Smith et al. [2006] employed such a fragmentation term in the DAN model, and produced a runout very similar to that of a medium-sized rock avalanche. Gray et al. [2003] provided model expressions of describing the flow of granular avalanches around obstacles in their runout, using hydraulic theory, and thus contributed to the little studied process interactions of granular avalanches with local topography or even structural countermeasures. Other recent approaches such as the RASH^{3D} model of Pirulli et al. [2006] have employed the St. Venant's Equation which is used in fluid dynamics.

3.3 Interpretation and Discussion of Model Results	
	In summary, there exists a range of models for describing and explaining the physical behaviour of rock avalanches as prime examples of fragmenting granular flows. While empirical approaches are useful first-order approximations to encapsulate the phenomenon with few readily obtainable parameters, their limitation lies in their lack of spatial explicit predictions. A range of one- to three-dimensional numerical models overcome this problem, hence paving the way for providing spatial information on the expected runout of a rock avalanche, given adequately specified initial volume and valley topography. However, the extraordinary runout of large rock avalanches remains the most crucial problem for numerical simulations. Many of the physically-based numerical runout models are readily calibrated for single events, and produce satisfying results for simulating the runout. Few studies have provided rigorous tests or comparisons of the range of model solutions. Sheridan et al. [2005], for example, used the well-documented characteristics of small historic debris avalanches on Mount Rainier, Washington, USA, to compare and evaluate the sliding-block based FLOW3D model with the Titan2D mass-flow model, which is based on solutions to the shallow-water equations adapted for granular flows. As a general observation, most of these models remain hardly applicable to other sites with differing initial and boundary conditions. The recent occurrences of ice/rock avalanches with runout >10 km [Shang et al., 2003; Huggel et al., 2005] demonstrate that rock avalanches are possibly just elements within a continuum of complex multi-phase granular flows, the range of which is presently intractable to formulate with the given set of algorithms within a single model. Nonetheless, applying the principles of mass and momentum conservation and continuum physics allows a much broader spectrum of applicability of these models, encompassing a broad range of granular flows in general already, and in particular the types of extremely rapid mass movements dealt within IRASMOS. One of the crucial research gaps thus lies in rigorous tests of the transferability of not only numerical runout, but also the remaining three other types of models on rock avalanches.
3.4 Model transferability	

	The key problem with many of the available models on rock-avalanche dynamics and runout is that they work well for the single case they have been calibrated, though fail to predict in any satisfying way the characteristics of other rock avalanches. Few models that have been derived for a specific site have been successful to adequately predict runout of rock avalanches at other sites, while the most comprehensive modelling approaches have mainly dealt with a single, usually well-documented, event for calibration. Even simple empirical approaches to constraining and comparing the geomorphometric characteristics of rock avalanches within or across various mountain belts subject to differing environmental boundary conditions experience order-of-magnitude scatter of data even in log-log space [e.g. Abele, 1974; Nicoletti and Sorriso-Valvo, 1991; Corominas, 1996; Legros, 2002]. Other important problem relate to the initiation and termination phases of rock avalanches, as there are several cases, where process domains cannot be distinguished discretely. There are a number of cases where deep-seated gravitational slope deformation, "sackungen" [e.g. Chigira et al., 2003; Ambrosi and Crosta, 2006], or rock flow [Cruden and Varnes, 1996] preceded catastrophic rock avalanching. Thus, some important initial conditions of rock avalanching, such as their initial volume, may be contained in or even dictated by the type and pattern of differential slope deformation. Numerical modelling of 3D rock-slope stability and ongoing deformation is largely based on finite-element or finite-difference codes [e.g. Stead et al., 2006]. There have been some modelling efforts of deep-seated gravitational deformation on the basis of a visco-plastic constitutive law which allows for effects of strain softening [Forlati et al., 2001]. Helmstetter et al. [2004] argued that a slider-block model would further provide a physical rationale to the commonly observed and empirically constrained inverse velocity law, which serves as one way to predict with considerable reliability the catastrophic failure of a rock-slope failure subject to initial and gradually accelerating creep movement. Clearly, the process continuum between slow rock-slope deformation and catastrophic failure requires future research to possibly couple models of deformation and runout. Likewise, many large landslides, including rock avalanches, may at some stage transform into channelized debris flows, e.g. after having entrained a critical amount of water along the runout track [e.g. Plafker and Ericksen, 1978; Boultbee et al., 2006]. This instance requires appropriate model algorithms not only to capture this mechanism, but also the critical timing (or, in this case, alluvial bulking volume) of its transformation.

Chapter 3

SNOW AVALANCHES

3.1 Modelling approach

Introduction

Since the 1970's, different avalanche forecasting models have been developed and used by various snow and avalanche research centres. Statistical methods using discriminant analysis and nearest neighbours seem to be the most popular approaches [Bois et al., 1975; Buser et al., 1987] although they have generally no explicit treatment of the physical snow processing. Operational systems based on the nearest neighbours methods are presently used by the avalanche forecasters in several countries but their results are highly dependant of the available archive fields and often the rare situations are badly reconstructed. Their most common limitation comes from the facts that the criteria for searching analogues situations use generally meteorological data rather than the internal state of the snowpack (stratigraphy and physical parameters of the different snow layers). The discriminant analysis method is more difficult to interpret by the local forecaster (less "sensible" approach). The discriminating capacity of the used function must be well studied for getting the best skill score in a stable way during all the utilisation period. Generally speaking, statistical approaches are efficient tools but their simplicity needs careful tunings and long calibration series. These methods are thus more suited for the forecasting of natural fresh snow avalanche but their results are limited in the case of slab avalanches triggered by skiers. As mentioned by Bader and Salm [1990] and Schweizer [1993], they cannot identify the presence of weak layers which are of prime importance for the release of slab avalanches. Even if an information on the vertical structure of the snowpack were available at a given time (typically once a week from a snow pit), such models would not have the possibility to make continuous and realistic time-evolution of the characteristics of the different snow layers. These models use local measurements as a main source of input data and thus have difficulties to take into account the variability of the snow pack stability due to elevation and slope aspects.

	Since the 1970's numerical models have been developed to simulate snow cover processes [Anderson, 1976; Colbeck, 1973; Obled and Rossé, 1975; Navarre, 1975]. These physically-based models simulate the evolution of the snow cover as a function of the weather conditions. They include a representation of the principal phenomena affecting the energy and mass balance of the snow pack. More recently, a new generation of these one-dimensional models has added more physical processes in the snow pack or at the snow atmosphere interface. These include snow metamorphism and absorption of solar radiation. These processes can be modelled in various ways. SNOTHERM model [Jordan, 1991] calculates crystal growth rate from the thermodynamics while CROCUS model [Brun et al., 1989 and 1992] calculates the evolution of both crystal size and shape with a possible connection to the international snow crystal classification [Colbeck et al., 1990]. A first attempt at using these numerical snow models for avalanche forecasting was made in France in 1988. It was based on a preliminary version of the CROCUS snow model [Brun et al., 1989]. This model required manual input of the relevant observed or forecasted meteorological variables necessary to calculate the evolution of the snow cover at given locations by the forecasters. This requirement limited the number of possible simulations to a few locations, which was not enough to calculate the evolution of snow cover at various elevations and for different slope aspects. In order to be able to run over numerous massifs and locations, it was decided to develop a special spatialisation model, SAFRAN, in order to automatically determine at hourly time step all the needed meteorological parameters at locations where no observation is available. SNOWPACK [Bartelt et al., 2002; Lehning et al., 2002a et b] is another successful modelling approach at SLF (Davos). It includes a very sophisticated modelling of the different heat and mass transfers between layers so as a detailed description of the snow microstructure and its properties. Generally SNOWPACK is running in operational mode for SLF at locations where automatic observations are available and is coupled to these data. Another avalanche forecasting method is based on expert systems, a popular approach in the 1980's decade. The initial objective of such models was to reproduce expert human reasoning in a particular field [Giraud et al., 1986]. Most systems use production rules organised in bases; some examples of these rules-bases can be found in Lafeuille et al. [1987]. Recently, hybrid expert systems have been developed by coupling expert systems with statistical models [Bolognesi et al., 1994, Schweizer and Föhn, 1994a, Weir and Mc Clung, 1994] or with neural networks [Schweizer et al., 1994b].
	3.2 Numerical Simulation Model
The SAFRAN/CROCUS/MEPRA chain (SCM)	Progress in snow research and more powerful computer facilities have made it possible to simulate the main features of the snowpack and the corresponding avalanche activity. Based on three individual models (SAFRAN, CROCUS, MEPRA) CEN has developed

	an automatic system, hereafter called SCM or "chain" [Durand et al. 1999]. The only inputs of this chain are daily meteorological observations, outputs of numerical meteorological models and precipitation climatologies. No snowpack information is entered into the system. The main assumption of this system lies in the spatial homogeneity of the massifs involved (especially for precipitation) which implies a corresponding working scale and excludes representing all the local effects such as those due to accumulation and erosion by the wind. As outputs, the chain simulates an average snow mantle, described by its stratigraphy, on different elevations and aspects of 23 Alpine massifs, 15 over the Pyrenees (surface area of about 500 km^2) and 2 in Corsica and the corresponding avalanche risks. Since the winter of 1992-93, this set of models has been used operationally by French Alps avalanche forecasters and since 1995-96 in the Pyrenees. At the same time it has been developed improved and validated by both contact with the different users and by comparison with different sets of human observations. The SCM chain starts at the first of August without any snow cover and runs all year long without any re-initialization. The snowcover is so only due to the hourly meteorological forcing provided by Safran for its creation, evolution and vanishing. The SCM chain is also at the root of different research and applicative works in mountainous hydrology [Braun et al., 1994], clayey landslides [Durand et al., 2006], or on the sensibility of the snow cover to a climate change [Martin et al., 1994]. All these studies have contributed greatly to its development.
SAFRAN	Before simulating snow cover, it is first necessary to calculate these prevailing meteorological conditions for the region considered with its different elevations and slope aspects. As we do not get observed data for each elevation or each aspect, we therefore developed a meteorological analysis model, called SAFRAN [Durand et al., 1993], to compute the relevant meteorological variables from all the meteorological information available in and around the region considered. The outputs of SAFRAN are then used by the snow model CROCUS to calculate the corresponding evolution of the snowpack. Due to the density of the "nivo-meteo" observation network in the French Alps and Pyrenees and also to the spatial definition of the meteorological forecast models, we decided to consider regions of about 500 km^2, called massifs, and to run the models on elevation from 600 to 3600 m a.s.l separated by 300 m steps, on the aspects N, E, SE, S, SW and W with slope angles of 20° and 40°. Over these areas SAFRAN performs a spatialization (we can also say "analysis") of the observed weather data available (automatic network, snow weather network, atmospheric upper-level sounding) over the considered elevations and aspect of the different massifs. Automatically (one says "objective" as opposed to "manual"), SAFRAN combines the observed information with preliminary estimations. These fields (generally called "guesses") are computed from the results of the "ARPEGE" French meteorological model (Courtier et al., 1991) or from the ECMWF analyses through appropriate downscaling operators. The interpolation method used ("optimal interpolation", OI) and the operators used have been described in detail in Durand et al. [1993]. As outputs, SAFRAN provides the main relevant atmospheric parameters affecting snowpack evolution: air temperature, wind speed, air humidity, cloud cover, snow and

rain precipitation, long wave radiation, direct and scattered solar radiation. The analysis provides, all through the year, series of relevant meteorological parameters over areas where no human or automatic observation is available.

Routine tests are daily performed by comparing the SAFRAN analyses with meteorological observations collected at two well instrumented automatic sites located respectively at 1320 m a.s.l (Col de Porte, Chartreuse massif) and 2700 m a.s.l (Col du Lac Blanc, Gdes-Rousses massif). At both sites, air temperature, air humidity, wind velocity, incoming long wave and short wave radiation and snow or rain precipitation were measured. Naturally, these data are not used by SAFRAN to perform its analyses and thus were actually designed to qualify SAFRAN results.

A forecast version of SAFRAN is also used by Durand et al. [1998]. As no observation can be used, the provided outputs are mainly based on the quality of the previously mentioned downscaling operators. About the forecasted precipitation fields, the analysis of a past date through a nearest neighbours research method is used together with the daily downscaled field. For an example of results see ***Figure 25*** and ***Figure 26***.

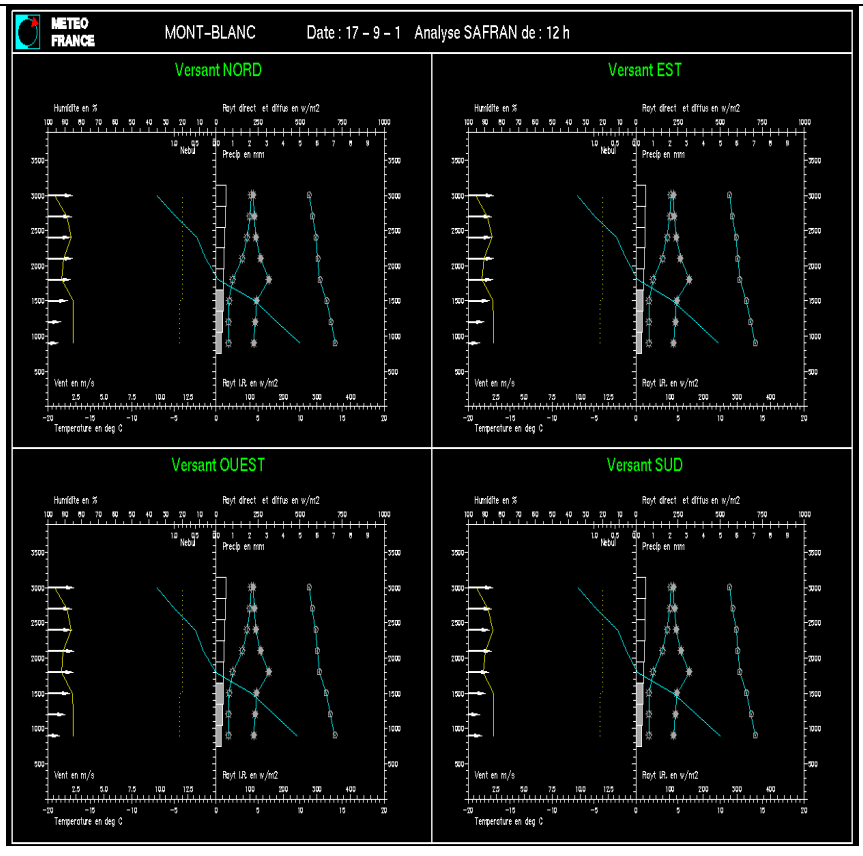

Figure 25 Example of the results obtained on four aspect of the Mont-Blanc massif on 17th September 2001 at 12 UTC in analysis mode. The surface humidity is drawn on the left as the yellow line (top left scale in %), with the arrows indicating the wind speed (bottom left scale in m/s). In the center the temperature is in full blue line (bottom scale in °C) and cloudiness in dotted line (top scale in [0,1]). The precipitation is to the right of the central axis (top right scale, grey squares means rain). All the radiation values are plotted on the right (direct="✧ "sun; scattered=mixed "✸" dotted/black sun; atmospheric=mixed "O" dotted/white circle) with their scales on top and bottom of this side in W/m^2)

Figure 26 Example of the 1 day range operational forecast mode of SAFRAN concerning the 24hr precipitation at 1800m a.s.l over 24 alpine massif on flat aspect for the 11th January 1999. The left picture shows the verification analysis (performed in real time), the middle picture exhibits the final operational 24hr precipitation forecast (issued the 10th January) as seen by the forecaster. This forecast is based on the result of the meteorological model ARPEGE (right side top) and a nearest neighbours research (here the 14th March 1996, right side bottom).	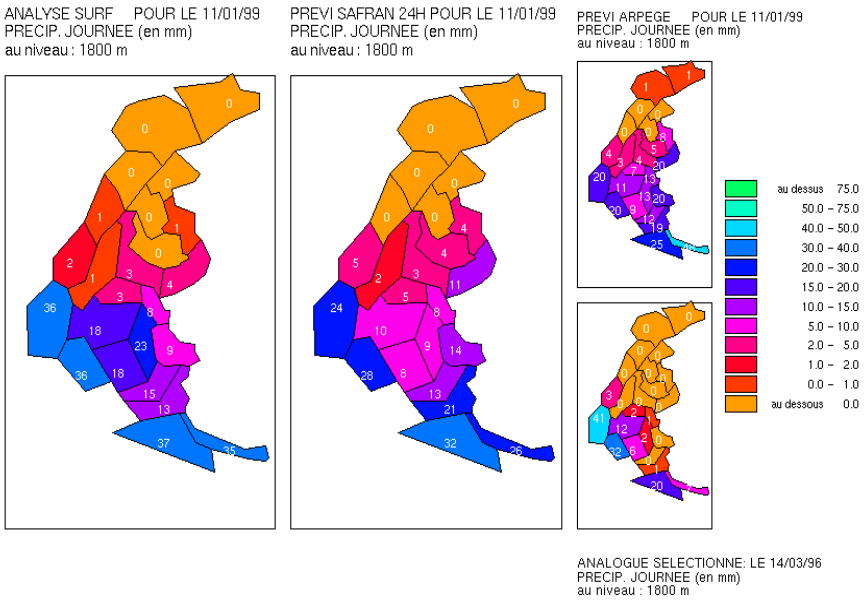
CROCUS	***CROCUS*** [Brun et al., 1989 and 1992**]** is a numerical snow model calculating the energy and mass evolution of snow cover. It uses the meteorological data calculated by the SAFRAN model and simulates the evolution of temperature, density, liquid water content and layering of the snow pack. The originality of this snow model comes from its ability to simulate snow metamorphism in near surface and buried layers and to represent each snow type under a comprehensible form. Snow albedo and extinction coefficient depend on the wavelength and the surface snow type, size and age. The model estimates the internal state of the snow pack: temperature, liquid water content, density and snow types. For calculating the different variables, the snow pack is divided into layers (between 1 and 50) which are parallel to the surface slope. The following phenomena are taken into account by the model: the energy exchanges inside the snow pack and at the snow-soil and snow-atmosphere interfaces, the absorption of solar radiation with depth, the phase changes between solid and liquid water, the water transmission through the snow pack, the mass exchanges due to precipitation and water runoff, the compaction and the metamorphism of the snow. Every year, the model considers that each simulated slope is snow free on August the first. The simulated snow pack evolves day by day from the first snow fall until the complete melting without re-initialisation. Recent further developments of this model include the initial determination of the parameters describing fresh snow crystal (dendricity and sphericity) depending on the SAFRAN wind speed, in order to begin to take into account the destructive effect of the wind during a snowfall. The model results have been compared (***Figure 27*** and ***Figure 28***) with observations at various scales: locally in the PILPS 2d intercomparison phase [Schlosser and others, 2000] and at Col de Porte [Brun and others, 1992], regionally in the French Alps [Martin and others, 1994] and for the entire northern hemisphere

	[Brun and others, 1997; Etchevers and others, 1999]. Crocus is an important research tool which is used together with other surface models for hydrology, environment, snow on roads. It also allows different studies on the impact on the snowpack and related risks of different climate change scenario. In the framework of avalanche hazard forecasting, Crocus has been used operationally since 1992 (JO-Albertville) in its earlier version and this use is still continuing.

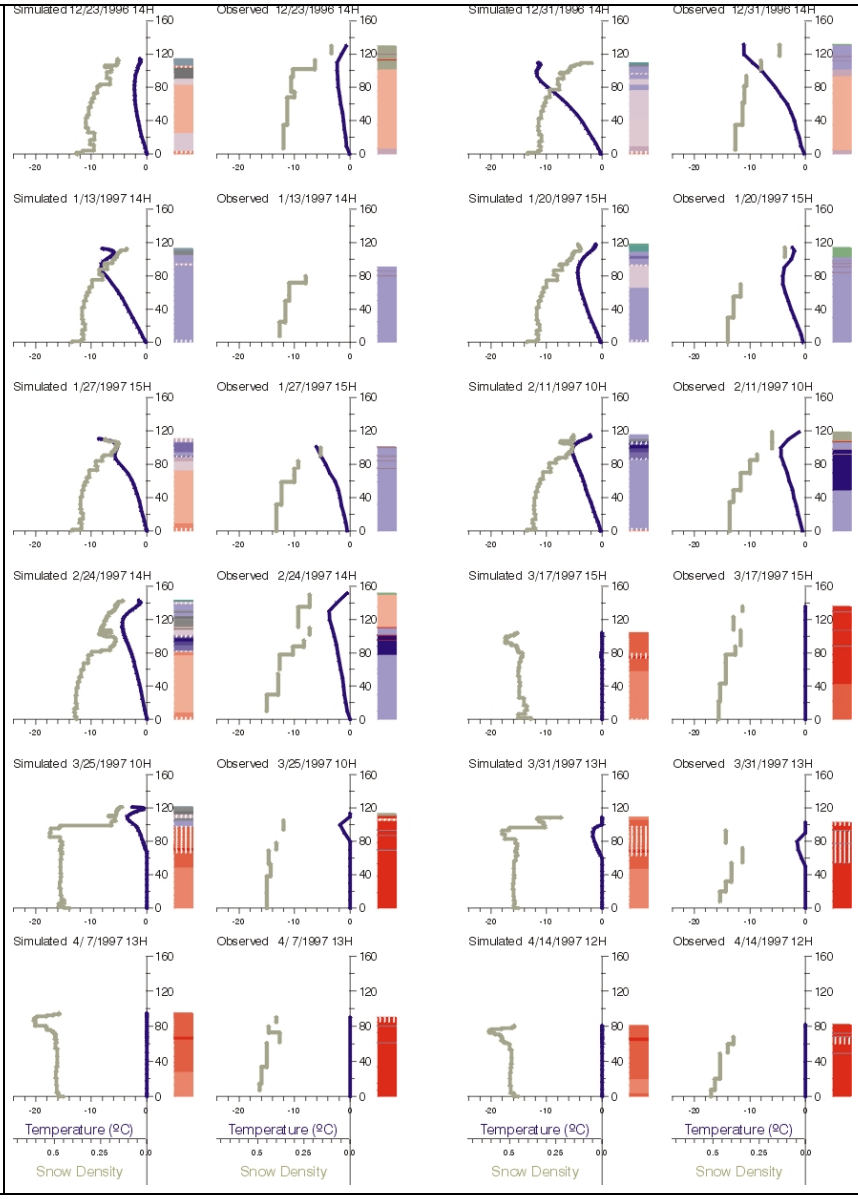

Figure 27 Comparisons between observed and numerically simulated snowpack structures during the 1996-97 winter at the ski resort of "La Plagne" (Vanoise massif) on the snow pit location of "Montchavin" (2100m, NE). The different panels illustrate the weekly observed snow pits and the corresponding computed profile. The vertical axis (in cm) represents the snow depth and the blue and green curves respectively temperature and density profiles (with two different scales on the horizontal axis in °C and %V). On the right side of each profile , the stratigraphic profile is illustrated by the color code presented in next figure while vertical hachures show crusts.

Figure 28 Color code used for the snow crystals representation. This figure shows the connection with the international classification (Colbeck et al., 1990). Briefly, the fresh snow is represented by green colors, faceted crystals by a blue coloration and rounded crystals by red. As explained in Brun et al. (1992), fresh snow is described in terms of dendricity and sphericity and the more transformed crystals are defined by their size and sphericity.	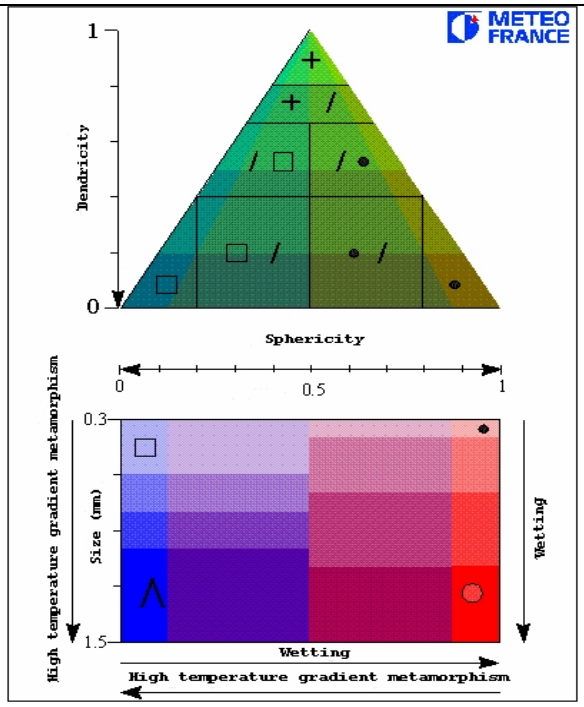
MEPRA	***MEPRA*** [Giraud, 1992] is an expert system for avalanche risk forecasting. This system deduces from the CROCUS snow pack simulations additional mechanical characteristics (shear strength, ram resistance) through statistical relationships. These relations have been calculated from a lot of in-situ snow measurement campaigns . After classifying the generated ram and stratigraphic profile, this model predicts the "natural" mechanical stability of the snow pack (i.e. the risk of spontaneous avalanches without human overloading). In a first step, the classical stability index is calculated for each layer of each simulated snow pack [Föhn, 1987]: $$S = \frac{C}{\tau_n} = \frac{shear strength}{snow shear stress}$$ Depending on the value and the temporal evolution of this index, a "natural" avalanche risk of spontaneous avalanches is classified into one of the 6 levels (very low, low, moderate increasing, moderate decreasing, high and very high) completed with a classification of different avalanche types (fresh dry, fresh wet, fresh mixed, surface slab, surface wet, bottom wet). In case of wet snow, the calculated index is adjusted by a diagnostic based on the increasing depth of the wetted layer. In a second step, the expert system interprets the snow pack structure to detect the risk of release of a dry slab avalanche by a skier. It is considered that slab avalanches start with a shear fracture or a collapse in a weak layer or interface [Schweizer, 1993, Jamieson and Johnston, 1993]. To achieve that, it looks first for a snow slab in the superficial layers of the snow pack according to different criteria as the density and the grain size and types. After detecting a slab, it looks for the presence of a weak layer beneath the slab by calculating a stability index integrating human triggering, grain size and shear strength [Föhn, 1987, Giraud, 1995], based on a simple Rankine equilibrium:

$$S' = \frac{C}{\tau_n + \tau_s} = \frac{shear\ \ strength}{snow\ \ shear\ \ \ stress + skier\ \ shear\ \ \ stress}$$

Depending on the S' index value, an "accidental" avalanche risk is then deduced on a 4 levels scale for each point (very low, low, moderate, high). Some examples, so as MEPRA risks evaluation can be seen in the following figures.

These avalanche diagnostics have the same spatial representativity as their input data (i.e. the massif) and do not take into account the accumulation or erosion of snow by the wind. MEPRA does not calculate a risk level integrated spatially on the whole massif. It provides the forecaster with "natural" or "accidental" risks at the different elevations and aspects. It helps him in pointing out what kind of slopes are more likely for the natural or accidental release of avalanche.

For a comparison between observed and calculated snowpack see ***Figure 29*** and ***Figure 30***. In ***Figure 31*** and ***Figure 32*** there are a symbolic representation of MEPRA natural avalanche types and risks.

Figure 29 Observed snowpack profile during the avalanche case of "Roc du Fer" on February 16th, 1996 showing the profiles of temperature (°C) and ram hardness (kgf) at different depths "H". According to Colbeck et al. (1990) the columns F1 and F2 indicate the two main grain shapes. The density "Dens" of each layer is in kg/m^3, and the grain size is described by its diameter "Diam" in tenth of mm. The column "Wet" at 1 indicates a dry profile whereas the different manual hardness "Hard" is expressed on a 5 level scale. A manual estimation of the shear strength (in kg/dm^2) is given in the column "Shear".	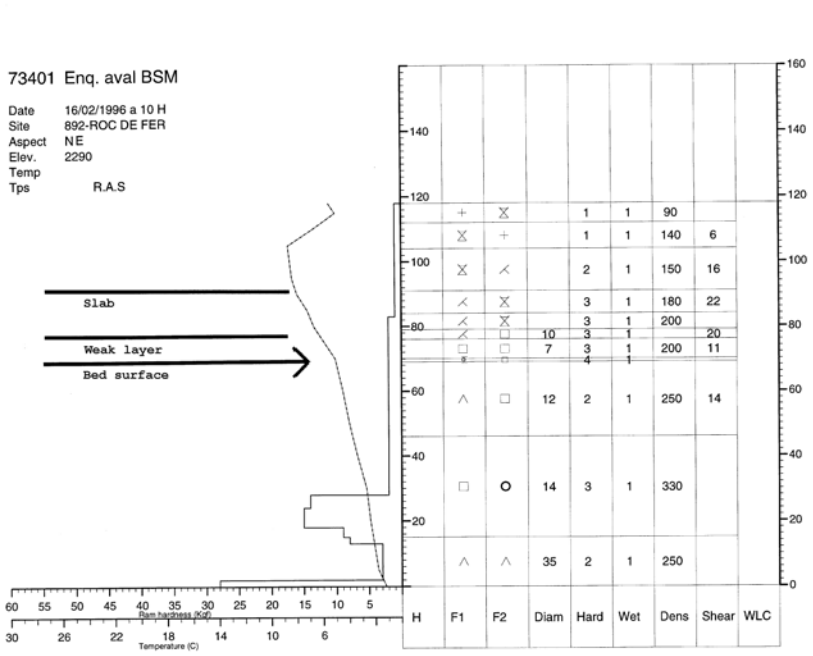
Figure 30 Simulated SCM snowpack profile at a computing location corresponding to the site of the avalanche case of "Roc du Fer" on February 16th, 1996 (Vanoise massif, East, 2100m, 40 deg. Slope) and showing the same two profiles as in the previous figure. Nevertheless the two main grain shapes are presented in a column named "grain", the diameter of the grain size (column "diam") is in mm and the density "dens" in 10^3 kg/m^3. The "S" stability index is printed in the last column.	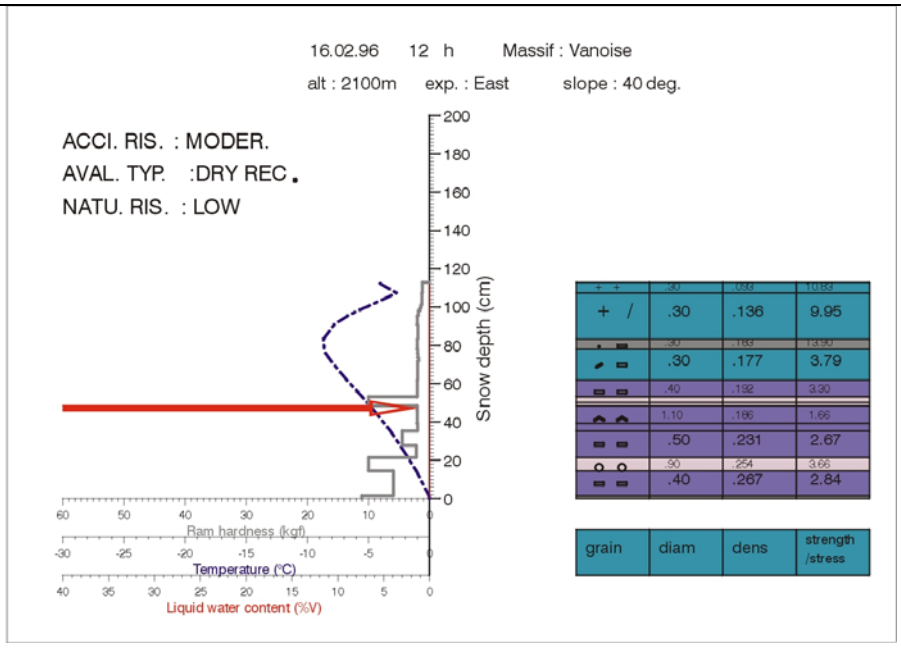

Figure 31 Symbolic representation (elevation and aspects) of MEPRA natural avalanche risks and types on the "Gdes-Rousses" massif for one slope (40 deg) in a typical winter situation (1995/01/23 at 12 UTC) as seen on the user screen.	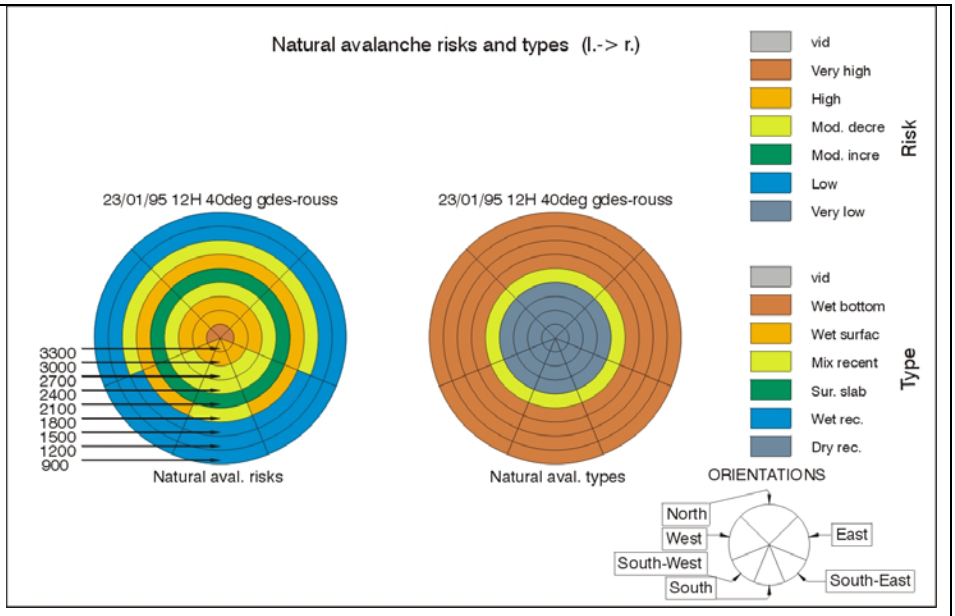
Figure 32 Symbolic representation (elevation and aspects) of MEPRA natural avalanche risks and types on the "Belledonne" massif for one slope (40 deg) in a typical spring situation (1994/03/09 at 12 UTC) as seen on the user screen.	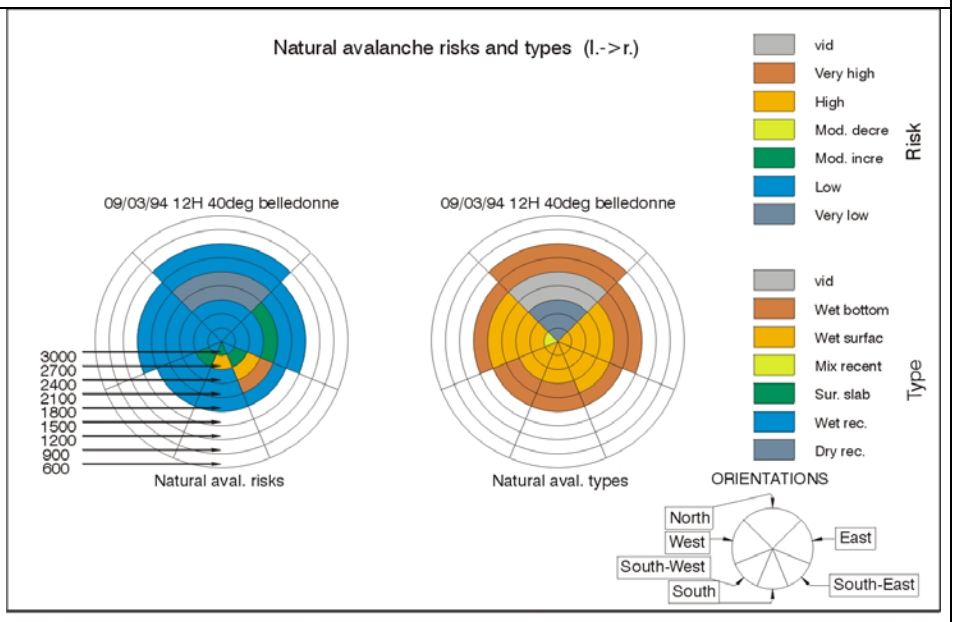
SNOWPACK	This numerical snowpack model has been developed and is routinely used by SLF. It is a one-dimensional physical model which is operationally employed on a day-to-day basis by avalanche warners to predict snowpack settlement, layering, surface energy exchange and mass balance. Meteorological data obtained from automatic weather stations positioned near avalanche starting zones is used as model input. The one-dimensional equations governing the heat transfer, water transport, vapour diffusion and mechanical deformation of a phase changing snowpack are used. New snow, wind drift and snow ablation are treated as special mass boundary conditions. Snow is modelled as a three-component (ice, water, air) porous material capable of undergoing large irreversible viscous deformations. Phase changes between the components are simulated. Snow layers are defined not only in terms of height and density, but also microstructure. That is, by the size, shape and bonding of the grains composing the ice lattice. The governing differential equations are solved using a fully implicit Lagrangian Gauss–Seidel finite-element method. The overall mass balance evaluation shows that the model accurately predicts the build-up and ablation of the seasonal

	alpine snowcover. The snow cover model SNOWPACK includes a detailed model of snow microstructure and metamorphism. In SNOWPACK, the complex texture of snow is described using the four primary microstructure parameters: grain size, bond size, dendricity and sphericity. For each parameter, rate equations are developed that predict the development in time as a function of the environmental conditions (***Figure 33*** and ***Figure 34***). The rate equations are based on theoretical considerations such as mixture theory and on empirical relations. With a classification scheme, the conventional snow grain types are predicted on the basis of those parameters. The approach to link the bulk constitutive properties, viscosity and thermal conductivity to microstructure parameters is novel to the field of snow cover modeling and is based on existing knowledge on microstructure-based viscosity and thermal conductivity. This includes the strong coupling between physical processes in snow: The bond size, which changes not only through metamorphic processes but also through the process of pressure sintering (included in our viscosity formulation), is at the same time the single most important parameter for snow viscosity and thermal conductivity. Laboratory results are used to illustrate the performance of all these formulations. The development of the seasonal snowcover is entirely driven by atmospheric forcing. SNOWPACK uses measured snow depths to determine snow precipitation rates via the calculated settling rates. This requires a rigid data control algorithm. A new statistical model is used to estimate fresh snow density as a function of the measured atmospheric conditions. A statistical model is also derived for the snow albedo, which is necessary to determine the absorbed radiation. The surface sensible and latent heat flux parameterizations are derived from Monin–Obukhov similarity and include a formulation for wind pumping. The formulations will also adapt to drifting snow conditions. This new suggestion is consistent with the observation of different roughness lengths for scalars and momentum over snow. An accurate formulation, especially for the latent heat exchange, is crucial because latent heat exchange determines the formation of surface hoar, a very important weak layer. The effect of wind pumping on the thermal conductivity in the uppermost snow layers are also taken into account. The surface energy and mass exchange formulations are evaluated by looking at the formation of the important thin layers surface hoar and melt–freeze crusts in SNOWPACK. Those layers are well simulated. In addition, the complete snow profile development is modeled successfully for the parameters grain type, temperature, density, grain size and liquid water content. An overall score between 0 and 1isused to describe the profile agreement with observations and an average score of over 0.8 is reached.

Figure 33Time evolution (over winter 98-99 on x axis) of the snow stratigraphical profile in a reference station with total sow depth on y axis. Grain types area referenced with the left-hand colour code.

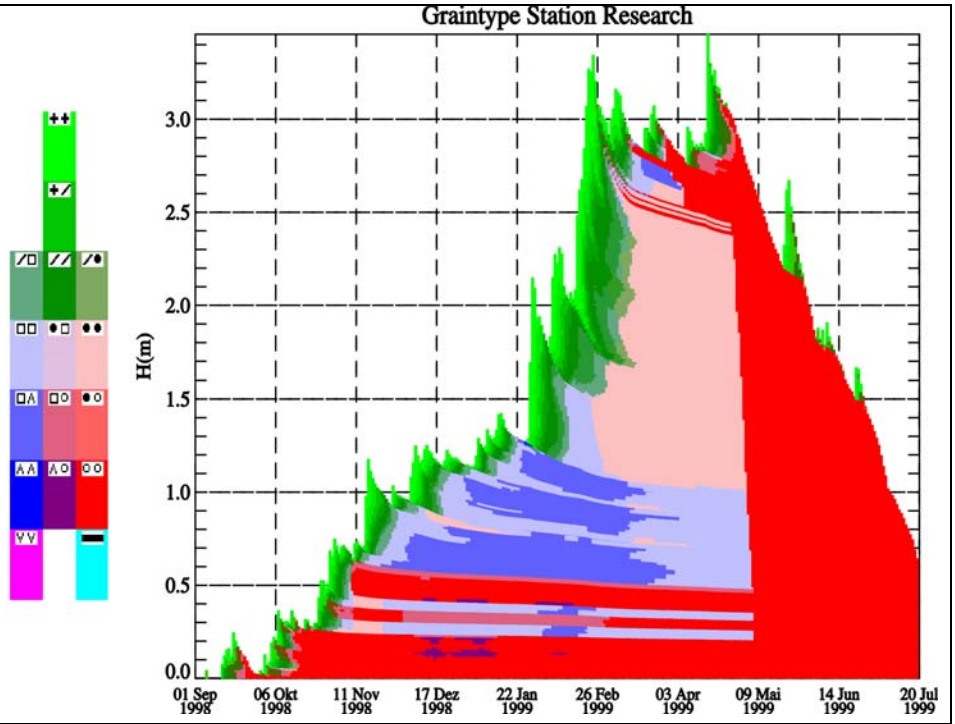

An interesting development in SNOWPACK concerns blowing snow and its ability to produce an automatic snow drift index.

Figure 34 Time evolution of SNOWPACK snow drift index.

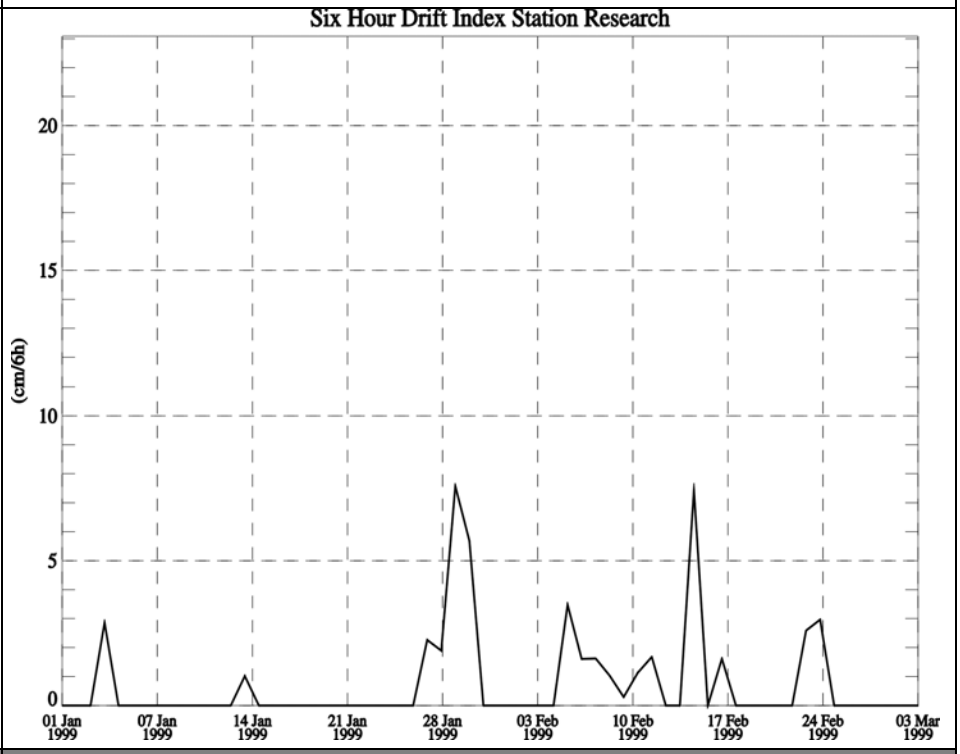

3.3 Empirical modeling

Since the 1970's, different avalanche forecasting models have been developed and used by various snow and avalanche research centres. Statistical methods using discriminant analysis and nearest neighbours seem to be the most popular approaches [Bois et al., 1975; Buser et al., 1987] although they have generally no explicit treatment of the physical snow processing. Operational systems based on the nearest neighbours

	methods are presently used by the avalanche forecasters in several countries but their results are highly dependant of the available archive fields and often the rare situations are badly reconstructed. Their most common limitation comes from the facts that the criteria for searching analogues situations use generally meteorological data rather than the internal state of the snowpack (stratigraphy and physical parameters of the different snow layers). The discriminant analysis method is more difficult to interpret by the local forecaster (less "sensible" approach). The discriminating capacity of the used function must be well studied for getting the best skill score in a stable way during all the utilisation period. Generally speaking, statistical approaches are efficient tools but their simplicity needs careful tunings and long calibration series. These methods are thus more suited for the forecasting of natural fresh snow avalanche but their results are limited in the case of slab avalanches triggered by skiers. As mentioned by Bader and Salm [1990] and Schweizer [1993], they cannot identify the presence of weak layers which are of prime importance for the release of slab avalanches. Even if an information on the vertical structure of the snowpack were available at a given time (typically once a week from a snow pit), such models would not have the possibility to make continuous and realistic time-evolution of the characteristics of the different snow layers. These models use local measurements as a main source of input data and thus have difficulties to take into account the variability of the snow pack stability due to elevation and slope aspects.
NXD/NXD2000/NXD-REG/NXD-VG (from Gassner et al., 2002)	NXD is numerical tool for local avalanche forecasting by the method of the nearest neighbors (past situations which are close of the current situation) initiated at SLF-Davos [Büser et al., 1987]. NXD-Lawinen contains a weather, snow and avalanche database. The program searches the database in order to find meteorologically similar days. The avalanche events of those days help estimate the current avalanche danger. The program gets better with each use because the search data is also inputted into the database. The set of variables used is primarily the one Obled and Good [1980] selected for their own test at the snow sport area Parsenn, Davos, Switzerland, because they are crucially connected with avalanche occurrence. However, not all of these variables are measured at every site. New variables are so used as decribed by Obled and Good [1980]. Variables from previous days (so-called “predays”) are used to calculate “elaborate” variables. They constitute an attempt to introduce physical knowledge about the assumed underlying phenomena and the experience of the forecaster. Changing from raw data to evaluated variables should involve a substantial increase of information. Weather and avalanche data are displayed for the nearest-neighbors, helping the human forecaster to anticipate the avalanche problems they may encounter that day. This provides an excellent avalanche forecasting tool for ski areas or highway avalanche forecasting operations. New versions of this software have been developed [Gassner et al., 2002]. They are always based on the same method, but they are targeted to different scales. NXD2000

	(***Figure 35***) is used to forecast avalanches on a local scale. It is operated by avalanche forecasters responsible for snow safety at snow sport areas, villages or cross country roads. The area covered ranges from 10 km^2 up to 100 km^2 depending on the climatological homogeneity. It provides the forecaster with ten most similar days to a given situation. The observed avalanches of these days are an indication of the actual avalanche danger
Figure 35 Representation of the nearest neighbors in NXD2000. On the left part the ten nearest neighbors with some of their previous days are shown, on the right top their variables and on the right bottom the aspect altitude diagram of the observed avalanches	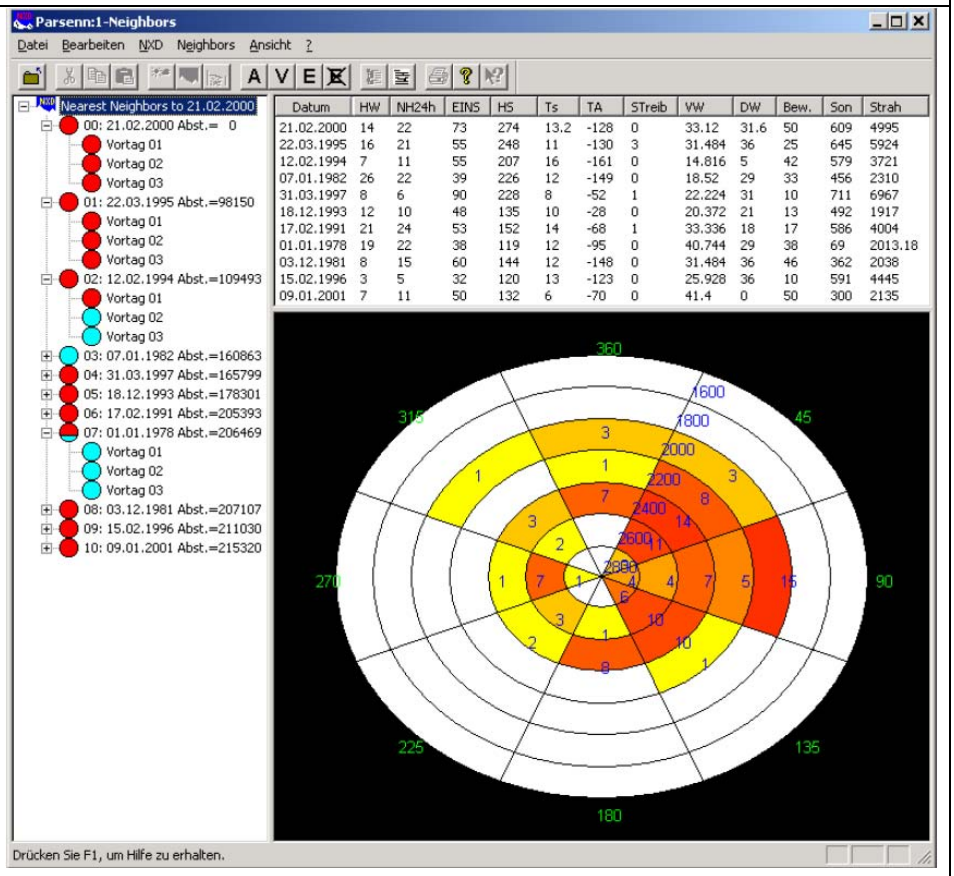
	NXD-REG is used operationally by the Swiss avalanche warning service for regional avalanche forecasting (***Figure 36***). The Nearest Neighbour approach is applied to the data sets of 60 observer stations. The results of each station are then compiled into a map of current and future avalanche hazard. Evaluation of the model by crossvalidation has shown that the model can reproduce the official SLF avalanche forecasts in about 52% of the days.

Figure 36 Result of NXD-REG for 19 February 2000

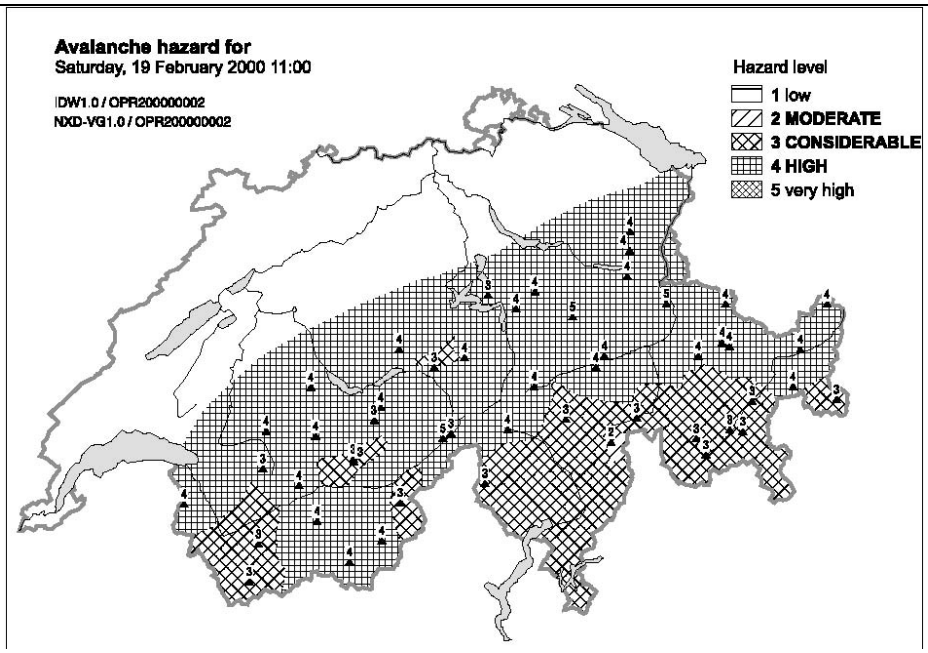

Because of the success of nearest neighbour models in local avalanche forecasting, the NXD model has also been adapted for regional avalanche forecasting and called NXD-VG. Swiss observational data are used operationally. Two elaborated parameters were added: the 3daysum of new snow and a 1day difference of air temperature. No further transformations are used. Model output is the estimated hazard level according to the European avalanche hazard scale. The hazard level is calculated by averaging results from the 10 nearest neighbours and applying decision boundaries. The distance is calculated using a Euclidean weighted distance metric. The weights have been estimated by the SLF avalanche warning service. The result of NXD-VG is given in table-form for each station: meteorologic and snow parameters, date of the 10 nearest neighbours, result of the distance calculation and the original avalanche bulletins are presented to the avalanche forecaster.

Globally, the main problems that restrict the use of the nearest neighbour method are :

- -Missing observations: For example, if there are no measurements on Sunday, no nearest neighbour search is possible until Wednesday, when fresh snow accumulated during the three pre-days is used as an elaborate variable.
- Missing or imprecise avalanche observations
- Sharp changes of variables within time period of measurement
- Homogeneity of data and observations: Changes in the location or the method of weather and snow measurements might interrupt the time series or lead to data inconsistencies to which the model is sensitive.
- Definition of an avalanche day: One of the main questions is: What makes an avalanche day?
- Avalanche control work performed on the previous days: During snowfall periods the avalanche danger increases with the amount of fresh snow. Launching avalanches reduces the danger that cross country roads or snow sport areas can be open.

Nearest neighbour method applied in Norway (from NGI report)	The forecasting method of nearest neighbour (Figure 37) was first introduced in Switzerland by Buser [1983]. In Norway, NGI started developing a similar system based on standard meteorological data from weather stations operated by the Norwegian Meteorological Institute. The observations are taken three times per day, 07, 13 and 19 local time, and the parameters of interest are temperature, wind speed, wind direction, snow depth, precipitation the last 24 hours, 72 hours and 120 hours. There are not performed radiation measurements on standard observation stations, the cloud cover is observed manually. Recording of avalanches hitting roads started in the middle of the seventies, and in some districts the records are quite good. In short, the nearest neighbour system can be expressed wit the following equation: Difference $\Delta J2 = \Sigma\, ki\, (xi - xiJ)2$ With used variables: temperature, precipitation one day, precipitation three days, precipitation five days, wind direction, wind speed, snow depth. This might be illustrated by the sketch below where R is the distance between the actual and former observation:
Figure 37 Graphical presentation of the nearest neighbour method	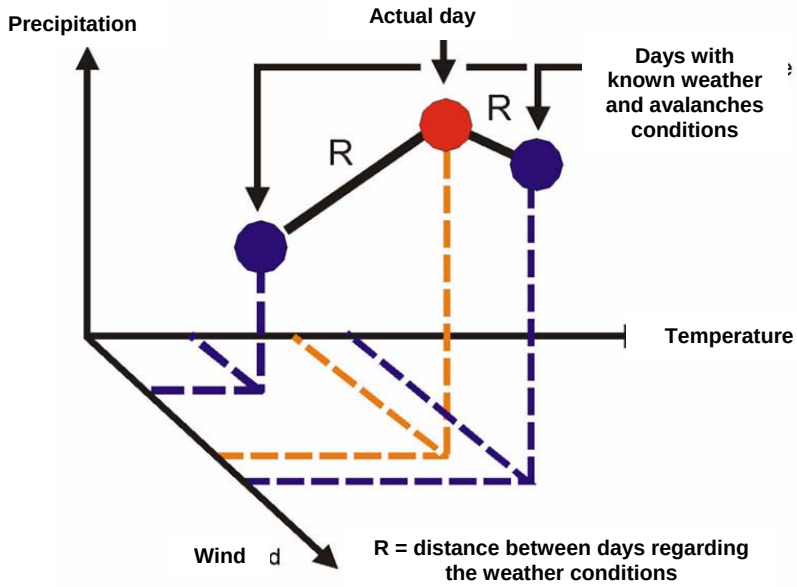 **Graphical presentation of the nearest neighbour method**
	Development of the system started in 1989, and as a tool for calculation, Paradox database engine was used. This work was sponsored by the Road department, and data from the NGI research station at Strynefjell was used as test dataset. Thereafter, a dataset for the Møre district of Western Norway used the system operative with manual observations of the meteorological parameters. However, the manual input of data into the system did not work, when the avalanche hazard was low, the interest for the model was low, and when the avalanche hazard was high, the maintenance crew were busy with removing snow. Therefore it seemed necessary to install automatic weather observation equipments. In addition, the development of new operating systems on the PCs, forced it necessary to reprogram the system. The program is now written in Visual basic using Microsoft Access for the database.

	In addition to Møre and Strynefjell, the system was introduced in Odda district in Southwestern Norway, later also in Hyen between Odda and Møre. For the winter season, the system is used in the Tromsø district in Northern Norway. The areas where the system is in use, are presented on the ***Figure 38***.
Figure 38 Map showing the location of nearest neighbour application sites	
	A professional programming company working for the Public Roads has worked with the interface between the user and the program. The program is now easy and logistic to use, and the data for avalanches are found on the main server for the Public Roads (***Figure 39***). The weather data is mostly available via FTP-servers on Internet or from local weather stations close to Public Road offices. There are different prints from the calculations, the best hits are printed first and you might have as many hits as necessary. Below is a screen shot giving data and dates for the best hits. There are possibilities to change the weighting factors for the different parameters according to the snow situation. Usually one set of weighting factors are used for cold days with subzero conditions while an other set is used when there is a melting situation in the release area for the avalanche.

Figure 39 Screen shot from the software implementing the nearest neighbour method

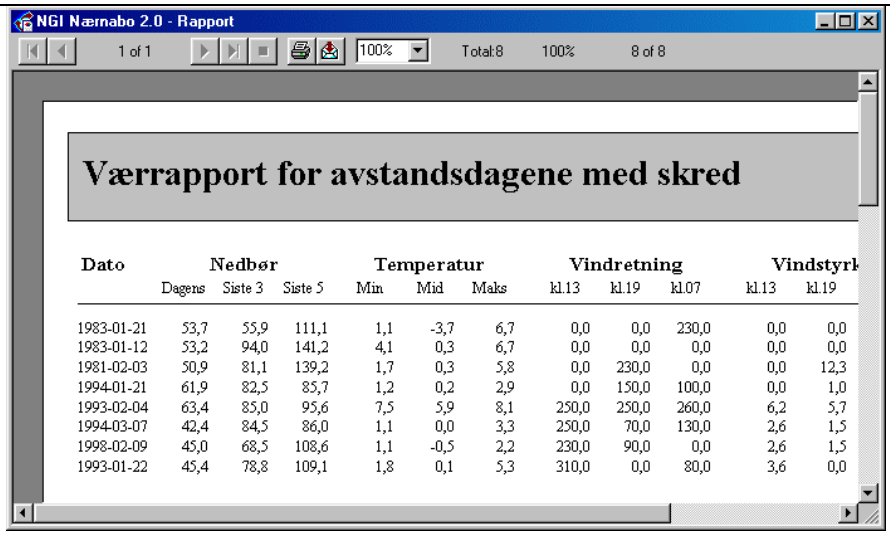

Dato	Nedbør			Temperatur			Vindretning			Vindstyrk	
	Dagens	Siste 3	Siste 5	Min	Mid	Maks	kl.13	kl.19	kl.07	kl.13	kl.19
1983-01-21	53,7	55,9	111,1	1,1	-3,7	6,7	0,0	0,0	230,0	0,0	0,0
1983-01-12	53,2	94,0	141,2	4,1	0,3	6,7	0,0	0,0	0,0	0,0	0,0
1981-02-03	50,9	81,1	139,2	1,7	0,3	5,8	0,0	230,0	0,0	0,0	12,3
1994-01-21	61,9	82,5	85,7	1,2	0,2	2,9	0,0	150,0	100,0	0,0	1,0
1993-02-04	63,4	85,0	95,6	7,5	5,9	8,1	250,0	250,0	260,0	6,2	5,7
1994-03-07	42,4	84,5	86,0	1,1	0,0	3,3	250,0	70,0	130,0	2,6	1,5
1998-02-09	45,0	68,5	108,6	1,1	-0,5	2,2	230,0	90,0	0,0	2,6	1,5
1993-01-22	45,4	78,8	109,1	1,8	0,1	5,3	310,0	0,0	80,0	3,6	0,0

Nearest neighbour method applied in France: ASTRAL/ANIS

Astral [Guyomarc'h et al., 1994, Mérindol et al., 2002] is a tool developed in order to help the avalanche forecaster at a local scale in a safety service of a ski-resort. In Astral, the selection is only made among the daily observed parameters. The daily observation comes mainly from the snow weather network made at 8h and 13h local time. In particular, daily information from snow-pits are not available. When the raw data are chosen, they are very often correlated ; it is more efficient to avoid variables which are too much correlated each other. Thus, the principal components analysis (PCA) is used to calculate linear independent variables and to minimize the lost of information in term of cumulated variance. In this new space, the principal components vectors space, each day is represented by a point with its new coordinates.

The used raw observed variables are:

- air temperature at 8h and 13h local time,
- snow temperature at the same times,
- daily water equivalent of the precipitations,
- daily recent snow amount,
- depth of snow mantle,
- sum on 3 days of the temperatures above 0°C threshold at 13h,
- sum of the water equivalent on two and three days,
- sum of the fresh snow on two and three days,
- penetration depth at 8h,
- wind velocity at 8h and 13h,
- avalanche code at 13h (D) and 8h (D+1).

Fifteen variables are so used for the characterization of the day and two (the avalanche code) as illustration parameters.

In ASTRAL, 10 principal components are retained from the 15 raw variables, which explains 95% of the cumulative variance. With about 600 days, the percentage explained by each principal component is stable as seen in ***Figure 40***. So for any new set up in a safety service, it is recommend to have a minimum of 4 winter seasons to avoid statistical instability.

Figure 40 Evolution of the variance in ASTRAL with the number of available	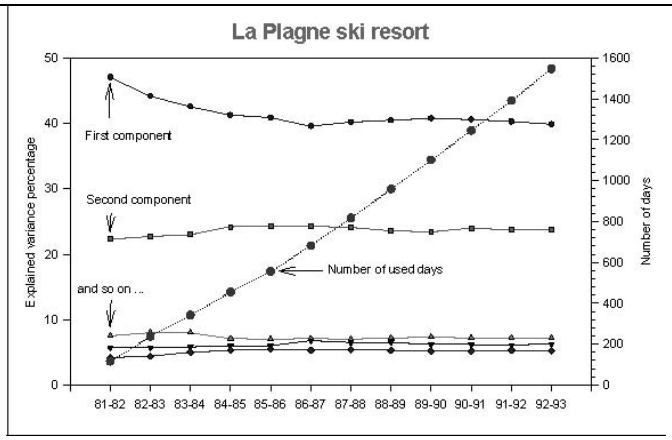
	All the past winter-days are projected in the PCA space and the principal component are calculated. In the PCA vector space, an Euclidean distance is used as a criteria of proximity and also the correlation coefficient. A geometric explanation of this second criterion is the cosine angle between the two vectors. This criterion is very interesting when a day is far away from the density centre of all days. The final result is the description of the ten neighbours of the selected day. For example see ***Figure 41*** and ***Figure 42***.

Figure 41 Astral results screen in Geliniv environment.

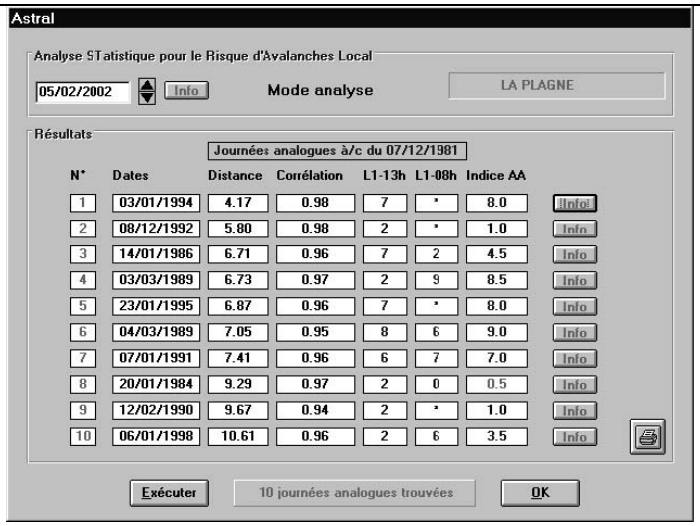

Figure 42 ASTRAL Raw variables for analysis day and the first analogous day

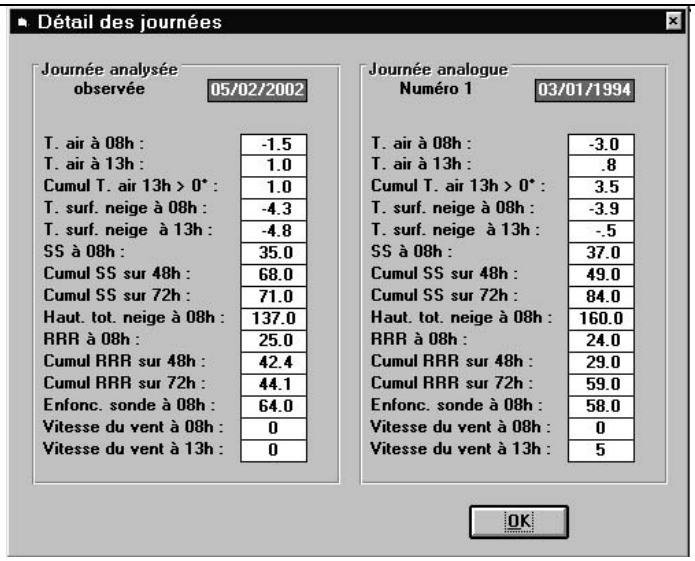

A forecasting possibility exists implicitly for the days after in inserting forecasted "observed" raw data in order to simulate other days with these "imaginary" data. This function is very appreciated by the local forecaster.

In order to improve the ASTRAL application, an additional information on the internal structure of the snowpack and on its spatial variability has been added in the framework of the ANIS application. But, as no daily snow-pits are routinely daily available, snow profiles and different other information issued from the SCM chain at different elevations and aspects are used. This application is presently in test at the La Plagne ski resort with improved results compared to the prior version.

Threshold values used in Norway (from NGI report)

A standard method to give avalanche hazard evaluation can be visualized with a matrix with the hazard scale versus the precipitation for a certain period, most commonly used is three day precipitation. In addition, a weighing due to wind in the period is performed [de Quervain, 1972] as shown on the ***Figure 43***. A practical example from an avalanche path at Framruste, Skjåk, is presented in the next figure

Figure 43 Avalanche hazard according to wind and three days precipitation

Wind(m/s) Precipitation 3 last days(mm)	<6	6 - 11	11 - 16	17 – 21	>21
0 – 10	1	2	3	4	5
10 – 30	2	3	4	5	5
30 – 60	3	4	5	5	5
60 – 80	4	5	5	5	5
>80	5	5	5	5	5

In 1986, NGI presented a probabilistic approach in the avalanche hazard warning [Bakkehøi, 1987] where for a certain avalanche path, the accumulated precipitation before a release were sorted and plotted on cumulative probability distribution paper, see ***Figure 44***.

Figure 44 Cumulative probability distribution of three day precipitation at Raffelsteinfonn causing avalanche occurrence

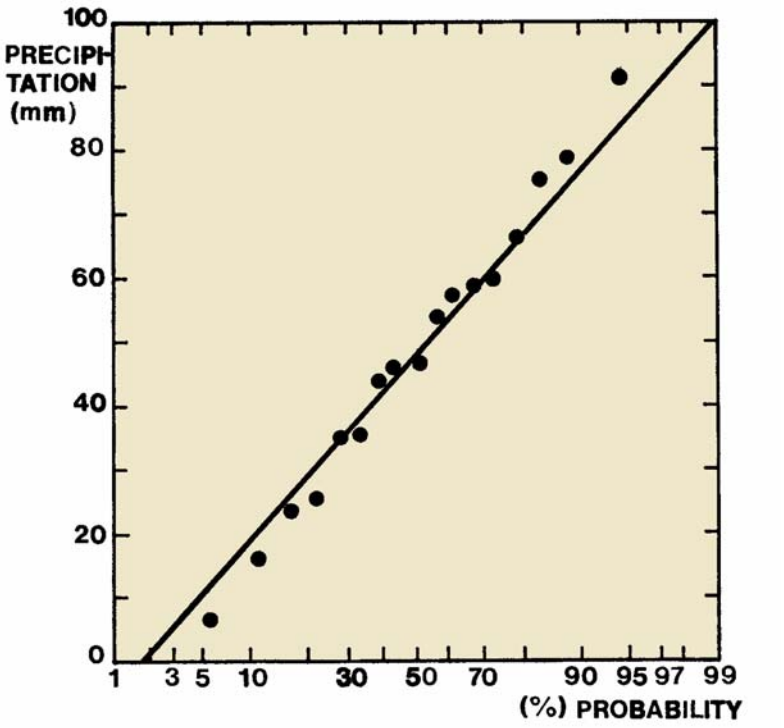

The avalanches used in the investigation, were dry snow avalanches released in situations accompanied by wind in the release zone. The different amounts of precipitation ahead the release are therefore mostly functions of snow fall intensity, different wind speed and the snow stratigraphy in the release area. There are achieved different probabilistic curves for different avalanche paths in the same region, this is due to different steepness in the starting zone and different aspects which give another building of the snow pack. Curves from five different avalanche tracks are presented in the ***Figure 45*** and the avalanche profiles are presented in ***Figure 46*** afterwards. The gentle slope Lifonn needs more precipitation before it starts sliding than the steeper ones, a 20% probability of release for the Lifonn avalanche needs 47 mm of precipitation while for the same probability Raffelsteinfonn avalanche which is much steeper in the release area, only needs 27 mm of precipitation. This method of avalanche hazard warning is used in the warning system for highway 15 passing Strynefjell.

Figure 45 Distribution of curves for five avalanche paths	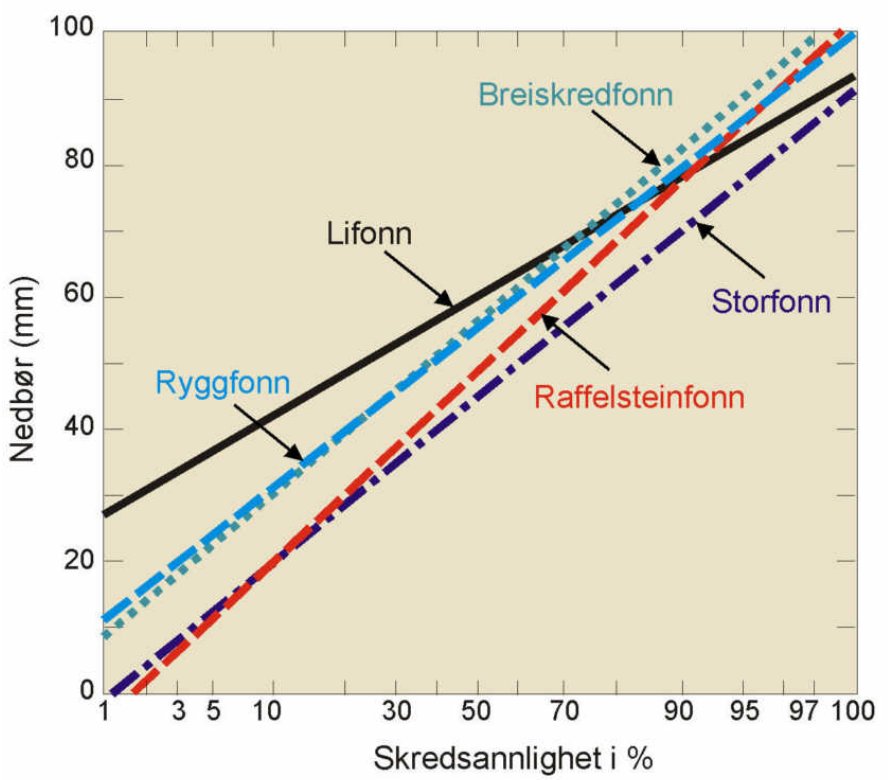
Figure 46 Terrain profiles for the five investigated avalanche paths in Grasdalen, Stryn	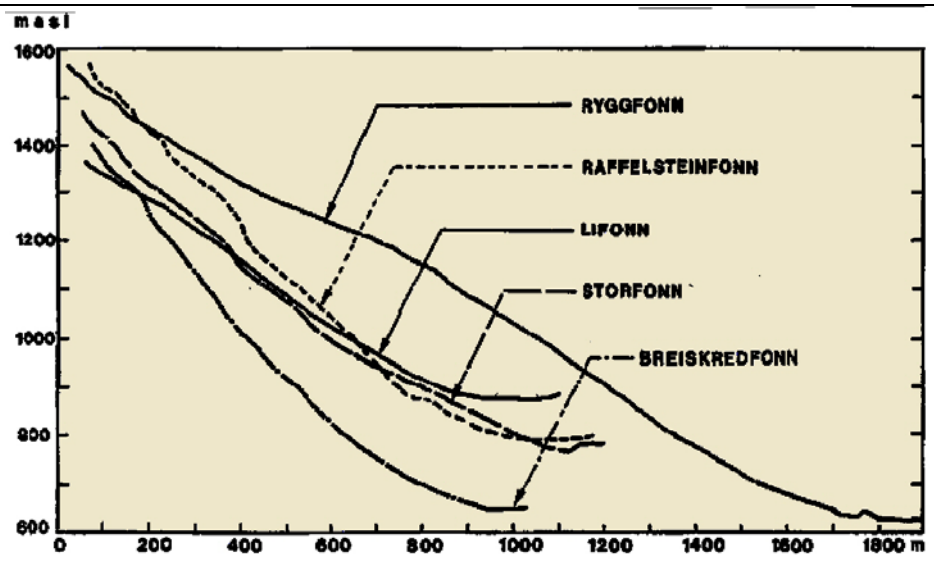
	Another important factor for avalanche release is the precipitation intensity in combination with wind drift. The snow layers are stabilizing with a certain factor during the snow fall, and if the precipitation intensity is below certain values, it might snow for days without avalanche release. If, on the other hand, the snow intensity is high, the avalanche might be triggered with only a little amount of new snow. NGI developed a precipitation gauge in 1985 based on vibrating strain gauges, the Geonor precipitation gauge which is weighing the temperature. Using this gauge, it is possible to have a continuous recording of the precipitation, and this is a good tool in evaluating the avalanche hazard. An example of records is presented in the ***Figure 47*** where it was released an avalanche the 1997-03-02 between 01:50 and 02:50 where the snow fall intensity was up to 3.7 mm (as melted water) per hour.

Figure 47 Weather observations from Grasdalen, Strynefjell 1. and 2. of March 1997

Dato	kl	ref	T_{inn}	FF m/s	FFg m/s	DD	TT	TT	NN	SS cm	nn	ΣRR mm	ΔRR mm
970301	1351	572	15.4	3.1	19.7	325	-1.9	-3.1	19	257	1002	230.3	
970301	1450	572	15.5	3.2	10.4	182	-2.0	-3.1	19	258	1021	230.9	0.6
970301	1550	572	15.7	2.2	5.4	129	-2.1	-3.2	20	258	29	231.8	0.9
970301	1650	572	15.8	1.0	3.3	85	-2.0	-2.9	20	260	60	232.8	1.0
970301	1750	572	15.9	2.2	6.0	151	-1.4	-2.3	20	260	70	233.2	0.4
970301	1850	572	15.9	1.7	5.4	102	-1.3	-2.2	20	257	89	233.7	0.5
970301	1950	572	15.9	1.9	4.8	123	-0.7	-1.7	20	385	104	234.3	0.6
970301	2050	572	16.0	1.6	5.1	136	-0.7	-1.8	20	385	133	235.2	0.9
970301	2150	572	16.0	1.9	5.1	130	-0.6	-1.7	20	385	180	236.8	1.6
970301	2250	572	16.1	1.6	3.6	166	-0.3	-1.5	20	385	233	238.5	1.7
970301	2350	572	16.2	0.7	2.7	55	-0.2	-1.5	20	385	322	241.5	3.0
970302	0050	572	16.2	0.0	0.3	134	-0.2	-1.5	20	385	401	244.2	2.7
970302	0150	572	16.3	0.0	0.3	122	-0.3	-1.6	20	385	497	247.4	3.2
970302	0250	572	16.2	0.0	0.3	141	-0.2	-1.6	20	385	606	251.1	3.7
970302	0350	572	16.3	0.0	0.3	122	-0.2	-1.5	20	385	702	254.3	3.2
970302	0450	572	16.3	0.0	0.3	124	0.0	-1.2	20	385	771	256.7	2.4
970302	0550	572	16.3	0.0	0.3	138	-0.1	-1.3	20	385	821	258.4	1.7
970302	0650	572	16.4	0.0	0.3	179	-0.2	-1.2	20	385	859	259.6	1.2
970302	0750	572	16.4	0.0	0.3	140	0.3	-0.9	20	385	866	260.0	0.4
970302	0850	572	16.4	0.0	0.3	311	0.3	-0.8	20	385	974	263.4	3.4
970302	0950	572	16.5	0.6	3.6	148	0.5	-0.7	20	385	1001	264.3	0.9
970302	1050	572	16.6	1.0	3.6	210	0.5	-0.7	21	385	39	266.4	2.1
970302	1150	572	16.6	2.3	9.0	130	-0.6	-1.8	21	385	69	267.5	1.1

	References
Debris Flows	A., C., M., C., F., G., and P., R., 1995: Gis technology in mapping landslide hazard. Carrara, and Guzzetti, Eds., Geographical Information System in Assessing Natural Hazard, New York, 135–176. Anderson, M., and Brooks, S. E., 1996: Advances in hillslope processes. Symposia Series.John Wiley and Sons. Baum R., Savage W., Godt J. 2002: Trigrs-a fortran program for transient rainfall infiltration and grid-based regional slope-stability analysis. Open-File Report 02-0424, U.S. Geological Survey Bandis, S. C., 1999: Numerical modelling techniques as predictive tools of groundin stability. Springer-Verlag, Ed., Floods and Landslides: Integrated RiskAssessment, Springer-Verlag, 101–118. Bertoldi, G., and Rigon, R., 2004: Geotop: A hydrological balance model. Technical description and programs guide. Technical Report DICA-04-001, University of Trento E-Prints, http://eprints.biblio.unitn.it/archive/00000551/. Bertoldi, G., Rigon, R., and Over, T. M., 2005: Impact of watershed geomorphic characteristics on the energy and water budgets. Journal of Hydrometeorology,7(3), 389–403. Beven, K. J., and Kirkby, M. J., 1979: A physically-based variable contributing area model of basin hydrology. Hydrol. Sci. Bull., 24(1), 43–49. Bischetti, G., Simonato, T., and Chiaradia, E., 2004: Valutazione del contributo degli apparati radicali nell'analisi di stabilit`a dei movimenti franosi superficiali. Rivista di Ingegneria Agraria, 3(3), 25–32. Bishop, A. W., 1955: The use of slip circle in the stability analysis of slopes. Geotechnique, 5(1), 25–32. Bromhead, E., 1996a: Slope stability modelling: an overview. S. L. Dikau R, Brunsden D, and I. M, Eds., Landslide Recognition. Identification, movement and causes, John Wiley and Sons, 231–235, Chichester. 24 Bromhead, E., 1996b: The treatment of landslides. Geotechnical Engineering, 125(85-96). Brooks, R., and Corey, A., 1964: Hydraulic properties of porous media. Hydrology Paper, 3, 27, Colorado State University, Fort Collins. Caine, N., 1980: The rainfall intensity-duration control of shallow landslides and debris flows. Geografiska Annaler, 62A, 23–27. Campbell, R., 1975: Soil slips, debris flows and rainstorms in the santa monica mountains and vicinity, southern california. United states. United States Geological Society Professional Paper, (851). Casadei, M., Dietrich, W. E., and Miller, N. L., 2003: A model for predicting the timing and locatgion of shallow landslide initiation in soil-mantled landscapes. Earth Surface Processes and Landforms, 28, 925–950. Crosta, G., 1998: regionalization of rainfall thresholds: anaid to landslide hazard evaluation. Environmental Geology, 35(2-3), 133–145. Dhakal, A. S., and Sidle, R. C., 2004: Pore water pressure assessment in a forest watershed: Simulations and distributed field measurements related to forest practice. Water Resources Research, 40(W02405). Dietrich, W. E., and Montgomery, D., 1994: A physically based model for the topographic control on shallow landsliding. Water Resour. Res., 30(4), 1153–1171. Dietrich, W. E., Reiss, R., and Montgomery, D., 1995: A process-based model for colluvial soil depth and shallow landsliding using digital elevation data. Hydrol. Proc., 9, 383–400. Dietrich, W. E., Wilson, C. J., Montgomery, D. R., and McKean, J., 1993: Analysis of 25 erosion thresholds, channel networks, and landscape morphology using a digital terrain model. J. Geology, 101(2), 259–278. D'Odorico, P., Fagherazzi, S., and Rigon, R., 2005: Potential for landsliding: Dependence on hyetograph characteristics. Journal of Geophysical Research, 110, FO1007. Doodge J.C.I. 1959: A general theory of the unit hydrograph, Jornal of Geophys. Res., 64, 241-256 Dunne, T., 1978: Field studies of hillslope flow processes. M. J. Kirkby, Ed., Hillslope Hydrology, Wiley-Interscience, New York, 227–293. Feller, W., 1968: An Introduction to Probability Theory and its Applications, vol. 1. John Wiley and Sons, 3 edn. Freeze, R. A., and Harlan, R. L., 1972: Role of subsurface flow in generating surface runoff 2. Upstream source areas. Water Resour. Res., 8(5), 1272–1283. Glade, T., Crozier, M., and Smith, P., 2000: Applying probability determination to refine landslide triggering rainfall threashold using an empirical antecedent daily rainfal model. Pure and Applied Geophysics, (157), 1059–1079. Godt, J., Baum, R. L., and Chleborad, A. F., 2005: Rainfall characteristics for shallow landsliding in seattle, washington, area: Earth surface processes and landforms. Earth Surface Processes and Landforms. Gupta, V.K. & E. Waymire, On the formulation of an analytical approach to understandhydrological response and similarity at the basin scale, J. Hydrol., 65, 95-129, 1983 Guzzetti, F., Carrara, A., Cardinali, M., and Reichenbach, P., 1999: Landslide hazard evaluation: a review of current techniques and their application in a multi-scale study, central italy. Geomorphology, 31, 181–216. Heimsath, M. A., Dietrich, W. E., Nishiizumi, K., and Finkel, R., 1997: The soil production function and landscape equilibrium. Nature, 388, 358–361. Hirano M. 1997: Prediction of debris flow for warning and evacuation, in "Recent Developments on Debris Fow, Lectures Notes in Earth Sciences, vol 64, 7-26, Armanini A. e Michiue M. Ho, K., 2003: Geotechnical Engineering – Meeting Society's Needs. A.A. Balkema. Horton, R. E., 1933: The role of infiltration in the hydrological cycle. EOS, Transactions, American Geophysical Union, 14, 446–460. 26 Iverson, R., 2000: Landslide triggering by rain infiltration. Water Resour. Res., 36(7), 1897–1910. Kirchner, J. W., 2006: Getting the right answers for the right reasons: Linking measurements, analyses, and models to advance the science of hydrology. Water Resources Research, 42(W03S04).

Larsen, M. C., and Simon, A., 1993: A rainfall intensity-duration threshold for landslides in a humid-tropical environment, puerto rico. Geografiska Annaler, 75 A(1-2), 13–23.
Leij, F., Romano, N., Palladino, M., Schaap, M., and Coppola, A., 2004: Topographical attributes to predict soil hydraulic properties along a hillslope transect. Water Resour. Res., 40(W02407), doi:10.1029/2002WR001641.
Lu, N., and Lycos, W. J., 2005: Suction stress characteristic curve for unsaturated soil. In press.
Maulem Y. 1976: Anew model for predicting the hydraulic conductivity of unsaturated porous media. Water Resour. Res., 12, 513-522
Montgomery D. R., D. W., 2004: Reply to comment by richard m. iverson on "piezometric responsein shallow bedrock at cb1: Implications for runoff' generation and landsliding,'. Water Resources Research, 40, W03802.
Nobuyuki, T., and Okimura, T., 2004: Proposal of risk evaluation method for rain-induced slope failure on road slope. I. S. I. 2004, Ed., Proposal of Risk evaluation method for rain-induced slope failure on road slope, International Symposium Interpraevent 2004.
NRC, 2003: Report of a workshop on predictability and limits-to-prediction in hydrologic systems. Tech. rep., Committee on Hydrologic Science.
Okimura, T., 1983: A slope stability method for predicting rapid mass movements on granite mountain slopes. Natural Disaster Science, 5(1), 13–30.
Okimura, T., and Ichikawa, R., 1985: A delimitation method for probable mountain 27 slope failures by a digital land form model. Jouranl of Japan Society of civil engineers, (358), 69–75. on Stability of Earth Slopes, E. C., Ed., 1954: Application of Composite Slip Surface for Stability Analysis.
Pack, R. T., Tarboton, D. G., and Goodwin, C. N., Eds., 1998: The SINMAP approach to terrain stability mapping, vol. 2, 8th Congress Association of Engineering Geology.
Paniconi, C., and Putti, M., 1994: A comparison of Picard and Newton iteration in the numerical solution of multidimensional variably saturated flow problems. Water Resour. Res., 30(12), 3357–3374.
R, I., 2004: Comment on piezometric response in shallow bedrock at cb1: Implications for runoff generation and landsliding by david r. montgomery, william e. dietrich, and john t. heffner,. Water Resour. Res., 40 , 40, doi:10.1029/2003WR002077.
Rawls, W. J., Gish, T. J., and Brakensiek, D. L., 1989: Unsaturated Flow in Hydrologic Modeling, chap. Estimation of soil retention and hydraulic properties, 275–300. Morel-Seytoux.
Reid, M. E., and Iverson, R. M., 1992: Gravity-driven groundwater flow and slope failure potential, 2. effects of slope morphology, material properties and hydraulic heterogeneity. Water Resources Research, 28(3), 9339–950.
Richards, L. A., 1931: Capillary conduction of liquids in porous mediums. Physics, 1, 318–333.
Rigon R., Cozzini A., Pisoni S., Bertoldi G., Armanini A. 2004: A new simple method fot the determination of the triggering of debris flows, proceeding of the 10th interpraevent conference, Riva del Garda, 2004
Rigon, R., Bertoldi, G., and Over, T. M., 2006a: Geotop: A distributed hydrological model with coupled water and energy budgets and energy budgets. Journal of Hydrometeorology, 7(3), 371–388.
Rigon, R., Cozzini, A., and Tiso, C., 2006b: The horton machine: a set of open source 28 programs for the quantitative geomorphologic analysis of mountain catchments. Tech. rep., Civil and Environmental Engineering Department, Trento University.
Simoni, S., and Zanotti, F., 2006: Anallisi idrogeologica e morfodinamica nell'ambito dello studio dei fenomeni franosi nelle aree sovrastanti gli abitati di sauris di sotto e di velt in comune di sauris (ud). Tech. rep., CUDAM.
Smith R.E. 2002: infiltrtion theory for hydrologic applications, vol. 15 of water resources monograph. American geophysical union – Washington, DC, Washington DC, 212 pp.
Swift, J., 2002: Archiving and web dissemination of geotechnical data project website cosmos/peer lifelines project 2l02. Tech. rep., University of California.
Todini E. 1996: the ARNO rainfall-runoff model, Journ. Of Hydrol., 175, 339-382
Terzaghi, K., 1943: Theoretical Soil Mechanics. John Wiley and Sons.
USDA-NRCS, 2006: National soil survey characterization data. Tech. rep., Soil Survey Laboratory, National Soil Survey Center USDA-NRCS.
Van Genuchten, 1980: A closed-form equation for predicting the hydraulic conductivity of unsaturated soils. Soil Sci. Soc. Am. J., 44, 892–898.
Vereecken, H., Maes, J., Feyen, J., and Darius, P., 1989: Estimating the soil moisture retention characteristic from texture, bulk density and carbon content. Soil Science, 148(6), 389–403.
Ward, T. J., R., L., and Simons, D. B., 1982: Mapping landslide hazards in forest watersheds. J. Geotechnical Eng. Div. Am. Soc. Civ. Eng., 108, 319–324.
Wieczorek, G., 1987: Effect of rainfall intensity and duration on debris flows in central santa cruz mountains, california. Geological Society of America Reviews in Engineering Geology, 7, 93–104.
Wilson, R. C., 1997: Broad-scale climatic influences on rainfall thresholds for debris flows: adapting thresholds for northern california to southern california.
Geological Society of America Reviews in Engineering Geology, 11, 71–80.
Wu, W., and Sidle, R., 1995: A distributed slope stability model for steep forested basin. Water Resources Research, 31(8), 2097–2110. 29
Wu, W., and Sidle, R., 1996: A distributed slope stability model for steep forested basin. International Journal of Rock Mechanics and Mining Science and Geomechanics, 33(4), 178.
Zanotti, F., Endrizzi, S., Bertoldi, G., and Rigon, R., 2004: The geotop snow module. Hydrol. Proc., 18, 3667–3679. DOI:10.1002/hyp.5794.
Zhao R.J., Zhuang Y.R., Liu X.R., Zhang Q.S. 1980:the Xinanjiiang model, in Hydrol' Forecasting IAHS Publications No. 129, Wallingfort, UK, 351-356
Zimmermann, R., and Bardet, J. P., 1998: Geotechnical info management and exchange project. Tech. rep., University of Southern California..

Debris flows

Burlando, P., and R. Rosso (1996), Scaling and multiscaling models of depth-duration-frequency curves of storm precipitation, J. Hydrol., 187, 45-64.

(continued)	storm precipitation, J. Hydrol., 187, 45-64. Montgomery DR, Dietrich WE. (1994), A physically based model for the topographic control on shallow landsliding, Water Resour. Res., 30(4), 1153–1171. Rosso, R., M. C. Rulli, and G. Vannucchi (2006), A physically based model for the hydrologic control on shallow landsliding, Water Resour. Res., 42, W06410, doi:10.1029/2005WR004369. Skempton AW, DeLory FA. (1957), Stability of natural slopes in London clay, ASCE Journal, 2, 378–381. Burlando, P., and R. Rosso (1996), Scaling and multiscaling models of depth-duration-frequency curves of storm precipitation, J. Hydrol., 187, 45-64. Burroughs, E.R., Jr., C.J. Hammond, and G.D. Booth (1985), Relativity stability estimation for potential debris avalance sites using field data, in Proceedings of the International Symposium on Erosion, Debris Flow and Disaster Prevention, Edited by A. Takei, 335-339, Erosion Control Society, Tokio. Caine N. (1980), The rainfall intensity–duration control of shallow landslides and debris flows. Geogr. Annales, Series A 6, 23–27. Campbell RH. (1975), Soil slips, debris flows and rainstorms in the Santa Monica Mountains and vicinity, southern California, United States Geological Society Professional Paper, 851. Cancelli A, Nova R. (1985), Landslides in soil debris cover triggered by rainstorms in Valtellina (Central Alps – Italy), in Proceedings 4th International Conference on Landslides, Tokyo. The Japan Geological Society, 267–272. Cannon S.H., and Ellen S.D. (1985), Rainfall conditions for abundant debris avalanches in the San Francisco Bay Region, California, California Geology, 38 (12), 267-272. Canuti P, Focardi P, Garzonio CA. (1985), Correlation between rainfall and landslides. Bulletin of the International Association of Engineering Geologists, 31, 49–54. Carrara A. (1983), Multivariate models for landslide hazard evaluation. Mathematical Geology, 15, 403–426. Carrara A. (1993), Uncertainty in evaluating landslide hazard and risk. In Prediction and Perception of Natural Hazards, Nemec J, Nigg JM, Siccardi F (eds). Kluwer Academic Publishers: Dordrecht; 101–109. Carrara A, Cardinali M, Detti R, Guzzetti F, Pasqui V, Reichenbach P. (1991), GIS techniques and statistical models in evaluating landslide hazard. Earth Surf. Proc. Land.,16, 427– 445. Carrara A, Cardinali M, Guzzetti F, Reichenbach P. (1995), GIS technology in mapping landslide hazard. In Geographical Information System in Assessing Natural Hazard, Carrara A, Guzzetti F (eds). Kluwer: New York; 135–176. Casadei M., Dietrich W.E. and Miller N.L. (2003) Testing a model for predicting the timing and location of shallow landslide initiation in soil-mantled landscapes, Earth Surf. Proc. Land. 28 (9), 925-950. Chung CF, Fabbri AG, Van Westen CJ. (1995), Multivariate regression analysis for landslide hazard zonation. In Geographical Information System in Assessing Natural Hazard, Carrara A, Guzzetti F (eds). Kluwer: New York; 107–134. Crozier MJ. (1999), Prediction of rainfall-triggered landslides: a test of the antecedent water status model, Earth Surf. Proc. Land., 24, 825–833. Crozier MJ, Preston NJ. (1999), Modelling changes in terrain resistance as a component of landform evolution in unstable hill country. In Process Modelling and Landform Evolution, Hergarten S, Neugebauer HJ (eds). Lecture Notes in Earth Science, Vol. 78. Springer-Verlag: Heidelberg, 267–284. Dawes, W. R., and D. Short (1994), The significance of topology for modeling the surface hydrology of fluvial landscapes, Water Resour. Res., 30, 1045–1055. D'Odorico P. and S. Fagherazzi (2003), A probabilistic model of rainfall-triggered shallow landslides in hollows: A long-term analysis, Water Resour. Res., 39(9), 1262, 10.1029/2002WR001595. D'Odorico, P., S. Fagherazzi, and R. Rigon (2005), Potential for landsliding: Dependence on hyetograph characteristics, *J. Geophys. Res.*, *110*, F01007, doi:10.1029/2004JF000127. D'Odorico, P. and R. Rigon, Hillslope and channels contribution to the hydrologic response, Water Resour Res, 39(5) , 1-9, 2003 De Graff, J.V., and P. Canuti (1988), Using isopleth mapping to evaluate landslide activity in relation to agricultural practices, Bull. Int. Ass. Eng. Geol., 38, 61-71. De Michele, C., N.T. Kottegoda, and R. Rosso (2001), The derivation of areal reduction factor of storm rainfall from its scaling properties, Water Resour. Res., 37, 3247-3252. Dietrich WE, Wilson CJ, Montgomery DR, MacKean J, Bauer R. (1992), Erosion thresholds and land surface morphology, Geology, 20, 675– 679. Dietrich WE, Wilson CJ, Montgomery DR, MacKean J. (1993), Analysis of erosion thresholds, channel networks and landscape evolution using a digital terrain model, Journal of Geology, 101, 259–278. Dietrich WE, Reiss R, Hsu M, Montgomery DR. (1995), A process-based model for colluvial soil depth and shallow landsliding using digital elevation data, Hydr. Process., 9, 383–400. Dietrich WE, Bellugi D, Real De Asua R. (2001), Validation of the shallow landslide model, SHALSTAB, for forest management. In Land Use and Watersheds: Human Influence on Hydrology and Geomorphology in Urban and Forest Areas, Wigmosta MS, Burges SJ (eds). Water Science and Application 2. American Geophysical Union: 195–227. Division of Water Resources, Department of Public Works, State of California. 1956. Floods of December 1955 in California. Dietrich, W.E. and D.R. Montgomery. 1998. SHALSTAB: A digital terrain model for mapping shallow landslide potential. http://ist-socrates.berkeley.edu/~geomorph/shalstab/. Dietrich, W.E., D. Bellugi, R. Real de Asua, and L. Stanziano. 1998. SHALSTAB Tools Tutorial: Using SHALSTAB to map shallow landslide potential. http://istsocrates.berkeley.edu/~geomorph /shalstab/ Glade T. (1997), Establishing the frequency and magnitude of landslide-triggering rainstorm events in New Zealand. Environmental Geology, 35(2–3), 160–174. Glade T, Crozier M, Smith P. (2000), Applying probability determination to refine landslide triggering rainfall thresholds using an empirical 'Antecedent daily rainfall model'. Pure and Applied Geophysics, 157, 1059–1079. Gupta, V.K., and E. Waymire (1990), Multiscaling properties of spatial rainfall and river flow distributions, J. Geophys. Res., 95(D3), 1999-2009.

	Hollingsworth R, Kovacs BS (1981), Soil slump and debris flows: prediction and protection. Bull. Assoc. Eng. Geol. , 18, 17-28. Keefer D.K., Wilson R.C., Mark R.K., Brabb E.E., Brown W.M., III, Ellen S.D., Harp E.L., Wieczorek G.F., Alger C.S., Zatkin R.S. (1987), Real time landslide warning during heavy rainfall, Science, 238 (4829), 921-925. Lanyon, L.E., and Hall, G.F. (1983), Land surface morphology:2. Predicting potential landscape instability in eastern Ohio, Soil Sci., 136, 382-386. Iida, T., (1999), A stochastic hydro-geomorphological model for shallow landsliding due to rainstorm, Catena, 34(3-4), 293-313. Iida, T. (2004), Theoretical research on the relationship between return period of rainfall and shallow landslides, Hydrol. Process., 739-756. Iverson RM. (2000), Landslide triggering by rain infiltration, Water Resour. Res., 36(7), 1897–1910. Kottegoda, N.T., R. Rosso (1997), Statistics, Probability and Reliability for Civil and Environmental Engineers, Mc-Graw-Hill Publishing Company, New York. Megahan, W.F.(1983), Hydrologic effects of clearcutting and wildfire on steep granitic slopes of Idaho, Water Resour. Res., 19(3), 811-819. Montgomery DR. (1991), Channel initiation and landscape evolution, PhD dissertation, U.C. Berkeley. Montgomery D.R., Wright R.H. and Booth T. (1991), Debris flow hazard mitigation for colluvium-filled swales. Bull. Assoc. Eng. Geol., 28, 203-323. Montgomery DR, Dietrich WE. (1994), A physically based model for the topographic control on shallow landsliding, Water Resour. Res., 30(4), 1153–1171. Montgomery DR, Dietrich WE, Torres R, Anderson SP, Loague K. (1997), Subsurface flow paths in a steep unchannelled catchment, Water Resour. Res., 33(1), 91–109. Montgomery DR, Schmidt KM, Green Berg HM, Dietrich WE. (2000), Forest clearing and regional landsliding, Geology, 28(4), 311–314. Moore, I. D. (1988), A contour-based terrain analysis program for the environmental sciences (TAPES), Eos Trans, AGU, 69, 345. Moore, I. D., and R. B. Grayson (1991), Terrain-based catchment partitioning and runoff prediction using vector elevation data, Water Resour. Res., 27, 1177–1191. O'Loughlin, E.M.(1986), Prediction of surface saturation zones in natural catchments by topographic analysis, Water Resour. Res., 22, 794-804. Okimura, T., and R. Ichikawa, A prediction method for surface failures by movements of infiltrated water in surface soil layer, Nat.Disaster Sci., 7, 41-51, 1985. Pack RT, Tarboton DG, Goodwin CN. (1998), Terrain stability mapping with SINMAP, technical description and users guide for version 1.00, Report Number 4114-0, Terratech Consulting Ltd, Salmon Arm, B.C., Canada. Pierson, T. C., (1977), Factors controlling debris flow initiation on forested hillslopes in the Oregon Coast Range, PhD Thesis, University of Washington, Seattle. Pradel D, Raad G. (1993), Effect of permeability on surficial stability of homogeneous slopes, Journal of Geotechnical Engineering ASCE, 119, 315–332. Reid, M. E., A pore-pressure diffusion model for estimating landslide inducing rainfall, J. Geol., 102, 709–717, 1994. Rodriguez-Iturbe, I. [Rodríguez-Iturbe] 1996 Comment on "The topography of optimal drainage basins" by T. Sun, P. Meakin, and T. Jo ssang [Jø] Water Resour. Res. Vol. 32 , No. 2 , p. 483-484 Rodriguez-Iturbe, I. & J.B. Valdes, The geomorphologic structure of hydrologic response, Water Resour. Res., 15(6), 1409-1420, 1979 Rodriguez-Iturbe, I. & A. Rinaldo, Fractal River Basins: Chance and Self-Organization, Cambridge Univ. Press, New York, 1997 Rulli, M.C., G. Menduni, and R. Rosso (1999), A distributed slope stability model to study shallow landslides initiation in catchment characterized by low permeable soil, Proc. IAHR Symp. "River, Coastal and Estuarine Morphodynamics", Genova, Italy, September 9-13, 1999, Vol.1, 327-336. Schroeder, W.L., and J.V. Alto (1983), Soil properties for slope stability analysis: Oregon and Washington coastal mountains, For. Sci., 29, 823-833. Seely, M.W., and D.O. West (1990), Approach to geologic hazard zoning for regional planning, Inyo national Forest, California and Nevada, Bull. Assoc. Eng. Geol., 27, 23-35. Skempton AW, DeLory FA. (1957), Stability of natural slopes in London clay, ASCE Journal, 2, 378–381. Sidle RC. And D.N. Swanston (1982), Analysis of a small debris slide in costal Alaska, Can. Geotech. J., 19, 167-174. Schmidt, K.M., J.J. Roering, J.D. Stock, W.E. Dietrich, D.R. Montgomery, T.Shaub, (2001) Root cohesion variability and shallow landslides susceptibility in the Oregon Coast Range. Canadian Geothecnical Journal, 38(1), 995-1024. Torres R, Dietrich WE, Montgomery DR, Anderson SP, Loague K. (1998), Unsaturated zone processes and the hydrologic response of a steep, unchannelled catchment. Water Resour. Res. 34(8), 1865–1879. Wieczorek, G. F., (1987) Effect of rainfall intensity and duration on debris flows in the central Santa Cruz Mountains, California, in Debris Flows/Avalanches: Process, Recognition, and Mitigation, edited by J. E. Costa and G. F. Wieczorek, pp. 93–104, Geol. Soc. Of Am. Boulder, Colo., 1987. Wieczorek, G.F., B.A. Morgan, and R.H. Campbell (2000), Debris-flow hazards in the Blue Ridge of Central Virginia, Env. Eng. Geol., VI, 3-23. Wu W, Sidle R. (1995), A distributed slope stability model for steep forested basins, Water Resour. Res. 31, 2097–2110. Yee, C.S., and R.D. Harr (1977), Influence of soil aggregation on slope stability in the Oregon Coast Ranges, Environ. Geol., 1, 367-377.
Rock avalanches	Abe, S., Mair, K., 2005. Grain fracture in 3D numerical simulations of granular shear. Geophysical Research Letters 32, L05305, doi:10.1029/2004GL022123. Abele, G., 1974. Bergstürze in den Alpen – ihre Verbreitung, Morphologie und Folgeerscheinungen.

Wissenschaftliche Alpenvereinshefte 25, 230pp.
Abele, G., 1997. Rockslide movement supported by the mobilization of groundwater-saturated valley floor sediments. Zeitschrift für Geomorphologie Supplementband N.F. 41, 1-20.
Ambrosi, C., Crosta, G.B., 2006. Large sackung along major tectonic features in the Central Italian Alps. Engineering Geology 83, 183-200.
Bachmann, D., Bousissou, S., Chemenda, A., 2004. Influence of weathering and pre-existing large scale fractures on gravitational slope failure: insights from 3-D physical modelling. Natural Hazards and Earth System Sciences 4, 711-717.
Barnouin-Jha, O.S., Baloga, S., Glaze, L., 2005. Comparing landslides to fluidized crater ejecta on Mars. Journal of Geophysical Research 110, E04010, doi:10.1029/2003JE002214.
Bottino, G., Chiarle, M., Joly, A., Mortasa, G., 2002. Modelling rock avalanches and their relation to permafrost degradation in glacial environments. Permafrost and Periglacial Processes 13, 283-288.
Boultbee, N., Stead, D., Schwab, J., Geertsema, M., 2006. The Zymoetz River rock avalanche, June 2002, British Columbia, Canada. Engineering Geology 83, 76-93.
Brodsky, E.E., Gordeev, E., Kanamori, H., 2003. Landslide basal friction as measured by seismic waves. Geophysical Research Letters 30, 2236, doi:10.1029/2003GL018485.
Bulmer, M.H., Zimmerman, B.A., 2005. Reassessing landslide deformation in Ganges Chasma, Mars. Geophysical Research Letters 32, L06201, doi:10.1029/2004GL022021.
Capra, L., Macías, J.L., 2002. The cohesive Naranjo debris-flow deposit (10 km3): A dam breakout flow derived from the Pleistocene debris-avalanche deposit of Nevado de Colima Volcano (Mexico). Journal of Volcanology and Geothermal Research 117, 213-235.
Chigira, M., Wang, W.N., Furuya, T., Kamai, T., 2003. Geological causes and geomorphological precursors of the Tsaoling landslide triggered by the 1999 Chi-Chi earthquake, Taiwan. Engineering Geology 68, 259-273.
Collins, G.S., Melosh, H.J., Acoustic fluidization and the extraordinary moblility of sturzstroms. Journal of Geophysical Research 108, NO. B10, 2473, doi:10.1029/2003JB002465.
Corominas, J., 1996. The angle of reach as a mobility index for small and large landslides. Canadian Geotechnical Journal 33, 260-271.
Chemenda, A., Bouissou, S., Bachmann, D., 2005. Three-dimensional physical modeling of deep-seated landslides: New technique and first results. Journal of Geophysical Research 110, F04004, doi:10.1029/2004JF000264.
Clavero, J.E., Sparks, R.S.J., Huppert, H.E., Dade, W.B., 2002. Geological constraints on the emplacement mechanism of the Parinacota debris avalanche, northern Chile. Bulletin of Volcanology 64, 40-54.
Crosta, G.B., Calvetti, C., Imposimato, S., Roddeman, D., Frattini, P., Agliardi, F., 2001. Granular flows and numerical modelling of landslides. DAMOCLES Report, 71p.
Crosta, G.B., Chen, H., Lee, C.F., 2004. Replay of the 1987 Val Pola Landslide, Italian Alps. Geomorphology 60, 127-146.
Crosta, G.B., Frattini, P. and Fusi, N., 2007. Fragmentation in the Val Pola rock avalanche, Italian Alps. Journal of Geophysical Research-Earth Surface, 112(F1): -.
Crosta, G.B., Imposimato, S., Roddeman, D., 2003. Numerical modelling of landslide stability and runout. Natural Hazards and Earth System Sciences 3, 523-538.
Cruden, D.M., Varnes, D.J., 1996. Landslide types and processes. In: Turner, A.K., Schuster, R.L. (Eds.), Landslides, investigation and mitigation. Special Report 247, Transportation Research Board, National Research Council, pp. 36-75.
Dade, W.B., Huppert, H.E., 1998. Long-runout rockfalls. Geology 26, 803-806.
Davies, T.R., McSaveney, M.J., 1999. Runout of dry granular avalanches. Canadian Geotechnical Journal 36, 313-320.
Davies, T.R., McSaveney, M.J., 2002. Dynamic simulation of the motion of fragmenting rock avalanches. Canadian Geotechnical Journal 39, 789-798.
Davies, T.R., McSaveney, M.J., Hodgson, K.A., 1999. A fragmentation-spreading model for long-runout rock avalanches. Canadian Geotechnical Journal 36, 1096-1110.
Denlinger, R.P., Iverson, R.M., 2004. Granular avalanches across irregular three-dimensional terrain: 1. Theory and computation. Journal of Geophysical Research 109, F01014, doi:10.1029/2003JF000085.
Dunning, S. A. (2006), The grain-size distribution of rock avalanche deposits in valley-confined settings. Italian Journal of Engineering Geology and the Environment 1, 117-121.
Erismann, T.H., Heuberger, H., Preuss, E., 1977. Der Bimstein von Köfels (Tirol), ein Bergsturz-'Friktionit'. Tschermaks Mineralogische und Petrographische Mitteilungen 24, 67-119.
Forlati, F., Gioda, G., Scavia, C., 2001. Finite element analysis of a deep-seated slope deformation. Rock Mechanics and Rock Engineering 34, 135-159.
Friedmann, S.J., Kwon, G., Losert, W., 2003. Granular memory and its effect on the triggering and distribution of rock avalanche events. Journal of Geophysical Research 108(B8), doi:10.1029/2002JB002174.
Friedmann, S.J., Taberlet, N., Losert, W., 2006. Rock-avalanche dynamics: insights from granular physics experiments. International Journal of Earth Sciences, 95(5): 911-919.
Gray, J.M.N.T., Tai, Y.C., Noelle, S., 2003. Shock waves, dead zones, and particle-free regions in rapid granular free-surface flows. Journal of Fluid Mechanics 491, 161-181.
Heim, A., 1932. Bergsturz und Menschenleben. Beiblatt zur Vierteljahresschrift der Naturforschenden Gesellschaft Zürich 20, 217pp.
Helmstetter, A., Sornette, D., Grasso, J.R., Andersen, J.V., Gluzman, S. Pisarenko, V., 2004. Slider block friction model for landslides: Application to Vaiont and La Clapière landslides. Journal of Geophysical Research 109, B02409, doi:10.1029/2002JB002160.
Hewitt, K., 1998. Catastrophic landslides and their effects on the Upper Indus streams, Karakoram Himalaya, northern Pakistan. Geomorphology 26, 47-80.

Hsü, K.J., 1975. Catastrophic debris streams (sturzstroms) generated by rockfalls. Geological Society of America Bulletin 86, 129-140.
Huggel, C., Zgraggen-Oswald, S., Haeberli, W., Kääb, A., Polkvoj, A., Galushkin, I., Evans, S.G., 2005. The 2002 rock/ice avalanche at Kolka/Karmadon, Russian Caucasus: assessment of extraordinary avalanche formation and mobility, and application of QuickBird satellite imagery. Natural Hazards and Earth System Sciences 5, 173-187.
Hungr, O., 1995. A model for the runout analysis for rapid flow slides, debris flows, and avalanches. Canadian Geotechnical Journal 32, 610-623.
Hungr, O., Evans, S.G., 2004. Entrainment of debris in rock avalanches: An analysis of a long run-out mechanism. Geological Society of America Bulletin 116, 1240-1252.
Hungr, O., Evans, S.G., Bovis, M., Hutchinson, J.N., 2001. Review of the classification of landslides of the flow type. Environmental and Engineering Geoscience 7, 221-238.
Iverson, R.M., 2003. How should mathematical models of geomorphic processes be judged? In: Wilcock, P.R., Iverson, R.M. (Eds.), Prediction in geomorphology. American Geophysical Monograph 135, AGU Washington, DC, pp. 83-94.
Iverson, R.M., Logan, M., Denlinger, R.P., 2004. Granular avalanches across irregular three-dimensional terrain: 2. Experimental tests. Journal of Geophysical Research 109, F01015, doi:10.1029/2003JF000084.
Kelfoun, K., Druitt, T.H., 2005. Numerical modeling of the emplacement of Socompa rock avalanche, Chile. Journal of Geophysical Research 110, B12202, doi:10.1029/2005JB003758.
Kilburn, C.R.J., Pasuto, A., 2003. Major risk from rapid, large-volume landslides in Europe (EU Project RUNOUT). Geomorphology 54, 3-9.
Legros, F., 2002. The mobility of long-runout landslides. Engineering Geology 63, 301-331.
Legros, F., Cantagrel, J. M., Devouard, B., 2000. Pseudotachylyte (Frictionite) at the base of the Arequipa volcanic landslide deposit (Peru): Implications for emplacement mechanisms. Journal of Geology 108, 601-611.
Li, M.H., Hsu, M.H., Hsieh, L.S., Teng, W.H., 2002. Inundation potential analysis for Tsao-Ling landslide lake formed by Chi-Chi earthquake in Taiwan. Natural Hazards 25, 289-303.
Liao, W.M., Chou, H.T., 2003. Debris flows generated by seepage from landslide dams. In: Rickenmann, D., Chen, C.L. (Eds.), Proceedings 3rd International Conference on Debris-Flow Hazard Mitigation, Millpress, Rotterdam, pp. 315-325.
Lynett, P., Liu, P.L.F., 2005. A numerical study of the run-up generated by three-dimensional landslides. Journal of Geophysical Research 110, C03006, doi:10.1029/2004JC002443.
McDougall, S., Hungr, O., 2004. A model for the analysis of rapid landslide motion across three-dimensional terrain. Canadian Geotechnical Journal 41, 1084-1097.
McSaveney, M.J., 2002. Recent rockfalls and rock avalanches in Mount Cook National Park New Zealand. In: Evans, S.G., DeGraff, J.V. (Eds.), Catastrophic Landslides: Effects, Occurrence, and Mechanisms. Geological Society of America Reviews in Engineering Geology XV, pp. 35-70.
Nicoletti, P.G., Sorriso-Valvo, M., 1991. Geomorphic controls of the shape and mobility of rock avalanches. Geological Society of America Bulletin 103, 1365-1373.
Panizzo, F., De Girolamo, P., Petaccia, A., 2005. Forecasting impulse waves generated by subaerial landslides. Journal of Geophysical Research 110, C12025, doi:10.1029/2004JC002778.
Pedersen, S.A., Larsen, L.M., Dahl-Jensen, T., Jepsen, H.F., Pedersen, G.K., Nielsen, T., Pedersen, A.K., Platen-Hallermund, F., Weng, W., 2002. Tsunami-generating rock fall and landslide on the south coast of Nuussuaq, central West Greenland. Geology of Greenland Survey Bulletin 191, 73-83.
Pirulli, M., 2004. Numerical analysis of three potential rock avalanches in the Alps. Felsbau 22, 32- 38.
Pirulli, M., Scavia, C., Mortara, G., Tamburini, A., Deline, P., Noetzli, J., 2006. The Thurwieser rock avalanche, Italian Alps: description and dynamic analysis. Geophysical Research Abstracts 8, 08482.
Plafker, G., Ericksen, G.E., 1978. Nevados Huascaran avalanches, Peru. In Voight, B. (Ed.), Rockslides and Avalanches I: Natural Phenomena Publications. Elsevier, Amsterdam, pp. 277-314.
Pollet, N., Cojean, R., Couture, R., Schneider, J.L., Strom, A.L., Voirin, C., Wassmer, P., 2005. A slab-on-slab model for the Flims rockslide (Swiss Alps): Canadian Geotechnical Journal 42, 587-600.
Sartori, M., Baillifard, F., Jaboyedoff, M., Rouiller, J.D., 2003. Kinematics of the 1991 Randa rockslides (Valais, Switzerland). Natural Hazards and Earth System Sciences 3, 423-433.
Scheidegger, A.E., 1973. On the prediction of the reach and velocity of catastrophic landslides. Rock Mechanics 5, 231-236.
Segalini, A., Giani, G.P., 2004. Numerical model for the analysis of the evolution mechanisms of the Grossgufer rock slide. Rock Mechanics and Rock Engineering 37, 151-168.
Shang, Y., Yang, Z., Li, L., Liu, D., Liao, Q., Wang, Y., 2003. A superlarge landslide in Tibet in 2000: Background, occurrence, disaster, and origin, Geomorphology 54, 225-243.
Sheridan, M.F. et al., 2005. Evaluating Titan2D mass-flow model using the 1963 Little Tahoma Peak avalanches, Mount Rainier, Washington. Journal of Volcanology and Geothermal Research, 139(1-2): 89-102.
Smith, G.M., Davies, T.R., McSaveney, M.J., Bell, D.H., 2006. The Acheron rock avalanche, Canterbury, New Zealand—morphology and dynamics. Landslides 3, 62-72.
Sørensen, S.A., Bauer, B., 2003. On the dynamics of the Köfels sturzstrom. Geomorphology 52, 11-19.
Stead, D., Eberhardt, E., Coggan, J.S., 2006. Developments in the characterization of complex rock slope deformation and failure using numerical modelling techniques. Engineering Geology 83, 217-235.
Tarchi, D., Casagli, N., Moretti, S., Leva, D., Sieber, A.J., 2003. Monitoring landslide displacements by using ground-based synthetic aperture radar interferometry: Application to the Ruinon landslide in the Italian Alps. Journal for Geophysical Research 108B, ETG 10-1- ETG 10-14.
Ward, S.N., Day, S., 2006. Particulate kinematic simulations of debris avalanches: interpretation of deposits and landslide seismic signals of Mount Saint Helens, 1980 May 18. Geophysical Journal International, 167(2): 991-1004.

	Weidinger, J.T., Korup, O., in press. Frictionite as evidence for a large Late Quaternary rockslide near Kanchenjunga, Sikkim Himalayas, India – implications for extreme events in mountain relief destruction. Geomorphology. Weidinger, J.T., Schramm, J.M, Nuschej, F., 2002. Ore mineralization causing slope failure in a high-altitude mountain crest—on the collapse of an 8000 m peak in Nepal. Journal of Asian Earth Sciences 21, 295-306.
Snow avalanches	Anderson, E.A. 1976. A point energy and mass balance model of snow cover. NOAA Technical Report, NWS-19. Bader, H.P., B. Salm. 1990. On the mechanics of snow slab release. Cold Regions Science and Technology, 17(3), 287-300 Bartelt, P., Lehning. M. 2002. A physical SNOWPACK model for the Swiss avalanche warning. Part I. Numerical Model. Cold Regions Science and Technology, 35 (2002) pp 123-145. Bakkehoi,S.; 1987, "Snow avalanche prediction using a probabilistic method," In Avalanche Formation, Movement and Effects, (Proceedings of the Davos Symposium, September 1986), IAHS Publication No. 162, p. 249-256 Bois, P., C. Obled and W. Good. 1975. Multivariate data analysis as a tool for day-by-dat avalanche forecast. IAHS,. 114, 391-403 Bolognesi, R. 1994. Local avalanche forecasting in Switzerland : Strategy and Tools . A new approach. Proceedings of the International snow science workshop (I.S.S.W.), 30 Oct- 3 Nov., Snowbird, Utah, USA, 463-472 Braun, L., E. Brun, Y. Durand, E. Martin. and P. Tourasse. 1994. Simulation of discharge using different method of meteorological data distribution, basin discretization and snow modelling. Nord. Hydrol., 25 (1--2) 129-144. Brun, E., E. Martin, V. Simon, C. Gendre and C. Coléou. 1989 An energy and mass model of snow cover suitable for operational avalanche forecasting. J. Glaciol., 35 (121), 333-342. Brun, E., P. David, M. Sudul and G. Brugnot 1992. A numerical model to simulate snow cover stratigraphy for operational avalanche forecasting. J. Glaciol., 38 (128), 13-22. Brun, E., E. Martin, and V. Spiridonov, 1997: The coupling of a multi-layered snow model with a GCM. Ann. Glaciol., 25, 66–72. Buser, O., M. Bütler and W. Good. 1987. Avalanche forecast by the nearest neighbours method. IAHS, 162, 557-569 Colbeck, S.C.. 1973. Effect of stratigraphic layers on water flows through snow. CREEL Spec. Rep. 311. Colbeck S.C., Akitaya E., Armstrong R., Gubler H., Lafeuille J., Lied K., Mac-Clung D. and E. Morris, 1990. The International Classification for Seasonal Snow on the Ground. Issued by the International Commission on Snow and Ice of the International Association of Scientific Hydrology and Co-Issued by the International Glaciological Society. Courtier, P., C. Freydier, J-F. Geleyn, F. Rabier and M. Rochas. 1991. The Arpege project at Météo-France. ECMWF Seminar Proceedings, 2, 193-232 Durand, Y., E. Brun, L. Mérindol, G. Guyomarc'h, B. Lesaffre and E. Martin. 1993. A meteorological estimation of relevant parameters for snow models, A. Glaciol., 18, 65-71. Durand, Y, Giraud G., L. Merindol. 1998. Short term numerical avalanche forecast used operationally at Météo-France over Alps and Pyrenees. A. Glaciol., 26, 357-367. Durand Y., Giraud G., Brun E., Mérindol L., Martin E., 1999. "A computer based system simulating snowpack structures as a tool for regional Avalanche forecast". Journal of Glaciology, Vol 45, Nø 151, pp469-485. Durand, Y., Etchevers, P., Guyomarc'h, Deque M., G., Malet, J.-P., Maquaire, O., 2006. Assessment of meteorological time series to estimate the activity of clayey landslides for present and expected future climate conditions. EGU General Assembly, 2-7 April 2006, Vienna (Austria). Etchevers, P., H. Douville, and E. Martin, 1999: Simulation of the Northern Hemisphere snow cover. IAHS Pub. No. 256, 3–10. Fohn, Paul M.B. 1987. The stability index and various triggering mechanisms. IAHS,.162, 195-214 Gassner M., Brabec B., 2002, Nearest neighbour models for local and regional avalanche forecasting , Natural Hazards and Earth System Sciences (2002) 2: 247–253 Giraud, G., J. Lafeuille and E. Pahaut. 1986. Skill evaluation of avalanche risk forecasting, IAHS, 162, 583-591. Giraud, G. 1992. MEPRA : an expert system for avalanche risk forecasting, Proceedings of the International snow science workshop, 4-8 Oct. 1992, Breckenridge, Colorado, USA, 97-106. Giraud, G and J.P. Navarre. 1995. MEPRA et le risque de déclenchement accidentel d'avalanche. Actes du colloque de l' Association Nationale pour l'Etude de la Neige et des Avalanches (ANENA) (The contribution of scientific research to safety with snow, ice and avalanche, Chamonix 30/5-03/6 1995),.145-150 Guyomarc'h G., Mérindol L; 1994. Que faut-il savoir sur Astral ?., Neige et Avalanche, ANENA, n°66, juin 1994, pp. 21-25 Jamieson, J.B. and C.D. Johnston 1993. Shear frame stability parameters for large-scale avalanche forecasting, A. Glaciol., 18,268-273 Jordan,R. 1991.A one-dimensional temperature model for a snow cover. Cold Regions Research & Engineering Laboratory , Special report 91-16, october 91,49p. Lafeuille, J., P. David, J. Konig-barde, E. Pahaut, C. Sergent and T. Granier. 1987. Intelligence artificielle et prévision de risques d'avalanches. IAHS, 162, 521-536 Lehning, M, Bartelt, P.B., Brown, R.L., Fierz, C., Satyawali, P., 2002a. A physical SNOWPACK model for the Swiss Avalanche Warning Services. Part II: Snow Microstructure, Cold Reg. Sci. Technol., 35/3, 147-167. Lehning, M, Bartelt, P.B., Brown, R.L., Fierz, C., Satyawali, P., 2002b. A physical SNOWPACK model for the Swiss Avalanche Warning Services. Part III: Meteorological Boundary Conditions, Thin Layer Formation and Evaluation, Cold Reg. Sci. Technol., 35/3, 169-184.

Martin, E., E. Brun and Y. Durand. 1994. Sensitivity of the French Alps snow cover to the variation of climatic variables, Annales Geophysicae, Ser. Atmospheres, hydrospheres and Space Sciences, 12(5),469-477

Laurent Mérindol , Gilbert Guyomarc'h and Gérald Giraud, 2002. A French Local Tool for avalanche hazard forecasting : Astral, current state and new developments. Proceedings of the International snow science workshop (I.S.S.W., Penticton, Canada.

Navarre, J-P. 1975. Modèle unidimensionnel d'évolution de la neige déposée. La Météorologie, VI 3 , 109-120.

Obled, Ch and B. Rossé. 1975. Modèles mathématiques de la fusion nivale en un point, ORSTOM, série Hydrologie, vol XII, n°4, 235-258.

Schlosser, C. A., A. G. Slater, A. Robock, A. J. Pitman, K. Y. Vinnikov, A. Henderson-Sellers, N. A. Speranskaya, K. Mitchell, and the PILPS 2(d) contributors, 2000: Simulations of a boreal grassland hydrology at Valdai, Russia: PILPS Phase 2(d). Mon. Weather Rev, 128, 301-321.

Schweizer, J 1993. The influence of the layered character of snow cover on the triggering of slab avalanche. A. Glaciol., 18, 193-198.

Schweizer, J. and Paul M.B. Föhn. 1994a. Two expert systems to forecast avalanche hazard for a given region. Proceedings of the International snow science workshop (I.S.S.W.), 30 Oct- 3 Nov., Snowbird, Utah, 295-309

Schweizer, M., Paul M.B. Föhn and Schweizer J. 1994b. Integrating neural networks and rule based systems to build an avalanche forecasting system. Proc. IASTED 4-6 July 1994, Zürich, Switzerland

Weir, P and D. M. Mac Clung. 1994. Computer based artificial intelligence as an aid to British Columbia Avalanche Forecasters. Canadian Avalanche Association, Avalanche News, 43, 2-4.